ABSTRACT

Title of Dissertation: EFFECT OF COOLING ON HYPERSONIC BOUNDARY-LAYER STABILITY

Laura Paquin
Doctor of Philosophy, 2022

Dissertation Directed by: Professor Stuart Laurence
Department of Aerospace Engineering

The prediction of boundary-layer transition to turbulence on hypersonic vehicles has long been considered a primary design concern due to extreme levels of heating and dynamic pressure loading this transition induces. While it has been predicted that the temperature gradient between the vehicle and the local freestream can drastically alter boundary-layer stability, experimental research on the topic over the past fifty years has provided conflicting results. This study investigates the relationship between the wall-to-edge temperature ratio and boundary-layer stability on a slender cone. Campaigns in two wind-tunnel facilities were conducted: one set within the HyperTERP reflected-shock tunnel at the University of Maryland, and one set at the high-enthalpy T5 reflected-shock tunnel at the California Institute of Technology. Both sets of campaigns employed non-intrusive, optical diagnostics to analyze the structures and spectral content within the boundary layer.

In the first part of the study, performed in HyperTERP, an experimental methodology was developed to vary the wall temperature of the model using active

cooling and passive thermal management. This allowed the wall temperature ratio to be varied at the same nominal test condition (and thus freestream disturbance environment), and three thermal conditions were established for analysis. Simultaneous schlieren and temperature-sensitive-paint (TSP) imaging were performed. Calibrated schlieren images quantified the unsteady density gradients associated with second-mode instabilities, and TSP contours provided insight into the thermal footprint of mean boundary-layer structures. It was found that, overall, cooling shrunk the boundary-layer thickness, increased second-mode disturbance frequencies, and increased the amplification rate of these instabilities. At nonzero angles of attack, cooling appeared to increase the azimuthal extent of flow separation on the leeward side of the cone.

In the second part of the study, performed in T5, the disturbance structures and spectral content of laminar and transitional boundary layers were characterized under high-enthalpy conditions. Schlieren images indicated that, at these extremely low wall-to-edge temperature ratios, second-mode waves were confined very close to the wall in the laminar case. During the breakdown to turbulence, structures radiating out of the boundary layer and into the freestream were discovered. A texture-based methodology was used to characterize the Mach angles associated with these structures, and a wall-normal spectral analysis indicated a potential mechanism by which energy was transferred from the near-wall region to the freestream.

The study presents some of the first simultaneous imaging of the flow structures and associated thermal footprint of boundary-layer transition within an impulse facility. The work also presents the first time-resolved, full-field visualizations of

the second-mode dominated breakdown to turbulence at high enthalpy. Thus, the study imparts significant insight into the mechanics of boundary-layer transition at conditions representative of true hypervelocity flight.

EFFECT OF COOLING ON HYPERSONIC BOUNDARY-LAYER STABILITY

by

Laura Anne Paquin

Dissertation submitted to the Faculty of the Graduate School of the
University of Maryland, College Park in partial fulfillment
of the requirements for the degree of
Doctor of Philosophy
2022

Advisory Committee:
Professor Stuart J. Laurence, Chair/Advisor
Professor Christopher P. Cadou
Professor Kenneth H. Yu
Professor Christine M. Hartzell
Professor Kenneth T. Kiger

Dedication

This thesis is dedicated to all women in engineering, especially those who may feel that they do not belong.

Acknowledgments

I first thank my advisor Dr. Stuart Laurence who made the decision to join the High Speed Aerodynamics and Propulsion Lab (HAPL) an easy one. I have appreciated and grown from our weekly meetings as well as his efforts to tailor my thesis project to my interests and strengths.

I was fortunate to receive funding from a number of sources during grad school. Thank you to ASEE, who granted and funded my National Defense Science and Engineering Graduate (NDSEG) Fellowship during my first three years. Thank you to the ARCS Foundation for providing financial support for two years. Finally, thank you to the family of Alex Brown and the UMD Aerospace Department for honoring me with the Alex Brown Memorial Scholarship.

I also would like to thank all of the other academic mentors who have persisted over the past ten years, especially those from the University of Notre Dame. I would not have begun the academic career I did without the guidance of Dr. Thomas Juliano and Dr. Joseph Powers. I thank Dr. Juliano especially for facilitating such an impactful undergraduate research experience, igniting my interest in experimental hypersonics, and never failing to provide support throughout grad school.

Additionally, I am grateful for the other mentors who helped me persist in my PhD. I had the invaluable privilege of getting to know a number of female faculty

role models who never hesitated to meet, listen, and encourage. In particular, thank you to Dr. Alison Flatau, Dr. Mary Bowden, Dr. Anya Jones, Dr. Elaine Oran, Dr. Amy Karlsson, and Dr. Elaine Petro. I also cherish the close friendships of Wanyi Ng and Shikha Redhal which have blossomed throughout grad school.

Finally, I am thankful to my parents, Donna and Rob Paquin, who were always there to listen and support in all kinds of ways. My mother was always willing to bring homemade meals during my studies for qualifying and comprehensive exams. As the first engineer in my life, my father has always taken a special pride and interest in my work. He never hesitated to extend his workday to help me succeed, whether it meant teaching me how to crimp wires in a Home Depot parking lot, or joining me in the lab to help run a few evening experiments. And lastly, thank you to Ruby, my canine companion who devoted much of her puppyhood to sitting by my side or on my lap during many long days.

Table of Contents

List of Tables

List of Figures

List of Abbreviations

Acronyms

LENS	Large Energy National Shock Tunnel (at CUBRC)
DNS	Direct Numerical Simulation
FLDI	focused laser differential interferometry
HIEST	High Enthalpy Shock Tunnel (JAXA)
HyperTERP	Hypersonic Tunnel for Educational and Research Purposes (at UMD)
LN_2	liquid nitrogen
LST	Linear Stability Theory
PCB	PicoCoulomB piezoelectric sensors
PSD	power spectral density
PSP	pressure-sensitive paint
T5	T5 Reflected Shock Tunnel at Caltech (fifth in series)
TSP	temperature-sensitive paint

Variables and symbols

A	spectral amplitude (a.b.)
A	surface area (m^2)
c_r	phase speed
C_p	specific heat (J/kg K)
f	frequency (kHz)
f_{lens}	focal length (m)
h	convection coefficient (W/m^2 K)
I	image intensity
k	Gladstone-Dale constant (m^3/kg)
k	wavenumber (mm^{-1})
$\mathbf{K}$	conduction and convection matrix (W/m^2 K)
L	length of cone (mm)
M	Mach number
$\mathbf{M}$	specific heat thermal mass matrix (J/kg K)
n	refractive index
N	N factor

P	pressure (kPa)
q	heat flux (kW/m^2)
$\mathbf{Q}$	combined nodal heat flow vector (kW/m^2)
r	distance normal to light path (mm)
r	weak-lens radius (mm)
Re	Reynolds number
Re_∞	freestream unit Reynolds number (m^{-1})
t	time (ms)
T	temperature (K)
$\mathbf{T}$	temperature vector (K)
x	distance along the cone surface from the nosetip (mm)
x_b	axial distance along the cone from the nosetip (mm)
y	wall-normal position (mm)
y	spectral power (a.b.)
z	spanwise position (mm)
α	streamwise wavenumber
α	angle of attack ($^\circ$)
β	spanwise wavenumber
δ	boundary-layer height (mm)
δQ	uncertainty
ϵ	surface emissivity
ε	angular deflection of light ($^\circ$)
θ	angle relative to cone surface ($^\circ$)
θ_c	cone half angle ($^\circ$)
λ	wavelength of light (nm)
ρ	density (kg/m^3)
σ	Stefan-Boltzmann constant (W/m^2 K^4)
τ	luminescent lifetime (μs)
ϕ_p	planar azimuthal angle ($^\circ$)
ψ	wave angle ($^\circ$)
ω	temporal frequency

Subscripts

ab	adiabatic wall
amb	ambient
0	stagnation
BG	background
BL	boundary layer

e	boundary-layer edge
f	fluid
h	convection
r	radiation
$shot$	shot-to-shot
sys	systematic
uns	unsteadiness
tr	transition
w	wall
∞	freestream

Chapter 1: Introduction

1.1 Motivation

> *...by the time the vehicle approached Edwards, intense heating associated with shock waves around the vehicle had partially melted the pylon that attached the ramjet engine to the fuselage. The engine tore loose and crashed into a bombing range below. Knight lived to fly another day, but the lesson was clear: The fluid mechanics of hypersonic flight are exceedingly complex, and the practical risks they pose are immense.*
>
> – Ivett Leyva, 2017

The science of hypersonic flight sits at the intersection of the aviation and the space industries. Within military aviation, the design and understanding of high-speed missiles and strike aircraft have long been priorities for national defense. Within the space industry, structural and thermal systems must prove capable of reentering the atmosphere at Mach numbers around 25. Additionally, as the space industry shifts its focus to reusable launch vehicles, designers are tasked with ensuring the safe landing of complex geometries, for example engine-down configurations.

Despite the extreme utility and appeal of hypersonic capabilities throughout

the aerospace industry, there is a reason why, after 60 years of various flight programs, hypervelocity flight is still not available to the general public. The physics of hypersonic flight, an entanglement of thermal, chemical, and structural phenomena, are not adequately understood. The prediction of boundary-layer transition has repeatedly been placed in the forefront of design concerns. Identified as contributing the "largest uncertainty" to hypersonic plane design, the inability to predict this phenomenon can more than double the takeoff weight of an over-designed aircraft [11, 12]. The location and spatiotemporal extent of this transition indeed depends on a number of factors: the flight path trajectory, the dissipation of atmospheric turbulence [13, 14], and the surface smoothness or likelihood of ablation throughout the flight. Often transition evolves over time; for example, the HIFiRE-1 flight experiment experienced phases of rapid and gradual downstream movement of a transitional region during its ascent phase [15, 16]. In other cases, like that the HIFiRE-5 flight test, vehicles have undergone instantaneous "flashes" of transition, and this phenomenon has been associated with surface nonuniformities [17].

While predicting this transition front often proves elusive indeed, its thermodynamic impact has been observed repeatedly and characterized extensively. Transition during the flight test of the Sherman-Nakamura 22° cone caused surface temperature to rise at a rate of 1100 K/s [18]. Regions of transition on conical boundary layers have been associated with heat-flux levels that are 25% higher than those of fully-turbulent boundary layers and triple those in fully-laminar cases [19]. Similarly, measurements of root-mean-square (rms) pressure fluctuations have indicated that dynamic pressure loading in the transitional conical boundary layer is

more than double that of its fully-turbulent counterpart [20].

Unfortunately the arsenal of flight data at high Mach numbers pales in comparison to that in the sub-, trans-, and super-sonic regimes, and development of such vehicles depends on the integration of computational predictions and experimental data from ground-test facilities. While a large array of hypersonic test facilities do indeed exist, they always involve some sacrifice of true-flight conditions. For example, most conventional hypersonic tunnels prove incapable of creating thermal conditions representative of the atmosphere. When a stagnant test gas is expanded to Mach 6, the static temperature, or enthalpy, is reduced by 88%. Such a significant temperature drop can drastically alter and even reverse the temperature gradient between the vehicle wall and the edge of the boundary layer. Malik demonstrates how the post-shock conditions around a reentry cone can induce temperatures five times the wall temperature [21]. Stanfield et al. suggested that this discrepancy in temperature ratio between flight and ground facilities can significantly change the transition location, even outweighing opposing effects from freestream noise [22]. Thus, the effect that such a change in temperature gradient has on boundary layer stability needs to be characterized.

1.2 Literature Review

This thesis work is not alone in investigating the effects of the thermal gradient on boundary-layer stability. This section contextualizes this research within the framework of boundary-layer stability and transition efforts spanning the past

century and a half. Thorough reviews have been detailed in Refs. [1, 23, 24, 25, 26, 27, 28], and a brief summary is outlined here. A large number of contemporary numerical studies have evaluated the relationship between boundary-layer temperature and stability at length. A smaller number of experimental studies have focused on the same problem. Studies of interest of both types are described here.

1.2.1 Historical Landmark Studies

> *The results of this investigation have both a practical and a philosophical aspect.*
>
> – Osbourne Reynolds, 1883

The concept of fluid transition from laminar to turbulent originates from the pivotal work of Osbourne Reynolds [29, 30], who first related the change in pipe flow from "direct" to "sinuous" to a dimensionless number $\rho DU/\mu$. This number was first coined the "Reynolds number" by Sommerfeld in 1908 [31] and also acknowledged similarly by Prandtl in 1913 [32] and von Kármán in 1954 [33]. Lord Rayleigh further promulgated the idea of hydrodynamic similarity and, reconciling his own theory with Reynolds's experiments, concluded in 1892 that the effects of viscosity, even "infinitely small," could not be neglected [34]. In 1904 Prandtl introduced the concept of a boundary layer, identifying a thin region of fluid along a surface where viscous effects could be confined [35]. In 1914 he showed that this region on a sphere could experience the laminar-to-turbulent transition first identified by Reynolds, and the drag on bodies greatly depended on this transition [36].

In 1915, Taylor, in his observations of inflectional wind velocity profiles, first highlighted the destabilizing effect of viscosity [37], which was also acknowledged in 1921 by Prandtl [38]. Beginning with Tollmien's 1929 thesis work under Prandtl [39], Tollmien and Schlichting paved the way for linear stability theory. Schlichting first applied the theory to the problem of transition in 1933 [40], and the method was reclassified in 1956 using the e^N terminology [41]. Of particular interest to this study is the work of Mack, who famously applied linear stability theory to compressible boundary layers in the 1960s and whose work is discussed further in Section 1.2.2 [42, 43, 44].

1.2.2 Numerical Studies

> *Almost nothing is known about transition to turbulence in hypervelocity boundary layers.*
>
> – P.D. Germain and H.G. Hornung, 1997

As computations are not confined to the operational limits of testing facilities, they provide unique and critical insight into thermal effects on boundary-layer stability. Often numerical studies identify the mechanisms of transition for various flow regimes and inform the conditions needed for experiments. This section identifies the theory which laid the foundation for the work at hand.

As explained by Fedorov and Khokhlov, boundary-layer transition can often be described as a three-part process: 1) introduction of disturbances via boundary-layer receptivity, 2) amplification of unstable modes, and 3) breakdown to turbulence

[45]. This process is depicted in Fig. 1.1, with Fig. 1.1(a) showing the state of the boundary layer throughout the process: laminar, transitional, and turbulent. Fig. 1.1(b) highlights the receptivity process, which begins in the laminar stage and induces the transitional stage due to interactions explained shortly. It is to be noted that the region between $R_*(F_1)$ and $R_*(F_2)$ is hereafter referred to as the "receptive region," insofar as it comprises two receptivity mechanisms, whereby vorticity and entropy waves are swallowed into the boundary layer, as well as intermodal interactions which lead to the development of instabilities [45].

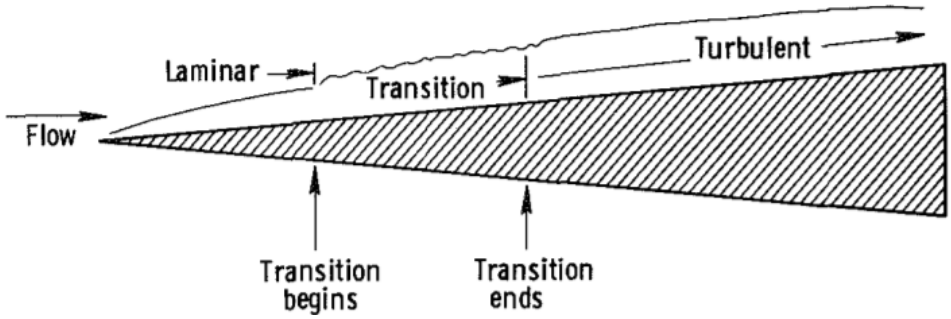

(a) State of boundary layer in three stages, from Ref. [46]

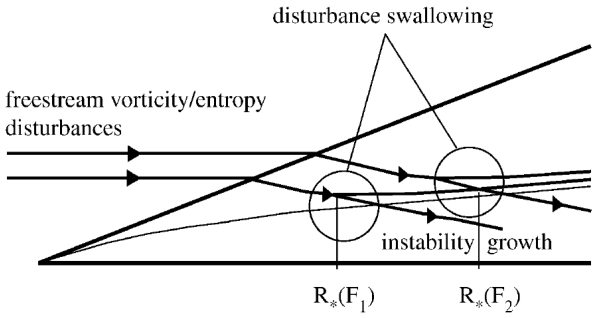

(b) Schematic of receptive region, from Ref. [45]

Figure 1.1: Stages of boundary-layer transition

Most numerical studies which have laid the framework for transition prediction have focused on the second part of the process: predicting the amplification of disturbances using linear stability theory, introduced in Section 1.2.1. The premise

of this theory is that any flow property can be decomposed into an average value and a fluctuating value. Following the terminology of Reshotko [47], the nominal property Q would be written as

$$Q = \bar{Q}(x,t) + Q'(x,t). \tag{1.1}$$

By making a parallel-flow assumption, this theory allows harmonic disturbances to be modeled as

$$Q'(x,t) = q(y)\exp[i(\alpha x + \beta z - \omega t)], \tag{1.2}$$

where q is the local amplitude at height y, α is the wavenumber of the disturbance in the streamwise direction, β is the wavenumber in the spanwise direction, and ω is the temporal frequency. Noting that any complex part of the wavenumber α_i contributes to disturbance growth or decay, the spatial amplification rate can be integrated,

$$N = \ln\left(\frac{A}{A_0}\right) = \int_{x_o}^{x} \alpha_i \, \mathrm{dx}, \tag{1.3}$$

where the N factor N relates the local amplitude of the disturbance A to the amplitude at the point of neutral stability A_0. Mack first discovered higher-order unstable modes α_n in supersonic and hypersonic boundary layers [42]. The criterion for their existence was $\bar{M}^2 > 1$, where

$$\bar{M}^2 = \frac{(\alpha\bar{U} - \omega)M_e}{[(\alpha^2 + \beta^2)\bar{T}]^{1/2}}. \tag{1.4}$$

In Eq. 1.4 (from Malik [48]), $\bar{U}$ is the non-dimensionalized streamwise velocity and $\bar{T}$ is the non-dimensionalized temperature within the boundary layer. Mack numerically compared the maximum amplification of these modes at different Mach numbers. As shown in Fig. 1.2, the maximum temporal amplifcation $(\omega_i)_{max}$ of the second mode is higher than that of all other modes for the range $2 < M \leq 10$ and five times greater than that of the first mode at $M = 5$. Mack ultimately recognized the "second mode" as being the most unstable and likely to lead to transition above Mach numbers of 4 [42].

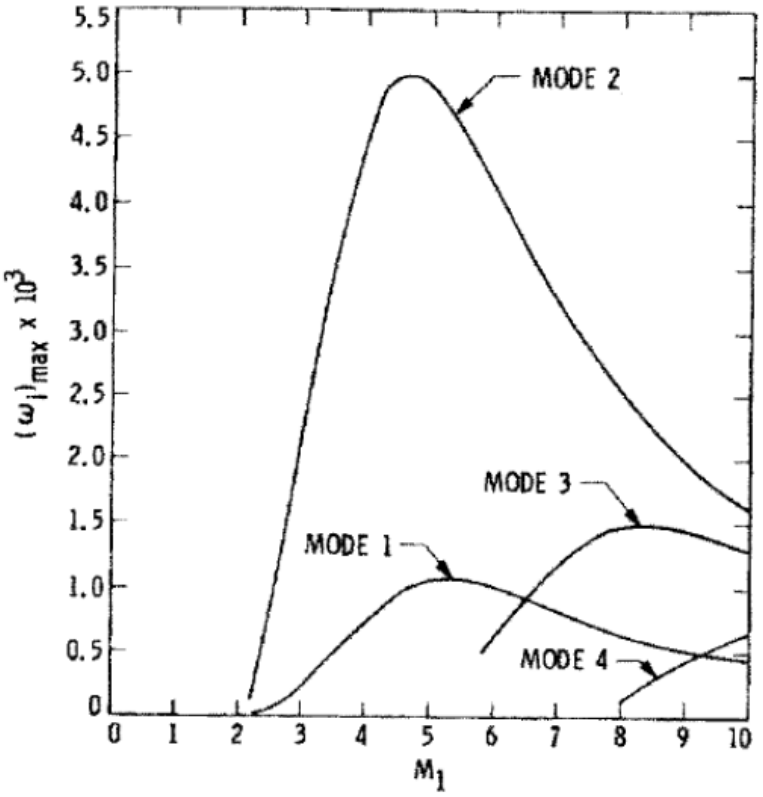

Figure 1.2: Amplitude of discrete modes at various Mach numbers from Ref. [1].

It is important to note that Fedorov and others have since clarified the terminology used by Mack and other numerical studies. Mack's first and second "modes"

are not conventional mathematical modes, which would serve as eigenfunctions to Eq. 1.2 according to normal mode decomposition. Mack "modes" instead refer to unstable regions, which, for $n \geq 2$, are caused by synchronization of fast and slow acoustic modes (which Mack instead refers to as "families") [1, 2, 45, 49]. For example, Mack's "second mode" instability occurs when the slow acoustic mode S (whose initial phase phase speed is $c_r = 1 - 1/M$) and the fast acoustic mode F (whose initial phase phase speed is $c_r = 1 + 1/M$) have equivalent phase speeds and growth rates α_i, and either F or S becomes unstable [2]. The freestream disturbance spectra, external flow properties, and upstream development of the normal modes all affect the topology of the the boundary-layer disturbances. Even minuscule changes can alter, for example, whether the fast or slow acoustic mode constitutes the instability within Mack's second-mode interaction. Fedorov and Khokhlov highlighted how these receptivity interactions at hypersonic speeds are unique from those within supersonic flowfields [45]. Thus, whether introducing new modes of instability or drastically amplifying their growth, Mach number clearly affects boundary-layer instability.

Apart from the Mach number, though, many scientists have investigated the role of temperature in the problem of stability. Although the higher-order modes had not been identified yet, Lees applied linear stability theory to compressible, supersonic flows in 1947 and first predicted that wall-cooling would stabilize the flow [50]. Mack further confirmed this effect for the first mode but concluded that cooling had the opposite (destabilizing) effect for the higher-order modes. It was found that an additional inflection point was introduced for cooled boundary layers, and the

level of cooling affected its location along with the stability of the boundary layer. Fig. 1.3 shows two numerical predictions of how cooling would affect boundary-layer stability. Fig. 1.3(a) from Ref. [1] compares the maximum temporal growth rate as a function of wall-to-recovery temperature ratio T_w/T_r for first and second-mode instabilities at various Mach numbers. As shown, the amplification rises for the second-mode instability at $M_1 = 5.8$ as the wall temperature is reduced whereas the first mode is stabilized. Fig. 1.3(b) from Ref. [48] similarly compares the spatial amplification rate as a function of the wall-to-adiabatic temperature ratio T_w/T_{ab} for first and second-mode instabilities at various Mach numbers. In this plot, where the x axis is flipped, cooling the wall again destabilizes the second-mode instability at $M_e = 4.5$ but decreases the growth of first-mode instabilities at $M_e = 2$ and 4.5.

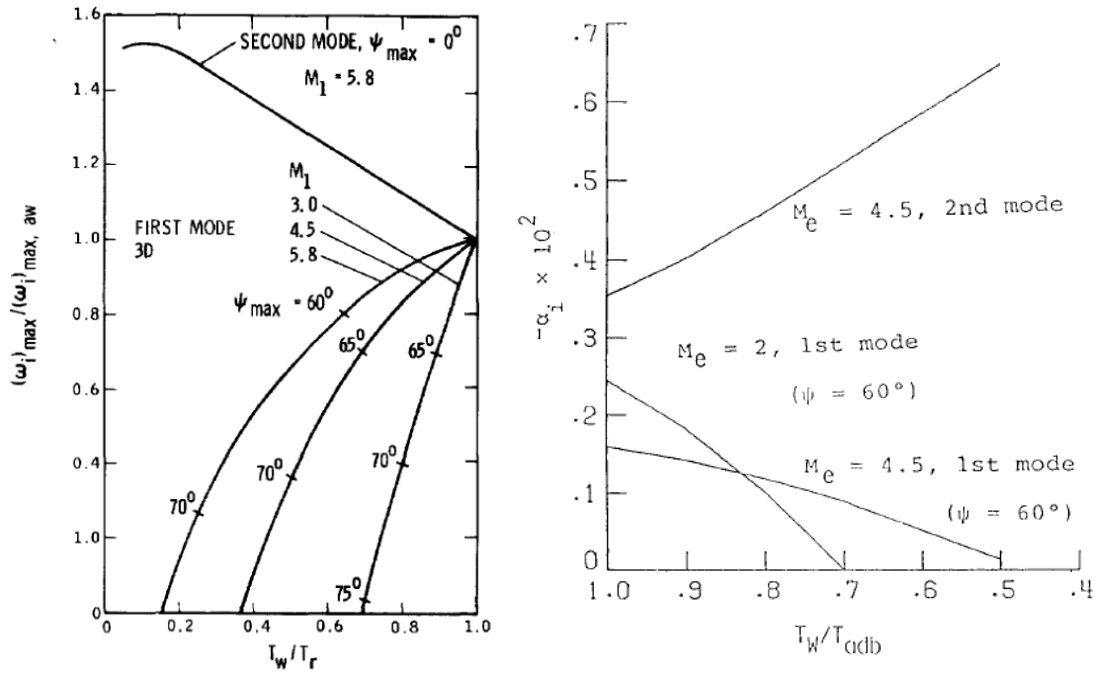

(a) Maximum temporal amplification as a function of wall cooling, from Ref. [1]

(b) Spatial amplification due to wall cooling, from Ref. [48]

Figure 1.3: Predicted effect of cooling on disturbance amplification

Recently, a number of computational studies have further investigated the destabilizing effect of cooling on the second mode, as well as interplay between the second mode and supersonic modes, which were predicted to grow unstable at cooled-wall conditions [51]. Chuvakhov and Fedorov performed a numerical study of a cooled flat plate where the supersonic mode grew unstable, suggesting that the radiation of sound waves provided a mechanism for energy transferred and potential transition delay [52]. Bitter and Shepherd depicted this radiation for a flat plate in $M = 5$ flow with $T_w/T_e = 0.2$, in Fig. 1.4 from Ref. [2]. As shown, a second sonic line is introduced above the critical layer for the supersonic mode, which induces the radiation of temperature fluctuations $\hat{\theta}_r$.

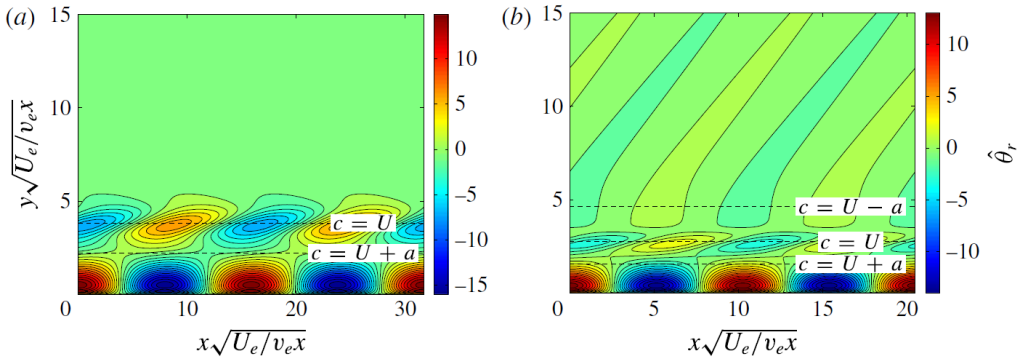

Figure 1.4: Comparison of temperature fluctuations due to a subsonic (left) and supersonic (right) mode, from Ref. [2].

Knisely and Zhong found similar results for a blunt cone in Mach-10 flow, showing that, although radiation of sound was experienced in both hot- and cold-wall conditions, the magnitude of the supersonic mode exceeded that of the traditional second mode in the cold-wall case [53]. Mortensen explained that wall temperature could determine whether the second or supersonic mode caused transition and also showed that the supersonic mode became more unstable as cone nose radius

increased, until a "critical" radius was achieved [54]. Acknowledging the competing phenomena of second-mode destabilization and acoustic radiation within cooled boundary layers, Unnikrishnan and Gaitonde sought to quantify the amount of energy efflux from radiation [55, 56]. Ultimately, they deemed that, for moderately and highly-cooled walls, the radiated energy would not outweigh the second-mode growth due to destabilization.

A final class of numerical studies has explored the effects of cooling on boundary-layer receptivity and intermodal interactions, otherwise known as the "prehistory of instability" [45]. Fedorov and Tumin found that cold-wall conditions can impact the receptivity mechanisms which induce second-mode development downstream. For instance, at $T_w/T_{ab} = 0.1$, the spectral topology in the vicinity of receptive regions (i.e. where vorticity and entropy waves are swallowed) depended strongly on the Mach number. Below $M = 6$, the fast acoustic mode F was destabilized by the second-mode interaction, but above $M = 6$, the slow acoustic mode S instead became unstable [49]. Kara et al. showed that, in contrast to the predictions of stability-based analyses, the receptivity process may have an opposing effect on the final location of boundary-layer transition. They found that found that cooled boundary layers were far less receptive to fast and slow acoustic disturbances for a slender cone at $M = 6$. The receptivity coefficient for a cone cooled to 20% of the adiabatic-wall temperature was three orders of magnitude less than that at the adiabatic condition [57]. Jahanbakhshi and Zaki demonstrated the potency of thermal manipulation as a flow-control mechanism. Their thermal texture, which concentrated most heating and cooling in the upstream portion of the receptive region,

increased the transition Reynolds number by 12% for Mach-4.5 flow over a flat plate with the most "dangerous" energy content applied at the inlet plane. Overall, they highlighted the importance of disrupting intermodal interactions (i.e. those taking place within the receptive region) and identified the pre-synchronization region as the most influential area for thermal control [58].

In summary, numerical studies based on linear stability theory indicate that wall-cooling destabilizes the second mode instability for high-Mach-number flows. Under particular cold-wall conditions, the supersonic mode may become unstable and radiate energy out of the boundary layer. Additionally, wall-cooling lowers the boundary layer's receptivity to acoustic disturbances.

1.2.3 Experimental Studies

> *The purpose is to clarify a somewhat confused picture which has evolved because the relevant data have been collected piecemeal for roughly three decades and are characterized by some gaps in coverage as well as disagreements.*
>
> – J. Leith Potter, 1980

Flight tests have long demonstrated the need to characterize the effect of the thermal gradient within the boundary layer, especially at lower wall-to-edge temperature ratios than typically achievable in conventional wind tunnels. Unfortunately, the situation described by Potter captures the general result of experiments studying the effect of the temperature ratio within the boundary layer. Various geometries

were flight-tested in the 1960s-1970s, and a few are depicted in Fig. 1.5. In the early 1960s a number of flight tests were performed investigating heat transfer on slender cones ($\theta_c = 5 - 7.5°$, $M = 1.8 - 3.8$, and expected $T_w/T_e = 1.3 - 2.1$), as well as on the wing of the X-15 ($M = 3, 5$ and expected $T_w/T_e = 1.4 - 2.4$) [59, 60, 61, 62]. Here θ_c is the cone half angle and M is the flight Mach number. These tests were remarkable in that they indicated that turbulent heat transfer rates were largely independent of Reynolds number and boundary-layer temperature gradients, leaving the existing heat-transfer theories in question [62, 63]. Further tests investigating transition on the vertical fin of the X-15, shown in Fig. 1.5(a), agreed well with ground-test data, demonstrating an order of magnitude increase in pressure fluctuations at transition relative to fully-turbulent flow [46]. In 1970 a flight test of the Sherman-Nakamura 22° cone, shown in Fig. 1.5(b) exhibited wall temperatures only 25% of the boundary-layer edge temperature [18]. It was found that the transition Reynolds numbers obtained agreed well with the experiments of Ref. [64], conducted on more slender cones at $M = 5.5 - 6.5$ and similar T_w/T_e in a ballistic range; however, the ground tests failed to show the same drag and temperature rise at transition onset that the flight test data exhibited [18]. Also in the 1970s, a flight test of the 5° Reentry-F cone, displayed in Fig. 1.5(c), demonstrated wall-to-edge temperature ratios (T_w/T_e) as low as 0.9 [65, 66]. This test provided critical insight into the transition process on slender cones at low T_w/T_e values. Two decades later, researchers at Caltech's T5 reflected-shock tunnel attempted to compare experimental results to Reentry-F flight data, and Germain and Hornung conducted the first tunnel measurements of boundary-layer transition on a 5° cone

for flight-relevant enthalpies, $h_0 > 3.5$ MJ/kg [67]. Adam and Hornung showed that the transition Reynolds number achieved within T5, when calculated with the Eckert reference temperature, matched that measured in the Reentry-F flight test reasonably well. Unfortunately the relationship between h_0 and Re^*_{tr} in the flight test opposed that seen in the experiments of Refs. [67, 68]: in the latter, a rise in flight h_0 corresponded to a decrease in Re^*_{tr}.

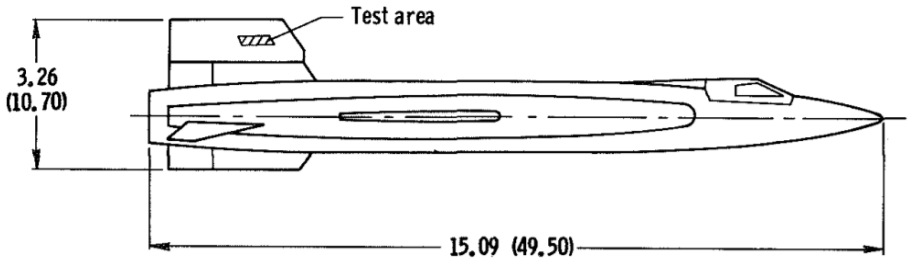

(a) X-15 with instrumented vertical fin, Fig. 1 from Ref. [46]

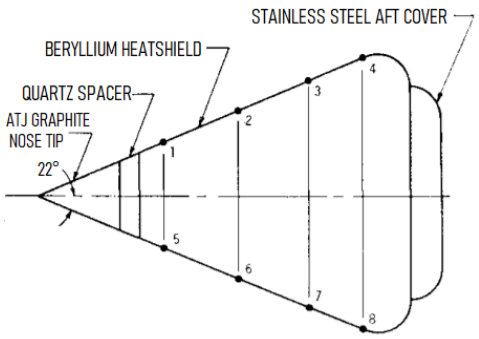

(b) Sherman-Nakamura 22° cone, adapted from Ref. [18]

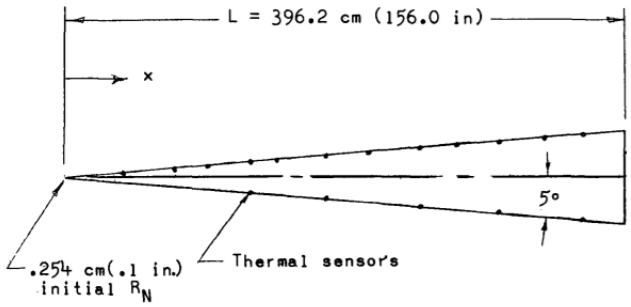

(c) Reentry-F 5° cone, Fig. 1 from Ref. [65]

Figure 1.5: Flight test geometries from the 1960s-1970s

Apart from discrepancies between flight and ground testing, tunnel experiments alone proved inconclusive when it came to evaluating thermal effects on boundary-layer transition. In general, experimental transition analysis can be classified in three categories: location/Reynolds number at transition, spectral growth

associated with transition, and the structure of disturbances leading to transition.

Most early campaigns focused on the first category: location of transition. A number of studies of interest here identified the transition Reynolds number Re_{tr} on actively-cooled and heated models. Fig. 1.6 depicts two examples of cooled models that used a similar methodology to reduce wall temperature. The 20° cone used by Scherrer and shown in Fig. 1.6(a) was actively cooled by air and capable of achieving wall temperatures T_w as low as -45°C [69, 70]. Transition results, however, were only analyzed down to $T_w/T_{aw} = 0.9$, or 90% of the adiabatic wall temperature [3, 69]. The flat plate used by Cary as well as Richards and Stollery, shown in Fig. 1.6(b), operated by recirculating liquid nitrogen (LN_2). It reached temperature ratios as low as $T_w/T_{aw} = 0.1$ [63, 71], and Richards and Stollery noted the accumulation of frost at these conditions.

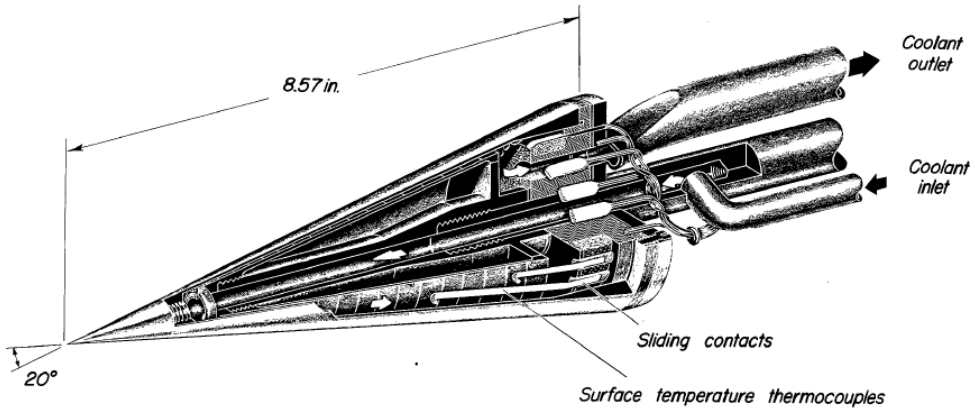

(a) Air-cooled cone from Ref. [69]

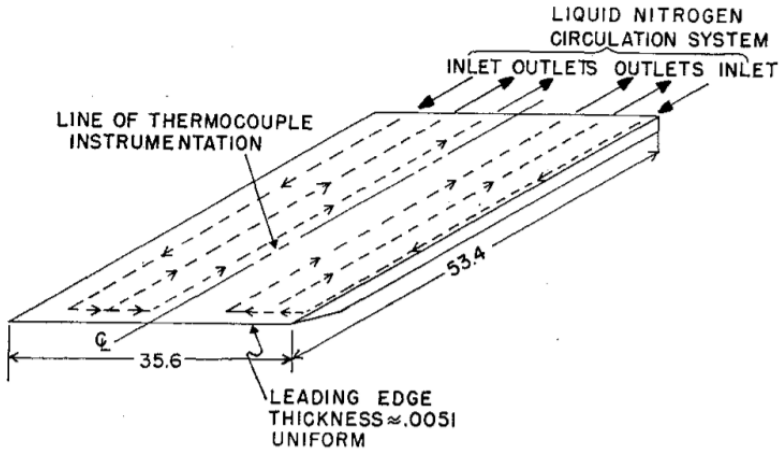

(b) LN_2-cooled plate from Ref. [63]

Figure 1.6: Models used in cooling experiments

Fig. 1.7 from Ref. [3] depicts the conflicting trends gathered from these and other experiments in the second half of the twentieth century [63, 69, 71, 72, 73, 74, 75, 76]. Potter summarized this data in an attempt to characterize the effect of the thermal gradient transition Reynolds number for flat plates and cones. Here $\bar{T} = T_w/T_{aw}$ is the wall-to-adiabatic temperature ratio, $\bar{Re}$, or $Re_{\delta t}/Re_{\delta ta}$, is the transition Reynolds number normalized by the transition Reynolds number at adiabatic-wall conditions, and M_δ is the edge Mach number. It was concluded that lower-M_δ tests showed a stronger effect of T_w/T_{aw} than higher Mach numbers

did, and freestream unit Reynolds number also affected the relationship. Results from Refs. [73] and [71] presented the phenomenon of transition reversal at certain T_w/T_{aw} values, and finally other experiments like Ref. [74] demonstrated no effect of T_w/T_{aw} on transition location.

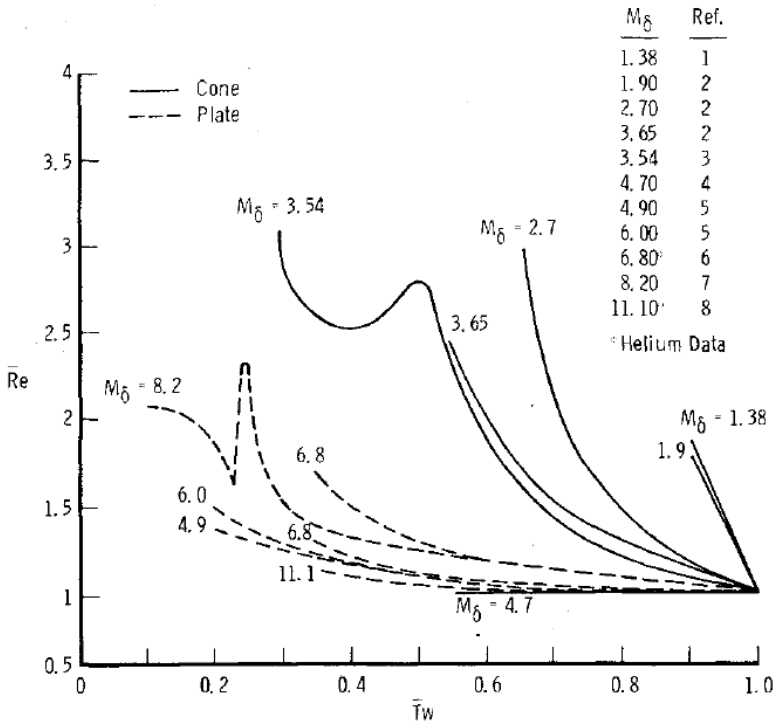

Figure 1.7: Effect of wall-to-adiabatic temperature ratio on transition Reynolds number, adapted from Ref. [3].

Stetson, in an extensive, multi-part study of conical transition, asserted that such experimental scatter could be due to the competing effects of first and second-mode disturbances (discussed in Section 1.2.2) [4]. He suggested that experiments which paid careful attention to the frequency of disturbances associated with transition could agree on the overall trend due to cooling. Both Demetriades's 1978 study and Stetson's 1989 experiment demonstrated that, in boundary layers where second-mode disturbances were the dominant instability, cooling increased the growth rate

and pushed transition upstream, a conclusion which corroborated predictions of stability theory [4, 77]. Fig. 1.8 compares the growing amplitudes of the dominant second-mode frequencies in an uncooled and cooled experiment from Stetson [4]. As shown, decreasing the wall temperature by 49% caused the transition Reynolds number to drop by 33%.

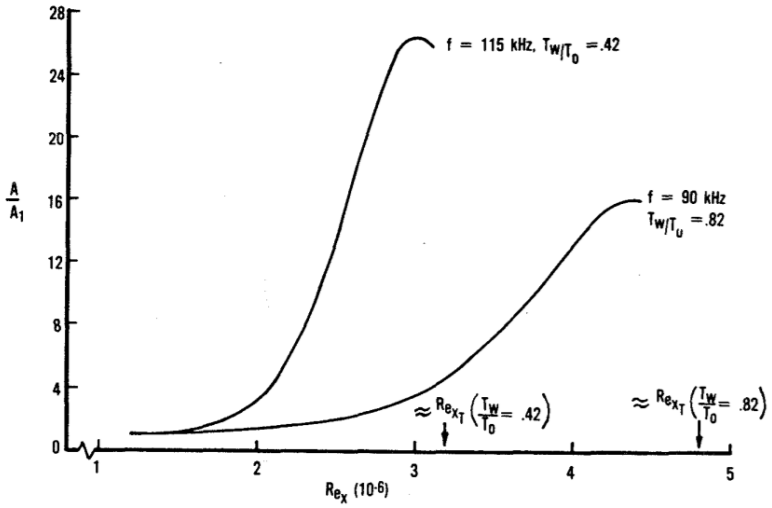

Figure 1.8: Amplitude of second-mode disturbance vs. local Reynolds number at cooled and uncooled condition, Figure 4 from Ref. [4].

Although many of Stetson's results assisted in reconciling the disparities among experimental campaigns and between experiments and theory, a number of questions still remained. For example, Stetson noted that, for both cooled and uncooled conditions, the trend of the maximum second-mode growth rate, $-\alpha$, with Reynolds number disagreed with linear stability theory. While $-\alpha$ initially increased with Re_x, it began to decrease with increasing Re_x at the point where higher-frequency content emerged. Also, second-mode frequency values did not increase with shrinking boundary layer height, as was expected from boundary-layer "tuning" [4]. Overall, Stetson's work set a precedent for further studies investigating second-mode-

dominated transition. It pointed out the importance of spectral growth analysis in a field which had largely focused on transition location measurement.

More recently, a variety of experimental programs have continued to shed insight on the spectral growth associated with transition. In particular, many studies have characterized the effect of high freestream temperatures on boundary-layer disturbances by deducing the integrated spectral amplification rate, or N factor (as defined in Section 1.2.2), of instabilities at transition using the e^N method. Alba et al. and Johnson et al. identified a factor of $N = 5.5$ as a predictor of boundary-layer transition in the NASA Langley Mach-6 and the CUBRC LENS tunnels [78, 79]. Because $N = 5.5$ predicted transition reasonably well for experiments at Mach 7 and Mach 10 with enthalpies h_0 = 2-5 MJ/kg, the discrepancy between this value and typical flight transition values (N = 8-11) was attributed to tunnel freestream noise [79]. For a set of experiments at Mach 7-8 and h_0 = 3-8 MJ/kg in JAXA's HIEST facility, however, Gronvall et al. associated $N = 8.0$ with transition on a 7°-half-angle cone. Similarly, Jewell et al. identified N = 9-10 at transition for a 5°-half-angle cone in air and an air/CO_2 mixture at enthalpies h_0 = 8-10 MJ/kg in T5 [80]. In a wide comparison of transition experiments, Marineau et al. found second-mode instabilities to reach similar spectral amplitudes at the point of transition regardless of enthalpy, but the growth of these disturbances was much more sensitive to the local Reynolds number in high-enthalpy cases than in cold-flow facilities, as shown in Fig. 1.9 from Ref. [5]. The instabilities rise in amplitude at different rates; for example, the $Re = 3.3 \times 10^6$ m^{-1} run has a much steeper slope than the $Re = 4.8 \times 10^6$ m^{-1} case in HIEST.

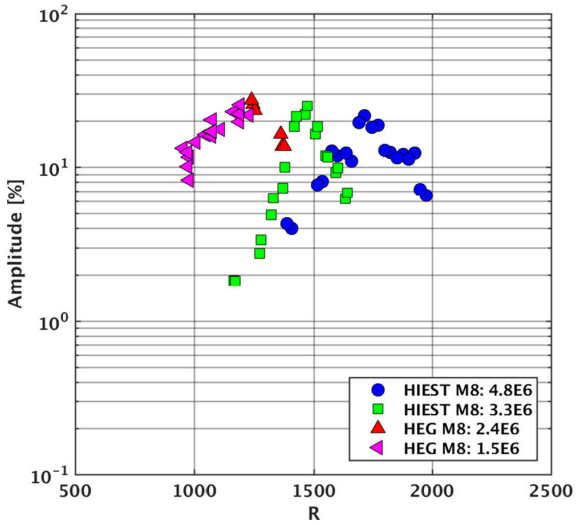

Figure 1.9: Spectral amplitude of second-mode disturbances in two high-enthalpy facilities, Figure 8 from Ref. [5].

A final category of transition studies has explored the structure and appearance of instabilities. While imaging techniques like schlieren offer unique insight into the evolution of boundary-layer disturbances, it is to be noted that such methods become increasingly difficult in high-enthalpy facilities with limited test times and chemiluminescence. Refs. [81] and [82] characterized the structures of instabilities on a 7°-half-angle cone using schlieren and PCB measurements in two different conventional hypersonic tunnels. Casper et al. quantified the intermittency of instabilities and turbulent spots at Mach 5 and 8 for freestream conditions $7 \leq Re \leq 15 \times 10^6 \mathrm{m}^{-1}$ [81]. Kennedy et al. investigated the evolution of second-mode wavepackets at Mach 10 and 14, $2 \leq Re \leq 7 \times 10^6 \mathrm{m}^{-1}$, and $1 \leq h_0 \leq 2$ MJ/kg, showing an initial double-peaked spectrum around the boundary-layer edge which transformed into a single peak as the packet propagated [82]. Laurence et al. conducted a similar analysis at $M \approx 7$, $2 \leq Re \leq 7 \times 10^6 \mathrm{m}^{-1}$, and $h_0 = 3$ and 12 MJ/kg. Schlieren images from each condition are displayed in Fig. 1.10, showing

the distinction between the wavepacket appearances at the two thermal conditions. Spectral analysis demonstrated that, in the high-enthalpy case, the harmonic intensity at the wall surpassed the signal in the rest of the boundary-layer by a factor of 3, and the instabilities exhibited an abnormal disturbance envelope as they moved in space [6]. Although breakdown into turbulence was not observed in these experiments, it is believed that the unique spectral distribution would distinguish the transition to turbulence from that visualized in conventional facilities. Additionally, it is hypothesized that the strong energy confinement near the wall makes these transitional high-enthalpy boundary layers excellent candidates for flow-control systems like porous plates and absorptive materials.

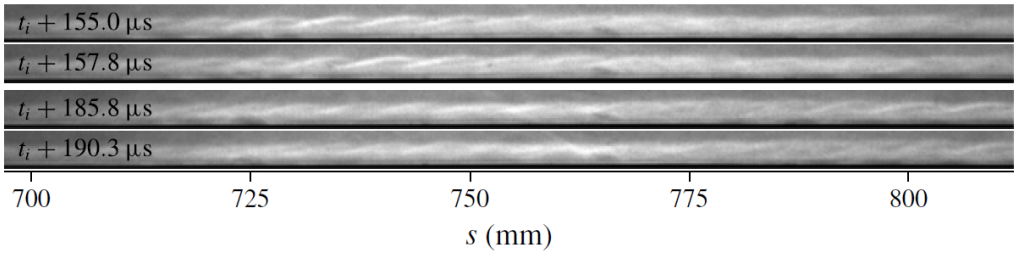

(a) Wavepackets at lower-enthalpy condition, $h_0 = 3$ MJ/kg

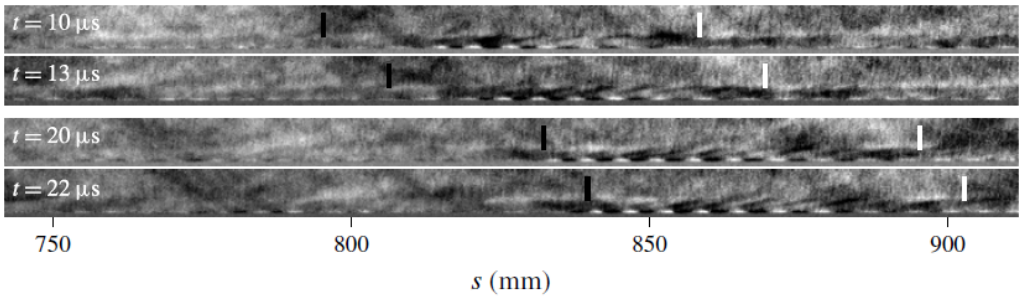

(b) Wavepackets at high-enthalpy condition, $h_0 = 12$ MJ/kg

Figure 1.10: Schlieren images of wavepackets at low and high enthalpies, Figs. 5 and 19 from Ref. [6]

While all of these contemporary studies have investigated the nature of boundary-layer transition, very few since Stetson have done so by actively altering the surface

temperature of the model. Apart from the author's own work [83, 84, 85], only a few studies are available. Blanchard actively cooled a flared cone model, decreasing the wall temperature by 34%, and tested it in quiet flow. He compared stability results gathered for the cooled case to those from an adiabatic case, demonstrating that higher frequencies and higher N factors were achieved in the cooled case [86]. More recently, Wylie heated the nosepiece of a 7° cone and analyzed the resulting disturbance spectrum, but found no significant difference in spectral amplitude for the range $T_w/T_0 = 0.12 - 0.19$ [87]. Oddo et al. actively cooled a monolithic 7° cone model, reducing the wall-to-edge temperature ratio T_w/T_e to 1.4 relative to its uncooled condition, $T_w/T_e = 4.3$ [88]. Using schlieren imaging and FLDI, they found that cooling thinned the boundary layer, increased disturbance frequencies, and delayed transition. It is difficult to reconcile this transition delay with the LST-predicted destabilization of the second mode; however, it is important to evaluate other factors leading to transiton: receptivity, spectral growth, and thermal uniformity.

1.2.4 Scope of Current Work

This study seeks to investigate the effects of the thermal gradient within the boundary layer on the stability of the flow over a slender cone. There are two clear approaches to creating the lower-T_w/T_e conditions relevant to flight: decreasing T_w by cooling the model, or increasing T_e by heating the freestream. The two parts of this work, in short, focus separately on these two approaches. In each part, non-

intrusive optical diagnostics were utilized to characterize the transition process. The results provided the most opportunity for analysis within the second two categories of transition investigation: instability amplification and breakdown to turbulence; however, the potential impact of receptivity on spectral amplitudes is also discussed. Additionally, results were compared to numerical predictions as well as data from other experimental methodologies.

The first part of the study involves a set of experimental campaigns in HyperT-ERP at the University of Maryland, where a system of active cooling was utilized to vary the wall temperature of the model while maintaining an unaltered freestream. These campaigns sought to evaluate the effect of cooling on boundary-layer structures for three different T_w/T_e values: 2.3 (uncooled), 1.9 (moderately-cooled), and 1.6 (highly-cooled). Calibrated schlieren was utilized to evaluate full-field, time-resolved density gradients within the boundary layer. Structural characteristics, like boundary-layer height and structure angle, were quantified, and power-spectral density (PSD) estimates were computed from reconstructed time signals. Temperature-sensitive paint was also used to characterize the mean heat-flux topology on the cone at two wall-temperature conditions and two angles of attack.

The second part of the study harnesses the capabilities of a high-enthalpy tunnel, T5 at the California Institute of Technology. This facility generates reservoir enthalpies of 10 MJ/kg, an order of magnitude higher than HyperTERP, inherently establishing low T_w/T_e values around 0.2 with an uncooled cone. Thus, this part of the study sought to investigate the transition mechanisms at play with extremely low T_w/T_e values and evaluate any signature of an unstable supersonic mode predicted

at these conditions. Again, schlieren imaging was utilized to interrogate boundary-layer spectral content and provide visualizations of the unique features characteristic of transition at such low T_w/T_e values.

In Chapter 2, the diagnostic techniques utilized in the two-part study are introduced. Chapter 3 presents the results of the variable wall-temperature campaign constituting the first part of the study, and Chapter 4 discusses the high-enthalpy campaign constituting the second part of the study. Finally, Chapter 5 remarks on some of the primary conclusions of the study and its contribution toward uncovering true-flight physics in experimental facilities.

Chapter 2: Overview of Diagnostics

It is the story of a way of seeing the invisible...

– Gary S. Settles, 2012

This section discusses the overall methodology and motivation for the diagnostic techniques utilized in each campaign. Further details of how each technique was implemented in each facility are discussed in Chapters 3 and 4.

2.1 Schlieren Imaging

The main diagnostic technique employed in all experiments was schlieren imaging. Schlieren has proven a remarkably instrumental technique in compressible flows, as it provides full-field images of density gradients. The schlieren technique hinges upon the Gladstone-Dale relation,

$$n - 1 = k\rho, \tag{2.1}$$

where n is the refractive index of the fluid, ρ is its density, and k is the Gladstone-Dale coefficient for the medium. Light rays bend due to optical disturbances, bending toward regions of higher n and, correspondingly, higher ρ. The integrated an-

gular deflection, ε, of a light ray passing through an optical disturbance can be expressed as

$$\varepsilon = \frac{L}{n}\frac{\partial n}{\partial r}, \tag{2.2}$$

where L is the length of the disturbance along the optical path, and $\frac{\partial n}{\partial r}$ is the gradient of the index of refraction transverse to the optical path (in this case assumed constant along L) [89]. In a typical schlieren setup, such as the Z-type shown in Fig. 2.1, a light source is positioned on one side of the region of interest containing the optical disturbance. Light rays are collimated using a lens or parabolic mirror, and then on the opposite side of the region of interest, the rays are focused back down to a point. A knife edge is introduced at the focus. This edge cuts off rays bent below the focus due to the optical disturbance, but rays bent in the opposite direction act to brighten other regions captured on the image plane. Thus, the optical disturbance's effect on $\frac{\partial n}{\partial r}$ manifests in the image intensity.

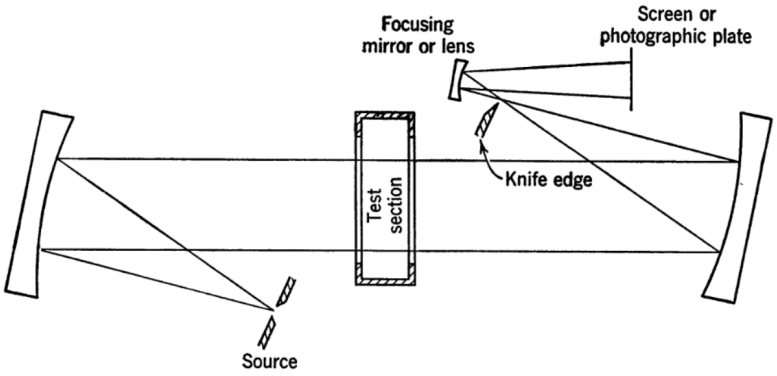

Figure 2.1: Basic Z-type schlieren system, from Ref. [7]

2.1.1 Calibrated Schlieren

Calibrated schlieren refers to the methodology by which the schlieren images are converted into full-field, quantitative measurements of density gradient $\frac{\partial \rho}{\partial r}$. The methodology involves taking an image of a calibration object with a known density gradient $\frac{\partial \rho}{\partial r}$ placed in the experimental field of view, as discussed in Ref. [8]. Fig. 2.2 demonstrates a setup where a weak lens is used as the calibration object. As shown in Fig. 2.2(a), the weak lens is placed within the region of interest between parabolic mirrors and imaged using the same optical setup as the experiment. For a long-focal-length lens, i.e. where $f_{\text{lens}} >> R$ in Fig. 2.2(b), the formula for light ray deflection is

$$\varepsilon \approx r/f_{\text{lens}}, \tag{2.3}$$

where f_{lens} is the focal length, and r is the distance from the geometric center of the lens. Intensity profiles, I, are extracted from the image of the lens and averaged to provide an I vs. r relationship. Then, following Eqs. 2.1 and 2.2 for a two-dimensional schlieren system (whereby $\frac{\partial n}{\partial r} \propto \frac{\partial \rho}{\partial r}$), a calibration is established such that $\frac{\partial \rho}{\partial r} = \text{f}(I)$. Thus, weak-lens calibration provides a way to relate image intensity directly to integrated density gradient.

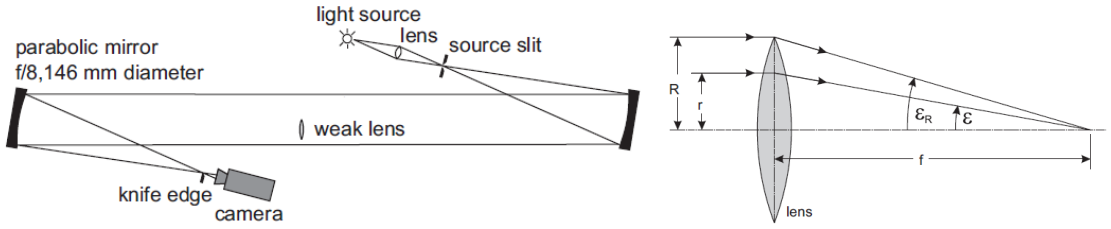

(a) Calibrated schlieren setup

(b) Weak lens ray deflection

Figure 2.2: Calibrated schlieren setup, adapted from Ref. [8]

2.1.2 Path Integration Effects

It is important to note that schlieren is a path-integrated technique, meaning that any disturbances within the optical path will bend light rays passing through them and affect the image collected past the knife edge. For experiments constructed to observe density perturbations on a single plane perpendicular to the optical path, it is important to evaluate: 1) the strength of any possible non-planar perturbations along the optical axis, and 2) the two-dimensional nature of the subject. Regarding the first concern, it is to be noted that both facilities utilized here involved free-jet test sections. In other words, the test-section diameter exceeded that of the nozzle in both cases, and core flow was bounded by a shear layer instead of a solid-wall boundary. These shear layers are quite thick relative to the boundary layer on the cone where gas is decelerated by over 1000 m/s within the span of a few millimeters. Thus, the turbulent energy within the shear layers is significantly weaker at the small length scales characteristic of the cone boundary layer. While a full characterization of tunnel disturbance environment was beyond the scope of this project, it is noted that the intensity fluctuations (and therefore density-gradient fluctuations) within the boundary layer on the model far exceeded those observed in the far field. Overall, no facility-based perturbations were deemed strong enough to significantly corrupt the boundary-layer signature.

Regarding the second concern, it is noted that the experiments in this work primarily investigate second-mode instability waves, as discussed in Sections 1.2.2-1.2.3. In every case, the schlieren system is set up with the goal of imaging second-

mode density perturbations along a central plane aligned with the cone axis and perpendicular to the optical path. Thus, it is important to assess whether this disturbance can truly be classified as two-dimensional in nature. In the pivotal work introducing the second-mode instability, Mack quantified the growth rates of first, second, and higher-order modes with various wave angles ψ, where $\psi = 0°$ corresponds to a two-dimensional wave and $\psi = 90°$ refers to a spanwise-harmonic disturbance [1]. While first-mode disturbances experienced the highest amplification rates for $50-60°$ at Mach numbers 4.5-10, second-mode waves consistently achieved the highest amplification rate at $0°$. These two-dimensional second-mode waves amplified more rapidly than their three-dimensional counterparts as well as the most unstable first-mode waves. For example, at $M = 6$, the maximum amplification rate of a second-mode wave at $\psi = 0°$ was more than double that of a first-mode wave at its most unstable orientation, $\psi = 50°$, and 4.5 times higher than a second-mode wave at $\psi = 50°$.

The two-dimensional nature of second-mode waves has been identified in other numerical and experimental investigations as well. Sivasubramanian and Fasel employed DNS to track the development of wavepackets on a sharp cone in Mach-6 quiet flow at $Re = 11 \times 10^6$ m^{-1} [90]. Computed wall-pressure fields demonstrated a strong axisymmetric topology with minimal spreading in the azimuthal direction. While some three-dimensional features, such as an oblique first-mode wave and a curved fast acoustic wave, were identified in the pressure fields, they either exhibited significantly lower amplitudes or decayed in time. Casper et al. conducted an experimental investigation at similar freestream conditions, recording pressure

fluctuations due to second-mode wavepackets within a nozzle boundary layer [91]. They characterized the second-mode wavepackets as "ordered and narrow in extent," showing that the structures concentrated the highest amplitudes of pressure fluctuations along their centerlines. These strong centerline fluctuations persisted as the structure envelope distorted and could be identified even after the point of nonlinear breakdown. Altogether, two-dimensional second-mode waves are expected to be the most unstable disturbances for the hypersonic, slender-cone boundary layer interrogated here, and thus the schlieren technique employed proves a suitable diagnostic tool.

2.2 Temperature-Sensitive Paint

While schlieren imaging can be used to provide full-field visualizations of flow features, fluorescent paints like temperature-sensitive paint (TSP) and pressure-sensitive paint (PSP) can provide global measurements of model surface properties. Hubner et al. demonstrated the utility of such fluorescent paints in short-duration facilities, resolving temperature fields during a 3-ms test time [92]. Ozawa et al. extended the capability of such techniques to a harsh high-enthalpy environment [93], and Peng et al. developed a noise-reduction methodology to increase the accuracy of temperature measurements made in such environments [94]. Running et al. utilized PSP on a blunt cone at high angles of attack to measure pressure fluctuations and, as a result, construct azimuthal separation lines due to cross-flow instabilities [95]. Pandey et al. employed TSP on a sharp cone at various angles of attack to

track the 3-D trajectory and evolution of turbulent spots generated by an electric-discharge-induced perturbation [96]. These techniques clearly allow insight into the mechanisms of transition which point measurements and planar imaging cannot.

For the first part of this study, temperature-sensitive paint was employed to visualize the mean flow topology on the cone at various wall temperatures and two different angles of attack. An adhesive film was applied to the top of the aluminum cone frustum, providing a base layer for the paint mixture, which was sprayed onto the model with a spray gun. A platinum metal complex, tris(1,10-phenanthroline)ruthenium(II) chloride hydrate (Ruphen), was utilized as the luminophore. Ruphen, has been characterized to have a very short luminescent lifetime ($\tau = 0.97$ μs [97]) and has been employed in other short-duration experiments for this reason [93, 98]. The luminophore exhibits a known Stokes shift whereby illumination near $\lambda = 450$ nm induces emission near $\lambda = 600$ nm [97], and the intensity of the fluorescence corresponds to the temperature of the molecules through thermal quenching [99]. The diagram in Fig. 2.3 demonstrates the overall operating principle. More details regarding the model, paint calibration, and heat-flux calculation are included in Chapter 3.

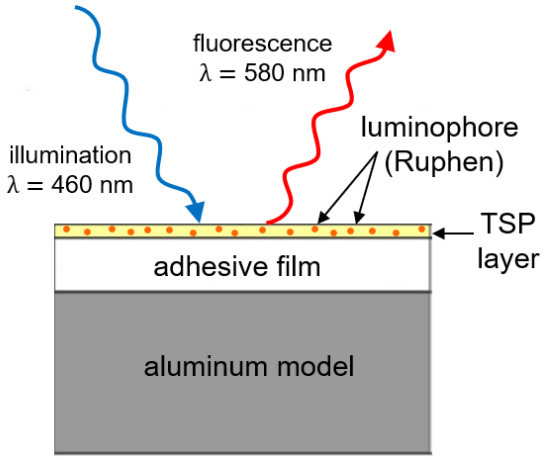

Figure 2.3: TSP diagram, adapted from Ref. [9]

Chapter 3: Experiments with Variable Wall Temperature in HyperTERP

3.1 Facility

Testing was conducted in the Hypersonic Tunnel for Educational and Research Purposes (HyperTERP) at the University of Maryland [100]. This facility, shown in Fig. 3.1, is a reflected-shock tunnel which allows variation of the freestream enthalpy and unit Reynolds number through modification of the pressure and composition of the driver and driven gases. After being compressed by both the incident and reflected shock, the test gas is accelerated through an axisymmetric contoured nozzle, producing uniform Mach-6 flow in the 0.32-m-diameter test section.

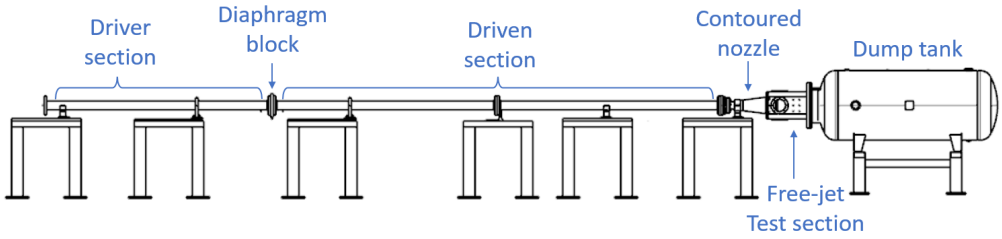

Figure 3.1: Schematic of HyperTERP, adapted from Ref. [10]

Tests were performed at a condition similar to "Re53" presented in Ref. [10], and the reservoir and freestream conditions are listed in Table 3.1. The reservoir

conditions correspond to the pressure, temperature, density, and enthalpy within the shock tube after compression by both the incident and reflected shock. A representative reservoir pressure trace is included in Fig. 3.2, along with the corresponding calculated temperature. The period of quality flow, in this case 5.9 ms, is marked. Freestream conditions were computed by assuming that the reservoir gas expands to Mach-6 flow under vibrational equilibrium up until the sonic point within the nozzle. At this point, a frozen-flow assumption was employed due to the low densities experienced at the nozzle exit [10]. Shot-to-shot variation of each flow property Q, i.e. δQ_{shot}, was characterized using the standard deviation of that flow property calculated from the set of runs. Unsteadiness, δQ_{uns}, was quantified as the root-mean-square (rms) value of fluctuations in each property during a shot. The uncertainty values ($\pm\delta Q$) listed in Table 3.1 reflect both of these sources of variation summed in quadrature. The uncertainty in reservoir pressure also includes the 1.6% systematic uncertainty, δQ_{sys}, discussed in Ref. [10], such that $\delta P_0 = \left(\delta P_{0,shot}^2 + \delta P_{0,uns}^2 + \delta P_{0,sys}^2\right)^{1/2}$.

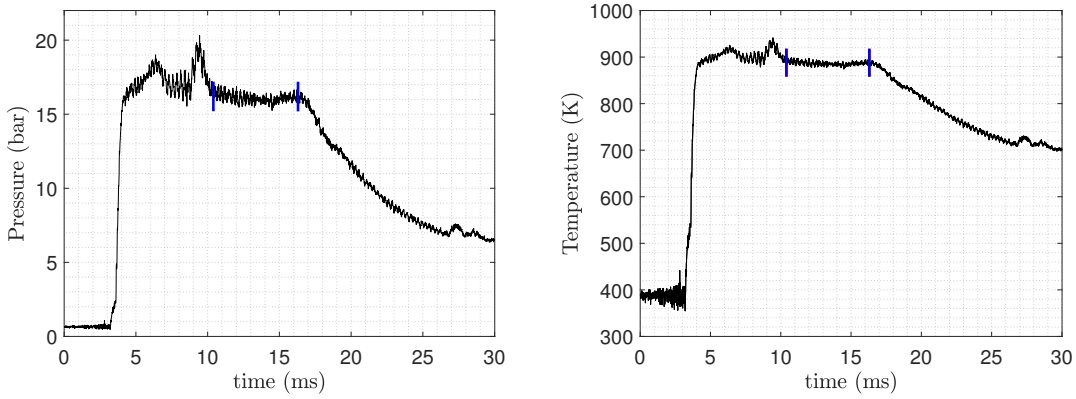

(a) Reservoir pressure trace

(b) Reservoir temperature

Figure 3.2: Reservoir pressure and temperature

reservoir			freestream		
P_0 (bar)	16.3	$\pm$ 0.4	P_∞ (Pa)	1020	$\pm$ 20
T_0 (K)	906	$\pm$ 9	T_∞ (K)	112	$\pm$ 1
ρ_0 (kg/m^3)	6.25	$\pm$ 0.10	ρ_∞ (kg/m^3)	0.0318	$\pm$ 0.0004
h_0 (MJ/kg)	1.02	$\pm$ 0.01	M_∞	6.0	
			Re_∞ ($\times 10^6$ m^{-1})	5.20	$\pm$ 0.08
			test time (ms)	5.2	$\pm$ 1.7

Table 3.1: Test conditions

3.2 Model & Cooling

For all tests a 5°-half-angle cone, 41 cm in length, was mounted in the test section of HyperTERP, as shown in Fig. 3.3. The model consisted of a 15-cm-long steel nosetip and a 26-cm-long aluminum frustum meant to enhance heat transfer during cooling. The frustum was machined in two halves, with a groove in the top half allowing a K-type thermocouple (T1) to measure surface temperature 5.2 cm upstream of the frustum base at an angle of 45° from the middle plane. An additional K-type thermocouple was fixed onto the surface of the bottom half at approximately the same distance from the frustum base. Both thermocouples carried a ±2.2°C limit of error for the temperature range examined here. A channel along the center axis allowed a PolyScience IP-100 cooler probe, one mode of cooling, to be inserted between the two halves. Apiezon thermal paste was applied along the opening to provide additional contact between the probe and the cone. A curved sting held the model in place and allowed for 1° adjustments (up to 4° in either direction) to the angle of attack. Fig. 3.3 shows a schematic illustration of the setup with the cooler probe inserted into the cone at 0° angle of attack.

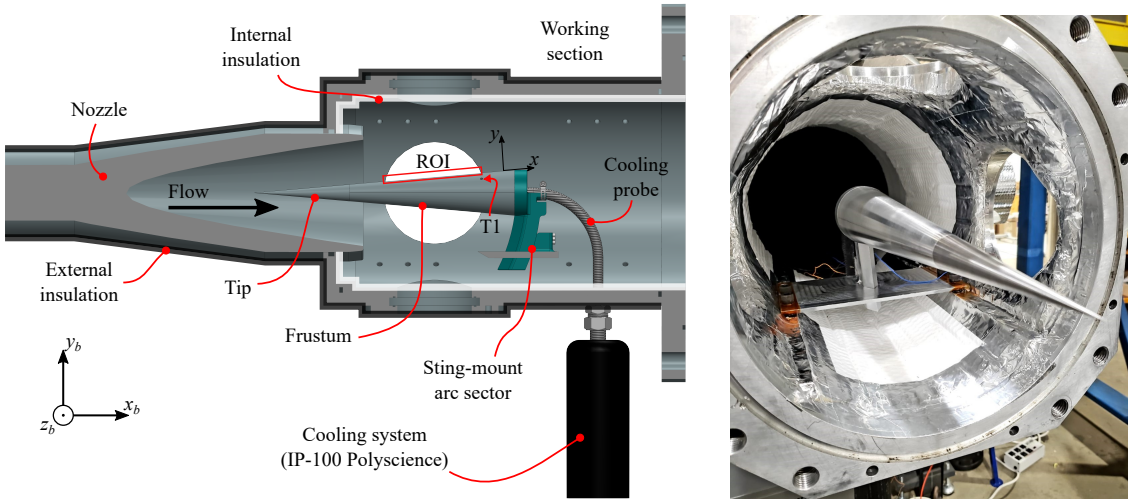

(a) Schematic of experimental setup

(b) Photo of cone

Figure 3.3: Model in test section

The highly-cooled conditions in this campaign required active cooling of the model and passive thermal management of the test environment. Active cooling involved two parts: contact with a cooling probe and test-section cooling with liquid nitrogen (LN_2). Passive thermal management involved extensive layering of insulation within and around the test section. Fig. 3.4 shows the overall setup. The PolyScience IP-100 cooling probe was installed through a port at the bottom of the test section, as shown in Fig. 3.4(a). Rated down to -100°C, the unit typically operated around -95°C. A liquid nitrogen tank on the port side of the dump tank delivered LN_2 at 22 psi through an injection control system consisting of a solenoid valve, pressure relief valve, and a cryogenic flow-adjustment valve. The LN_2 sprayed in a 30° cone via the injection lance, as shown in Fig. 3.4(b), and expanded through the dump tank and into test section. A valve with an air dryer allowed the pressure within the test environment to be controlled without adding humidity. Visible in Fig. 3.3(b), the inside of the test section was covered with two layers of 0.64-cm-

thick double-cell cryogenic insulation. Additional layers of insulation also covered the outside of the test section and nozzle.

Prior to a run, the cone was first cleaned with acetone and then wiped down with an anti-ice solution. Additionally, a cold-trap "jacket" made out of aluminum foil was placed on the cone for the cool-down process. When these techniques had not been employed, ice-like crystals typically formed along the surface of the cone by the time it had cooled to -35°C. A string attached to the jacket was routed out of the test section through a feed-through fitting.

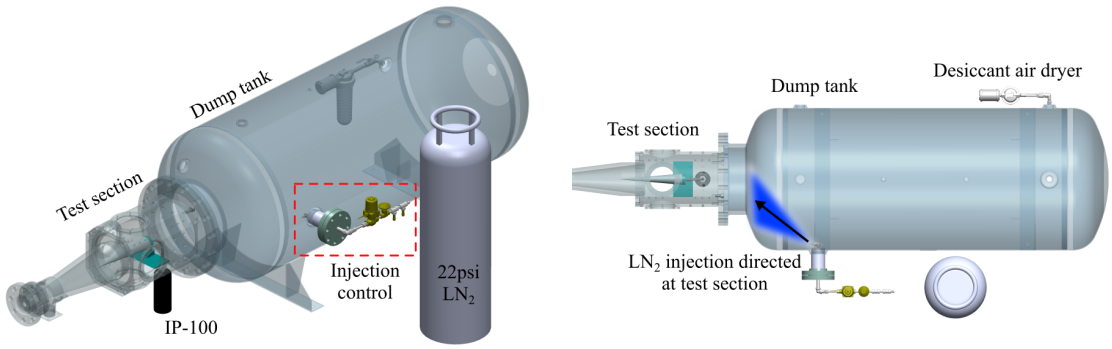

(a) Overall setup

(b) Top-down view of setup

Figure 3.4: Experimental setup

To estimate the cooling potential of this setup, a finite element thermal analysis was conducted in the SolidWorks 2018 simulation suite. The time-dependent thermal system was governed by Eq. 3.1,

$$\mathbf{M}\dot{\mathbf{T}} + \mathbf{K}\mathbf{T}(t) = \mathbf{Q}(t), \tag{3.1}$$

where $\mathbf{M}$ is the specific heat thermal mass matrix, $\mathbf{K}$ is the conduction and convection matrix, and $\mathbf{Q}$ the combined nodal heat flow vector due to internal sources/sinks

(cooling probe), conduction, convection, radiation, and heat flux. In this work, the magnitude of heat flux normal to the cone (and working section) surface due to free convection was determined as

$$q_h = hA_h(T_w - T_f), \tag{3.2}$$

where h is the convection coefficient, A_h is the local surface area in contact with the fluid, T_w is the surface temperature, and T_f is the temperature of the fluid. Contributions of cone heating from radiation (the dominant source limiting the cooling of the cone) is a highly non-linear function, where the magnitude of the heat flux normal to a solid surface was governed by:

$$q_r = \epsilon\sigma A_r(T_w^4 - T_f^4), \tag{3.3}$$

where T_w is the absolute temperature of the body surface, T_f is the absolute temperature of the surrounding fluid, A_r is the local surface area subjected to radiation, σ ($= 5.67 \times 10^8$ W/m^2 K^4) is the Stefan-Boltzmann constant, and ϵ is the surface emissivity (taken to be 0.1 for all surfaces). A convergence analysis was performed to ensure minimal discretization and solution errors. The material properties of all sections of the cone were taken to be isotropic.

Fig. 3.5 presents the predicted surface thermal profile over the length of the cone once thermal stability has been reached. Fig. 3.5(a) shows the predicted profile with probe cooling only, and Fig. 3.5(b) demonstrates the results when LN_2 is

introduced at 1 kPa, with the different curves representing ambient temperatures $-100 \leq T_{\text{amb}} \leq 0°\text{C}$. In all cases, cooling of the model plateaus due to radiative heating from the tunnel's aluminum nozzle and working section, which are in relatively close proximity to the cone. The probe-only simulation indicates that the groove temperature reaches -56.3°C, and the longitudinal thermal gradient between $0.51 \leq x_b/L \leq 1$ arises from the probe's consistent cooling along the model's narrowing cross-sectional density. At $x_b/L = 0.51$, coinciding with the tip of the cooling probe, the combination of the reduced cross-sectional area and increased thermal contact causes the brief range of enhanced cooling. For $x_b/L < 0.51$ there is no active cooling present, and the temperature of the cone increases rapidly with the aid of radiative heating. Furthermore, towards the tip of the cone, the thermal conductivity drops as the material transitions from aluminum to steel. With the addition of LN_2, every condition decreases the minimum temperature at $x_b = 0.51L$ to nearly $-100°\text{C}$, and the temperature range in the region of interest drops to less than $-90°\text{C}$. As the ambient temperature is decreased toward $-100°\text{C}$, the longitudinal profile becomes more uniform along the cone.

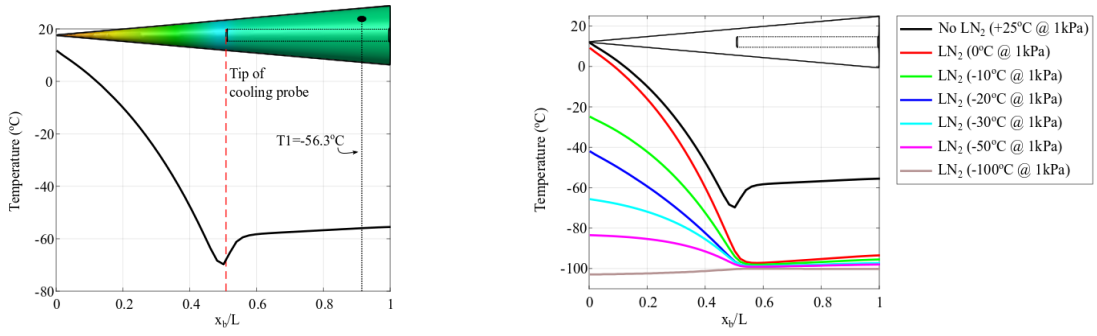

(a) Predicted temperature profile with IP-100

(b) Predicted temperature profile with LN_2 and IP-100

Figure 3.5: Cooling simulations

Fig. 3.6 demonstrates the experimental cool-down process before a run. Two thermocouples monitored model temperature. One was fed through a groove machined into the cone frustum, measuring surface temperature at $x_b/L = 0.88$ (shown in red). The other was fixed directly onto the surface of the nosetip, measuring temperature at $x_b/L \approx 0.34$ (shown in green). A third thermocouple was exposed to the gas in the test section and monitored the ambient temperature (shown in blue). Once the test section was pumped down to a vacuum, the PolyScience IP-100 cooling probe was powered on and used in isolation until the surface temperature began to plateau, as T_{groove} does near $-55°\text{C}$ at $t =$ 1:40:00. At this point the LN_2 cycle began. Because it took time for all the injection components to cool down, the system delivered a less-cold gaseous nitrogen at first, causing a rise in both pressure and temperature, as seen in T_{groove} and T_{tip} for 1:40:00 $\leq t \leq$ 1:50:00. When the components had cooled sufficiently, liquid nitrogen was delivered at 22 psi at an expected temperature around its boiling point, -196°C. The injection cooled the test-section ambient by roughly 30°C in 2 hours, and the model temperature continued to drop due to the combination of probe and LN_2 cooling. It was observed that maintaining a test-section pressure in the range 40-50 kPa provided the most effective balance of probe and injection cooling. If the full 240-liter tank of LN_2 as exhausted and more cooling was needed, the tank was swapped out for a second and the cycle was repeated, as shown at $t =$ 3:55:00. When the cone temperature was considered low enough, injection was stopped and the test section was pumped back down to a vacuum. Before the tunnel was fired, the string connected to the cold-trap jacket was pulled so that the model was exposed.

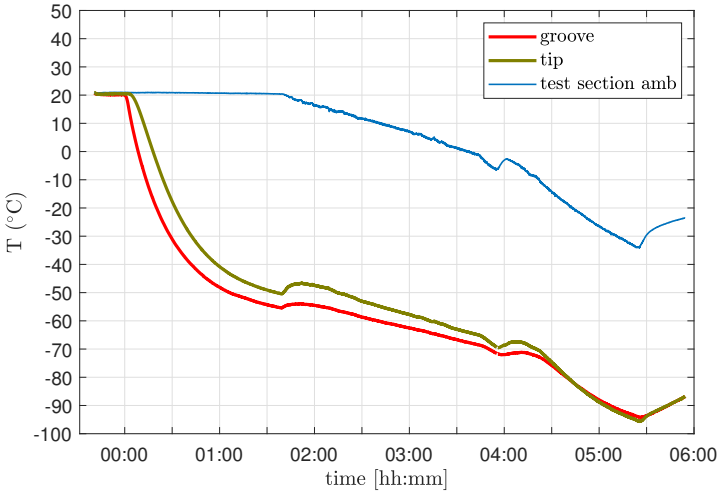

Figure 3.6: Cooling of cone and test section

Ultimately, three thermal conditions were chosen for testing: uncooled $T_w = 24°\text{C}$ (297 K), moderately-cooled $T_w = -32°\text{C}$ (240 K), and highly-cooled $T_w = -64°\text{C}$ (209 K). Here the wall temperature corresponds to that measured at the groove. The associated wall-to-edge temperature ratio, T_w/T_e, and number of shots performed at each condition are listed in Table 3.2. Due to the time required to cool down to $T_w = -64°\text{C}$, the matrix includes only two shots at this condition but four at the uncooled and moderately-cooled conditions.

Cooling Level	T_w **(K)**	T_w/T_e	**Number of shots**
uncooled	297 ± 1	2.34 ± 0.04	4
moderately-cooled	240 ± 4	1.88 ± 0.03	4
highly-cooled	209 ± 1	1.64 ± 0.01	2

Table 3.2: Cooling levels of experiments

3.3 Diagnostics

3.3.1 Calibrated Schlieren

Optical access on opposite sides of the test section allowed a modified Z-type schlieren system to image the boundary layer on the upper or lower surface of the cone, as shown in Fig. 4.1. A Cavilux HF laser generated a $\lambda = 640$-nm beam with a pulse width of 20 ns, and a pair of 152-mm-diameter spherical mirrors, 1.52-m in focal length, collimated and directed the beam through the test section. A knife edge placed a few centimeters in front of the camera lens served as the horizontal cutoff, and a Phantom 2512 high-speed camera captured 640×48-pixel schlieren images at 550 kHz. The schlieren system provided images with a scale of 7 pixels/mm.

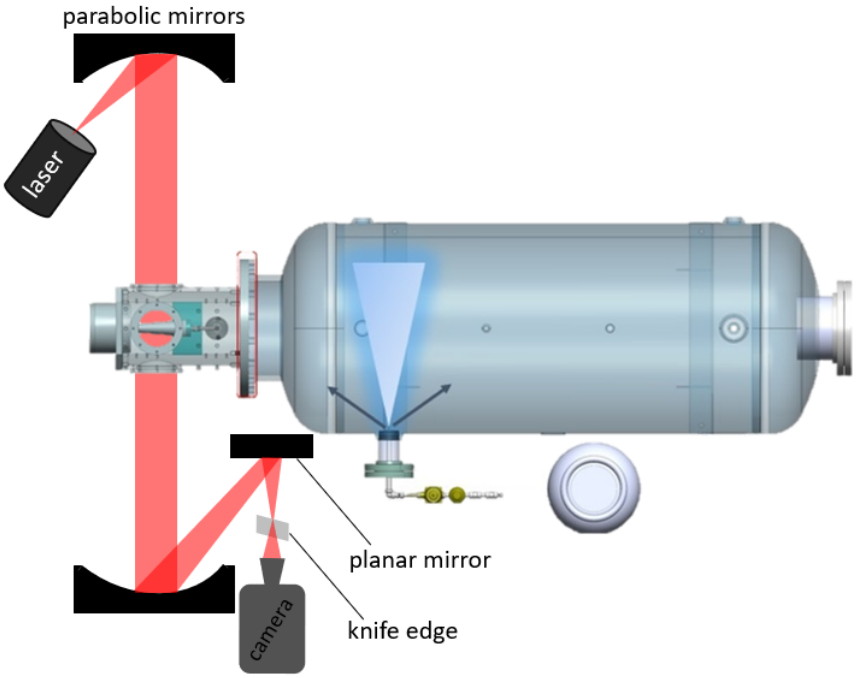

Figure 3.7: Schematic of schlieren setup

Prior to runs, two calibration images were taken for schlieren imaging: 1) of

marker objects on the cone to generate a mm/pixel scale, and 2) of a weak lens of a known density gradient to allow calibrated schlieren measurements, as discussed in Section 2.1.1 and also utilized in previous instability studies [82, 101, 102]. Fig. 3.8 demonstrates the calibration process in HyperTERP. The weak lens placed in the experimental field of view is shown in Fig. 3.8(a), and the lines drawn on the lens indicate where vertical intensity profiles I were extracted. These profiles were averaged to provide an I vs. r relationship, where r is the vertical distance from the geometric center of the lens. It is important to note that the geometric center ($r = 0$) corresponds to the location where no density gradient exists in the lens. As a result, light rays are not deflected and the intensity is equivalent to 92% of the background intensity due to the slight lens absorption discussed in Ref. [101].

To compensate for nonuniform background intensity, the calibration curve was shifted such that $I(r = 0)$ was equated to the time-resolved background intensity at each location. In this way, the ray deflection ε was related to the difference in intensity ΔI, where $\Delta I = I_{BL} - I_{BG}$, I_{BL} is the local intensity in the boundary layer, and I_{BG} is the local background intensity. The justification for this procedure was ealier measurements which showed that, in a schlieren image with nonuniform background intensity, to a reasonable approximation the calibration curve is essentially translated along the intensity axis. The resulting ε vs. ΔI curve for one lens calibration is displayed in Fig. 3.8(b). Outlined with a dashed line, the calibration is linear for $-500 \leq \Delta I \leq 2500$. The intensities for all runs conducted fell in this linear regime, so a simple proportionality was established to calibrate the intensities: $\varepsilon = \alpha \Delta I$.

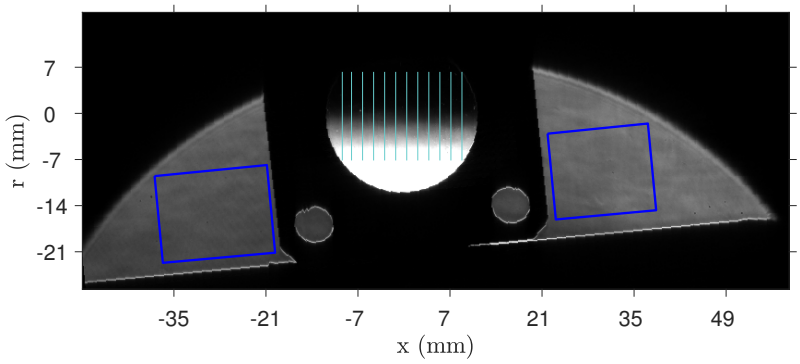

(a) Weak lens in field of fiew

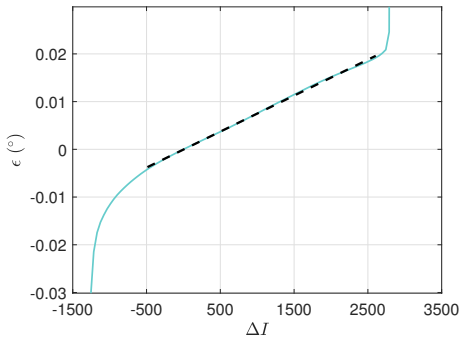

(b) Calibration curve for test

Figure 3.8: Calibration of schlieren images

3.3.2 Temperature-Sensitive Paint

Additional optical access on the top of the test section allows top-down illumination and imaging of the TSP surface on the upper half of the frustum, as shown in Fig. 3.9. For this system, a series of 462-nm LEDs provided the illumination for the paint, and an additional high-speed Phantom 2640 camera mounted above the test section captured images of the TSP emission at 30 kHz. For the TSP images, a 590-nm-centered bandpass filter with a full-width-half-max bandwidth of 60 nm was installed to isolate fluorescence from other sources of light. The top-down TSP-imaging system captured frames with a scale of 4.3 pixels/mm.

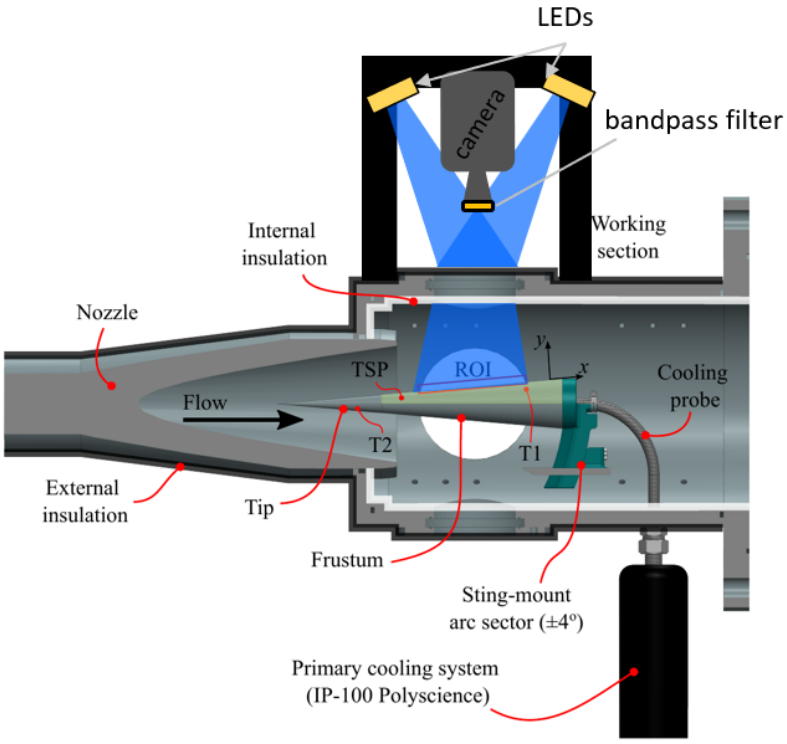

Figure 3.9: Schematic of TSP setup

As discussed in Section 2.2, a Ruphen-based paint mixture was sprayed onto a layer of adhesive film applied to the cone. Because the paint formula was based on that used in Ref. [98], the intensity-to-temperature calibration presented there was used for all uncooled runs. Cooled runs, however, provided a unique opportunity for in-situ calibration. Images were captured of the painted surface during the cool-down process, and the intensity of each image was correlated to the temperature recorded at the time. Fig. 3.10 displays the results of two cool-down processes compared to the Ruphen calibration curve adapted from Ref. [98].

There is a notable discrepancy in the curves: Both cool-down curves demonstrate the opposite concavity of the previous calibration for the temperature range $250 < T < 300$ K, and the cause of this discrepancy is not clear. A minor dis-

tinction between paint response while heating versus cooling has been observed before in Ref. [103]. The distinction was attributed to the thermal mass, and resultant lag, between thermocouple reading and painted surface, and the discrepancy was mitigated by slowing down the heating and cooling cycles. Hysteresis in the thermo-optical behavior of fluorescent paints has also been attributed to a change in polymer structure at its glass temperature [104, 105]; however, this phenomenon has not been characterized for the paint mixture at hand.

It is also to be noted that the TSP layer frequently exhibited degradation after and sometimes during cooled runs. Despite extensive efforts to maintain vacuum conditions during cool-down cycles and to fill the shock tube with only dry air between runs, the model would still accumulate frost after each experiment, causing the paint layer to appear blotchy. Some minor nonuniformities were also observed at times during the run. This meant that that a fresh coat of paint needed to be applied after each cooled run. Because of these challenges, TSP results on the cooled cone should be interpreted primarily qualitatively rather than quantitatively.

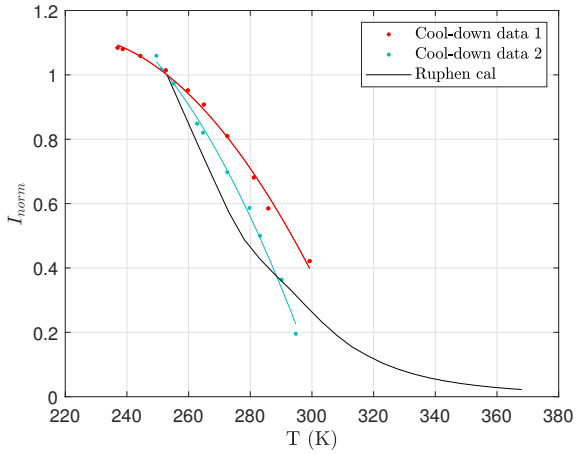

Figure 3.10: TSP calibration curves obtained before runs compared to previous Ruphen data

A three-layer Green's function routine was employed to calculate surface heat flux, as detailed in Ref. [9]. Table 3.3 enumerates the thicknesses and thermal properties assumed for each layer.

Layer	Thickness (mm)	Nominal material	ρ (kg/m^3)	C_p (J/kg K)	k (W/m K)
1	0.002	Ruphen polymer	1132	2070	0.20
2	0.1	PVC	1410	1000	0.15
3	76.2	Aluminum	2712	910	236

Table 3.3: Properties used in heat-flux calculation

3.4 Results & Discussion

3.4.1 Boundary-layer structures

Fig. 3.11 shows a series of reference-subtracted schlieren images from an uncooled run, and Fig. 3.12 shows a series from a highly-cooled run for which $T_w/T_e = 1.64$. The rope-like structures characteristic of second-mode instability waves are visible within the boundary layer throughout the extent of the field of view in both examples. Properties of the mean boundary layer and disturbances are provided in Table 3.4. The boundary-layer height, δ, was measured using a Sobel filter, as discussed in Ref. [84]. The height listed represents the average height measured over an 8-mm bin at center of the image, near $x = 360$ mm. Propagation speeds were calculated by cross-correlating image pairs containing wavepackets that were identified using a wavelet transform, similar to Refs. [81, 83, 84, 106]. The average number of wavepackets identified during a run at each condition is listed, along with the average computed speed u_p. Uncertainties were calculated using the standard deviation obtained for each set of wavepackets correlated. The uncooled

and moderately-cooled u_p varied by 4% and the highly-cooled calculation varied by 5%. As indicated, these second-mode disturbances propagate at around 88% of the edge velocity u_e. The waves in each schlieren series move approximately 8 mm between images, as indicated by the dashed propagation arrows. In the uncooled case, the waves appear quite rounded and grow taller as they move downstream toward $x = 393$ mm. Confined to a thinner boundary layer, the wavepackets in the highly-cooled case appear straighter and smaller in both streamwise and vertical extent. Unlike the large billowing structures in Fig. 3.11, these instabilities appear as a series of light and dark streaks that lie close to the surface, as noted in Ref. [84]. At the downstream end of the first two frames $t = 2.434 - 2.448$ ms, the structures become less organized, and a large swell can be seen moving from $x = 385$ to 393 mm. In the latter two frames, faint streaks in the top half of the field of view for $x = 388 - 402$ mm (labeled with dotted arrows) indicate the radiation of some disturbances out of the boundary layer and the beginning of breakdown to turbulence.

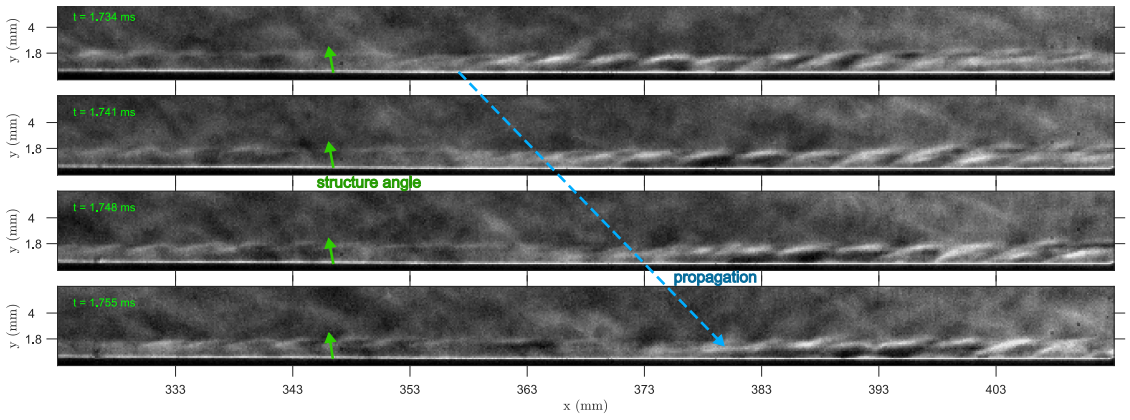

Figure 3.11: Second-mode wavepacket propagating at $T_w/T_e = 2.38$ condition

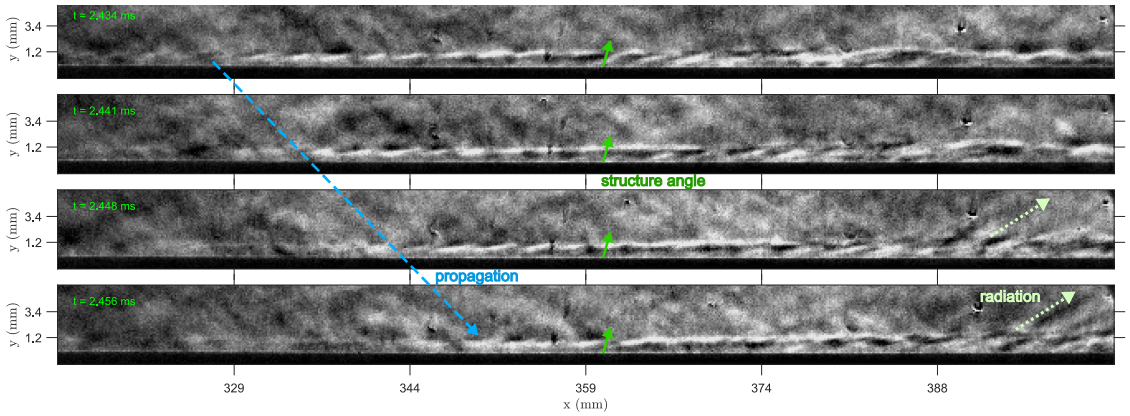

Figure 3.12: Second-mode wavepacket propagating at $T_w/T_e = 1.64$ condition

T_w/T_e	δ **(mm)**	u_p **(m/s)**	u_p/u_e	**average number of wavepackets identified**
2.34±0.04	1.55	1120±40	0.89	1660
1.88±0.03	1.37	1110±40	0.88	2450
1.64±0.01	1.21	1090±50	0.87	2970

Table 3.4: Cooling levels and associated boundary-layer/disturbance characteristics

Boundary-layer heights were predicted using similarity solutions computed for each run, assuming hypersonic similitude as in Refs. [107, 108] and the $\sqrt{3}$ transformation introduced by Mangler [109]. The results, normalized by edge velocity u_e and temperature T_e, for one uncooled ($T_w/T_e = 2.38$) and one highly-cooled ($T_w/T_e = 1.64$) case are shown in Fig. 3.13. Each solution assumed a sharp 5° cone in Mach-6 flow, but post-shock and edge conditions were calculated based on the reservoir conditions for the specific run. From schlieren images, boundary-layer height was measured at discrete locations along the field of view for each run, and the results are displayed in Fig. 3.14(a) along with a representative $\delta \propto \sqrt{x}$ curve. As could be expected, decreasing T_w/T_e decreases δ. Moving downstrean, all profiles grow quite similarly to the expected $\delta \propto \sqrt{x}$ behavior. Additionally, the measured

boundary-layer height at $x = 350$ mm was compared to that computed from similarity solutions at this location for each case. The results are shown in Fig. 3.14(b). The results for the uncooled cases match the similarity solution extremely well, with an average discrepancy of less than 1%. The moderately-cooled cases show good agreement as well, with an average discrepancy of 5% of measured δ. In the highly-cooled set, the similarity solution δ exceeds the measured value by an average of 15%; however, this discrepancy corresponds to approximately 1 pixel of difference. Thus, it is demonstrated that the Sobel filtering method provides a generally reliable way to measure δ.

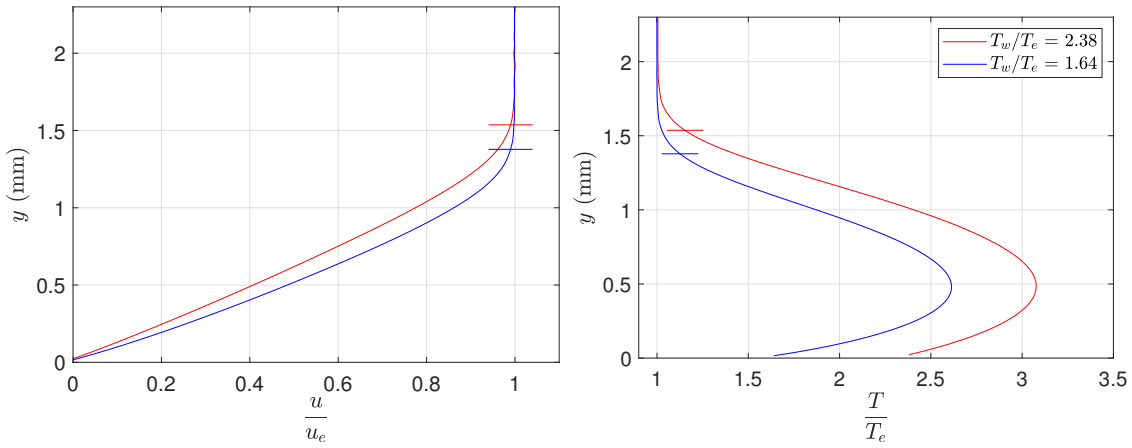

(a) Boundary-layer velocity profile

(b) Boundary-layer temperature profile

Figure 3.13: Similarity solutions computed for uncooled and highly-cooled cases

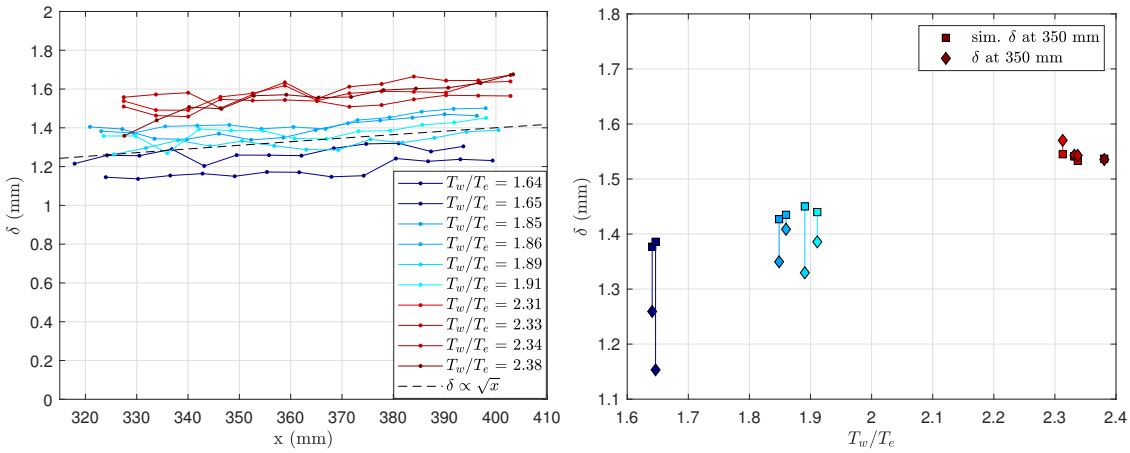

(a) Measured boundary-layer height across field of view

(b) Boundary-layer height comparison with similarity solution

Figure 3.14: Boundary-layer height measurements

The structure angle of wavepackets is defined as the orientation of waves relative to the wall where $\theta = 0°$ lies along the cone surface in the flow direction, $\theta = 90°$ is the surface normal, and $\theta > 90°$ represents backwards-leaning structures. Angles were calculated by cross-correlating neighboring rows of intensity from wavepacket regions within frames. The results for wavepackets contained in the region $335 \leq x \leq 385$ mm are compiled in Fig. 3.15. The average number of wavepackets lying in this region per run was as follows: 160 (uncooled), 300 (moderately-cooled), and 960 (highly-cooled). The main distinction among the cases is the angle directly above the wall, θ_{wall}, and arrows representative of θ_{wall} are included in Figs. 3.11-3.12. For uncooled cases, The structure angle begins at $\theta = 95 - 100°$, meaning that, close to the wall, the waves actually lean slightly backwards. This can be seen in Fig. 3.11 for $338 \leq x \leq 353$, where the waves appear to point upstream in the lower half of δ but then curve over near the top of the boundary layer. For moderately cooled cases, the near-wall angle is closer to 90°,

meaning that the waves are more vertical at their base. Finally, for the highly-cooled cases, θ begins in the range $74 - 82°$, meaning that waves lean downstream at this condition. This results reflects the behavior observed in Fig. 3.12, where streaks can be traced from the cone floor diagonally up and to the right through δ. In all cases, wavepackets are largely vertical for $y = 0.2 - 0.4\delta$, and then θ decreases for $y = 0.4 - 0.7\delta$, indicating the roll-over of the structures near the top of the boundary layer. The trend back to $\theta = 90°$ for $y = 0.7 - 1.0\delta$ is most likely due to the apparent vertical "thickness" at the tops of waves. For example a pattern of pixel intensity spanning more than one row in vertical extent would lead to a $\theta = 90°$ result.

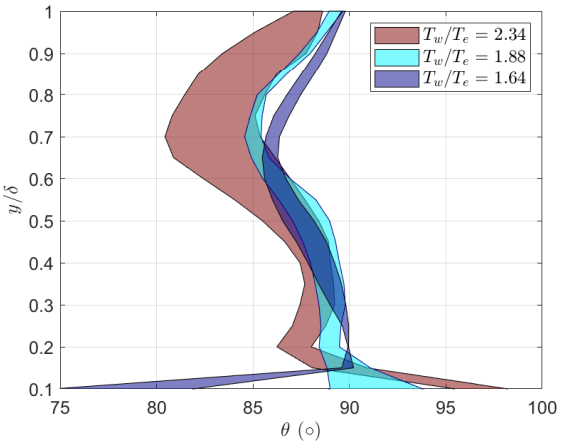

Figure 3.15: Structure angle comparison

3.4.2 Spectral analysis

The methodology described in Refs. [83, 102] was employed here to analyze spectral content. Temporally-resolved pixel signals were reconstructed using neighboring pixel information and the determined propagation speeds, and Welch's method was used to generate power-spectral density (PSD) estimations for the re-

constructed density fluctuations. For these calculations, 50% overlap was used, and a Blackman window was applied to segments 1/60 of the length of the total timespan, resulting in an average of 0.1 ms per segment. The N factor was then computed according to

$$N(f,x) = 1/2 \ln y(f,x) + C(f), \tag{3.4}$$

where $y(f,x)$ is the PSD power of a given frequency f at each location x, and $C(f)$ is a constant depending on the disturbance amplitude at the neutral stability point for the frequency. Because this constant is unknown, ΔN is shown here, with the y-intercept $\Delta N = 0$ set at $Re = 1.72 \times 10^6$ for all the runs. Fig. 3.16 exhibits the evolution of ΔN over the field of view for one run at each wall-temperature condition. Fig. 3.16(a) shows the gradual growth of second-mode content in the uncooled case. By $Re = 2.1 \times 10^6$, a peak has developed around $f = 280$ kHz and the spectrum is extending over the range $f = 240 - 330$ kHz. At the same location, low-frequency content ($f \leq 200$ kHz) grows in strength. The moderately-cooled example shown in Fig. 3.16(b) exhibits the largest change in N of all three cases. Disturbance energy is first visible at $Re = 1.8 \times 10^6$ and grows to encompass $250 \leq f \leq 340$ kHz at $Re = 2.01 \times 10^6$. The maximum ΔN is experienced for $f = 300$ kHz at $Re = 2.03 \times 10^6$, at which point higher-frequency content begins to taper off. In the highly-cooled case in Fig. 3.16(c), the disturbance spectrum expands to $f = 310 - 380$ kHz by $Re = 1.96 \times 10^6$. The strength ΔN of the peak frequency at $f = 350$ kHz plateaus over the region $Re = 1.96 - 2.0 \times 10^6$. From the side-by-side comparison of these three contours, it is clear that cooling pushes the

lobe of second-mode content upstream.

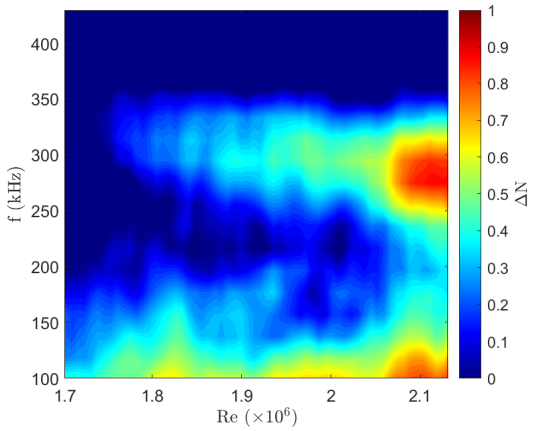

(a) N factor contour for $T_w/T_e = 2.33$

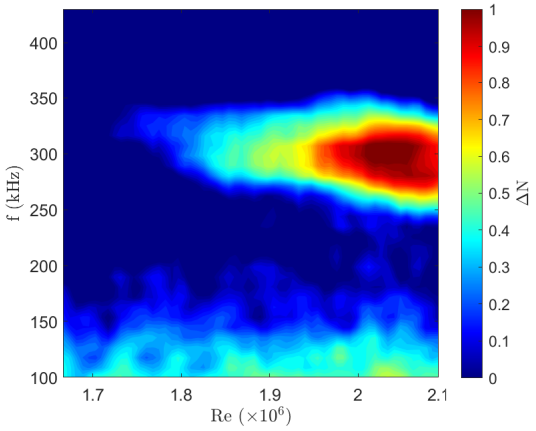

(b) N factor contour for $T_w/T_e = 1.86$

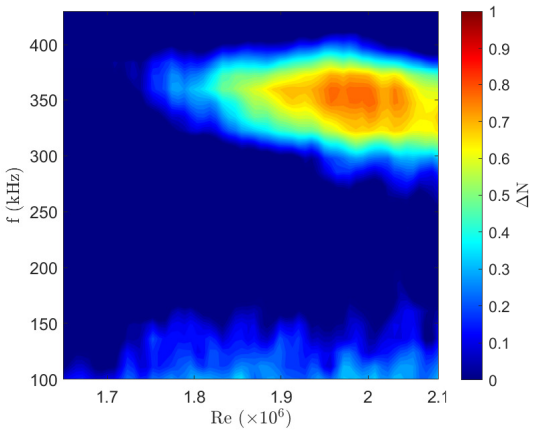

(c) N factor contour for $T_w/T_e = 1.64$

Figure 3.16: N factor contours

Peak frequencies were extracted by identifying the maximum spectral amplitude experienced at each location along the cone. Fig. 3.17 plots the peak frequencies from the disturbance spectra calculated at each point along the cone, as well as associated ΔN for each peak frequency.

Although the expected trend was for frequency to increase with wall cooling, this is not strictly observed. As seen in Fig. 3.17(a), two runs in the moderately-cooled category, $T_w/T_e = 1.89$ and 1.91, exhibit frequencies equal to or higher than those obtained in the coldest-wall conditions, $T_w/T_e = 1.64 - 1.65$. However, these two runs appear to be outliers, and it is not entirely clear what caused these anomalously high frequencies. The author suspects one possibility these two runs diverged from the other two cooled cases could be that the nosetip was slightly colder than the frustum. Although the temperatures of the two pieces (i.e. T_{groove} and T_{tip} from Fig. 3.6), were always within a few °C of one another, the effect of this minor gradient is still unknown. Additionally, it is noted that the two outlier runs were consecutive, so it is possible that there was some issue with the experimental apparatus that affected them in particular. These two runs were removed from the subsequent ΔN comparison.

The ΔN curves in Fig. 3.17(b) reflect the spectral power of each peak frequency identified in Fig. 3.17(a). Similar to the trend seen in Fig. 3.16, the curves show that cooling pushes the point of spectral saturation upstream. While all the uncooled runs, $T_w/T_e = 2.31 - 2.38$, show a positive slope for the extent of the field of view, every cooled example demonstrates a peak and subsequent decrease in calculated ΔN values. The moderately-cooled runs, $T_w/T_e = 1.85 - 1.86$, reach their peak

between $2.00 \leq Re \leq 2.05 \times 10^6$, but the highly-cooled runs, $T_w/T_e = 1.64 - 1.65$, plateau in the range $1.87 \leq Re \leq 1.94 \times 10^6$. Additionally, the highly-cooled examples indicate a more extended region of saturation than the moderately-cooled ones do. For example, ΔN for $T_w/T_e = 1.64$ and 1.65 plateau for a span of roughly $\Delta Re = 0.05$ whereas the ΔN curves for $T_w/T_e = 1.85$ and 1.86 appear to immediately drop after reaching their peaks.

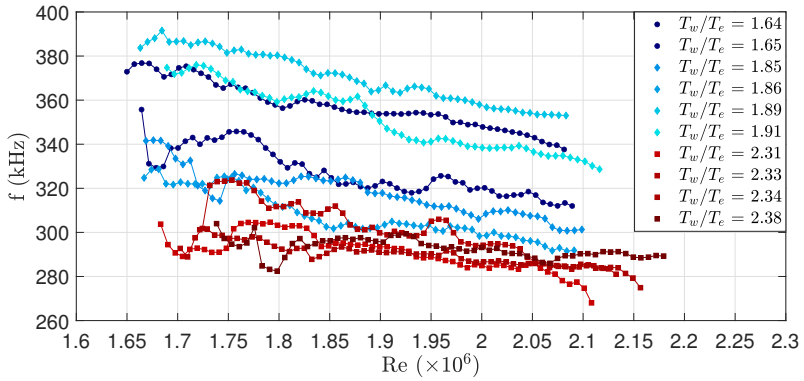

(a) Peak frequency comparison

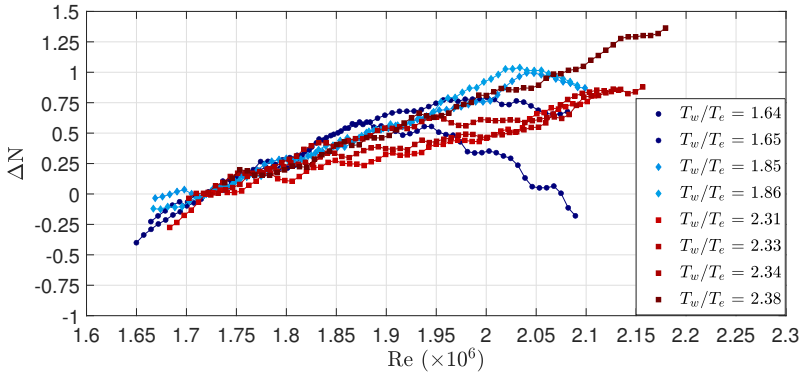

(b) N factor curve

Figure 3.17: Peak frequencies and associated N factor curves

To estimate the growth rates at these most amplified frequencies, a straight-line was fit to portions of the N-factor curves where linear growth was observed. For the uncooled and mildly-cooled cases, this region spanned $1.72 \leq Re \leq 2.0 \times 10^6$, while for the highly-cooled cases, data between $Re = 1.72 \times 10^6$ and the point of

saturation was used. The range of slopes calculated for the three thermal conditions is displayed in Fig. 3.18, where the filled regions are bounded by the maximum and minimum growth rates, $\Delta N/\Delta Re$, calculated for each set of runs. The average growth rate for each set is shown as a dashed line. The results for the two highly-cooled cases lie close to one another, with $\Delta N/\Delta Re$ differing by only 8% of one another. By including the two outlying runs in this data set, the spread of the moderately cooled results increases significantly, but the average growth rate still lies below the range of the highly cooled experiments. Thus, overall, the average slopes indicate that increasing wall-cooling causes an increase in $\Delta N/\Delta Re$, as would be expected with a destabilized second-mode.

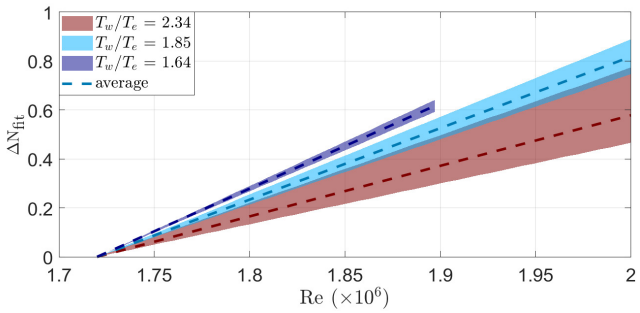

Figure 3.18: Linear fit of N factor curves

One final goal of the spectral analysis was to compare the competing effects of growth rates and receptivity. To evaluate the receptivity of the boundary layer, spectral amplitudes of calibrated density fluctuations were compared. Results are shown in Fig. 3.19. One run, $T_w/T_e = 1.65$, was excluded from this analysis because the optical setup appeared to change significantly between the calibration image and the run, invalidating the calibration curve. Fig. 3.19(a) compares the PSD estimates calculated at an upstream location, $Re = 1.75 \times 10^6$, for each run. As

shown, the coldest case $T_w/T_e = 1.64$ exhibits the highest spectral amplitude of all the runs, with its peak at $f = 370$ kHz an order of magnitude higher than that of the uncooled cases. The moderately-cooled $T_w/T_e = 1.91$ also displays a 370-kHz peak of similar amplitude, and the $T_w/T_e = 1.89$ case demonstrates highest-frequency peak at 390 kHz but at a notably lower amplitude. The other two moderately-cooled cases ($T_w/T_e = 1.85 - 1.86$) exhibit amplitudes similar to those experienced in uncooled cases. Thus, at least within this field of view, there is no evidence of a diminished receptivity in the cooled cases. Additionally, it is important to note that freestream characterization of the tunnel with FLDI revealed lower density-fluctuation amplitudes at higher frequencies in the core flow, as discussed in Ref. [110]. For example, the strength of density fluctuations at $f = 370$ kHz in the freestream is expected to be 33% lower than that at $f = 300$ kHz, as the fluctuations ρ'/ρ_∞ scale with wavenumbers k according to $\rho'/\rho_\infty \propto k^{-1.8}$ in this range.

Fig. 3.19(b) plots the amplitudes corresponding to the peak frequencies (i.e. those plotted in Fig. 3.17(a)) at each Re for all the runs. As shown, the uncooled and most of the moderately-cooled runs begin around the same amplitude. The $T_w/T_e = 1.64$ and 1.91 cases begin slightly higher, but the $T_w/T_e = 1.64$ run rises sharply until about $Re = 1.95 \times 10^6$, whereas the $T_w/T_e = 1.91$ plateaus in amplitude until $Re = 1.9 \times 10^6$ where it begins its sharp rise, as does the $T_w/T_e = 1.89$ case. Overall, these plots suggest that any decrease in receptivity for the cooled boundary layer, as predicted by Kara [57], was outweighed by the increased growth rate of these disturbances.

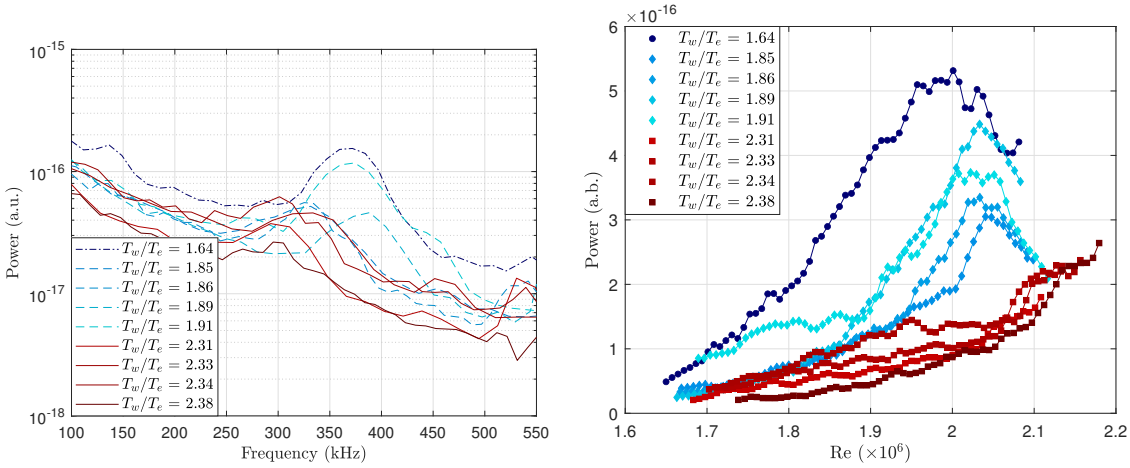

(a) PSD of signal at $Re = 1.75 \times 10^6$ (b) Amplitude of peak frequencies along cone

Figure 3.19: PSD amplitude comparison

Despite some scatter obtained within the moderately-cooled data set, these results do overall seem to support the conclusion from Ref. [2]: Wall-cooling tends to destabilize the second-mode at least to some extent for the lower-T_w/T_e cases. At this point the opposition between this conclusion and that found by Oddo et al. in Ref. [88] is unknown. It is possible that the thermal gradient between cone base and tip acknowledged in Ref. [88] could have altered the stability characteristics observed, or that the expected decrease in receptivity outweighed the destabilizing effects of cooling. One surprising implication could be that HyperTERP is quieter at the relevant frequencies than the AFRL Ludwieg tube employed in the work by Oddo et al. [88].

3.4.3 Temperature-Sensitive Paint Analysis

The resulting heat-flux contours averaged over the test time for cooled and uncooled runs at 0° and 4° angles of attack α are shown in Figs. 3.20 and 3.22.

Unfortunately image saturation occurred over a large region of the frames from the $\alpha = 0°$, $T_w/T_e = 1.87$ run; for this reason, only half of the field of view is shown in Fig. 3.20(c), and some data near the centerline was removed.

Despite the corruption due to saturation in Fig. 3.20(c), the cooled contours, $T_w/T_e = 1.87 - 1.90$, exhibit heat-flux profiles unique from $T_w/T_e = 2.32$. Centerline profiles were constructed from the intensities at $z = 0 \pm 2$ mm, and the results for the three $\alpha = 0°$ cases are shown in Fig. 3.21. The dashed line in the $T_w/T_e = 1.87$ curve indicates that data from the region most affected by saturation was removed. The profile from the uncooled case shows that the centerline heat flux drops by about 30% over the region $280 \leq x \leq 380$ mm, which would be expected for a laminar boundary layer that grows fuller in the downstream direction. The cooled cases, however, do not reflect this trend. For example, the $T_w/T_e = 1.90$ curve reaches its maximum at $x = 320$ mm and then drops in the downstream direction. The $T_w/T_e = 1.87$ case exhibits an apparent rise in heat flux at the downstream end of the cone, which could be indicative of the onset of transition; however, it is difficult to draw definite conclusions from these data.

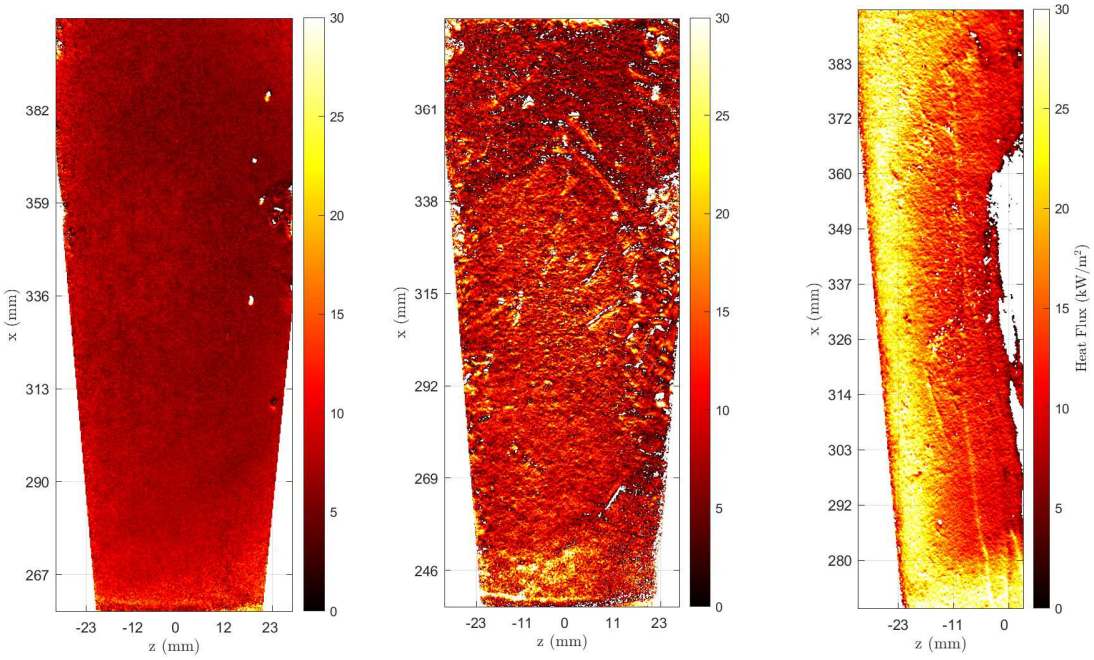

(a) $T_w/T_e = 2.32$ run (b) $T_w/T_e = 1.90$ run (c) $T_w/T_e = 1.87$ run

Figure 3.20: Mean heat flux contours for $\alpha = 0°$ condition

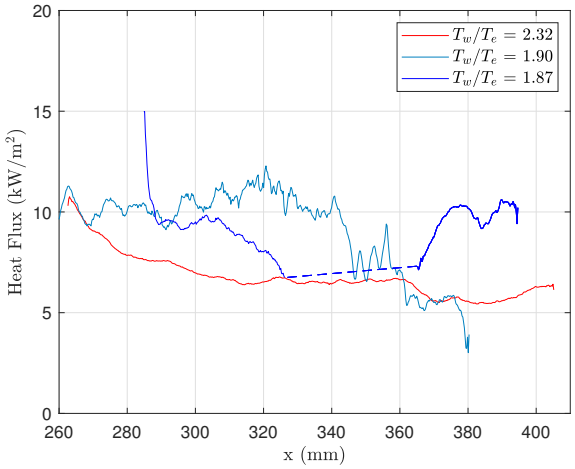

Figure 3.21: Centerline heat flux profiles at $\alpha = 0°$

Fig. 3.22 shows the average heat-flux contours for the leeward side of the cone during two $\alpha = 4°$ runs. As discussed, some non-uniformities are present in the cooled case shown in Fig. 3.22(b), especially in the range $260 \leq x \leq 280$ mm. Since it is expected that the surface heat flux would be highest for the most-cooled condi-

tion, the overall level of heat flux computed for the cooled case is considered too low to be physical. Discussion of these results will focus on qualitative spatial features instead of quantitative heating values. Despite the limitations of the method, TSP imaging is utilized to characterize two-dimensional flow topology, similar to previous studies [111, 112].

In both cases, notable high-heating streaks lie on either side of the centerline. Outboard of these streaks, darker bands indicate regions of low heating, but the heat flux rises back up toward the sides of the cone. In the uncooled case, the high-heating streaks appear to decay moving in the streamwise direction over the region $290 \leq x \leq 320$ mm and then rise back slightly by the aft end of the frame. In this region of decay, the lobes on either side of the centerline divide into narrow streaks, especially visible around $x = 300$ mm. The cooled case shows less contrast with little change in the streamwise direction.

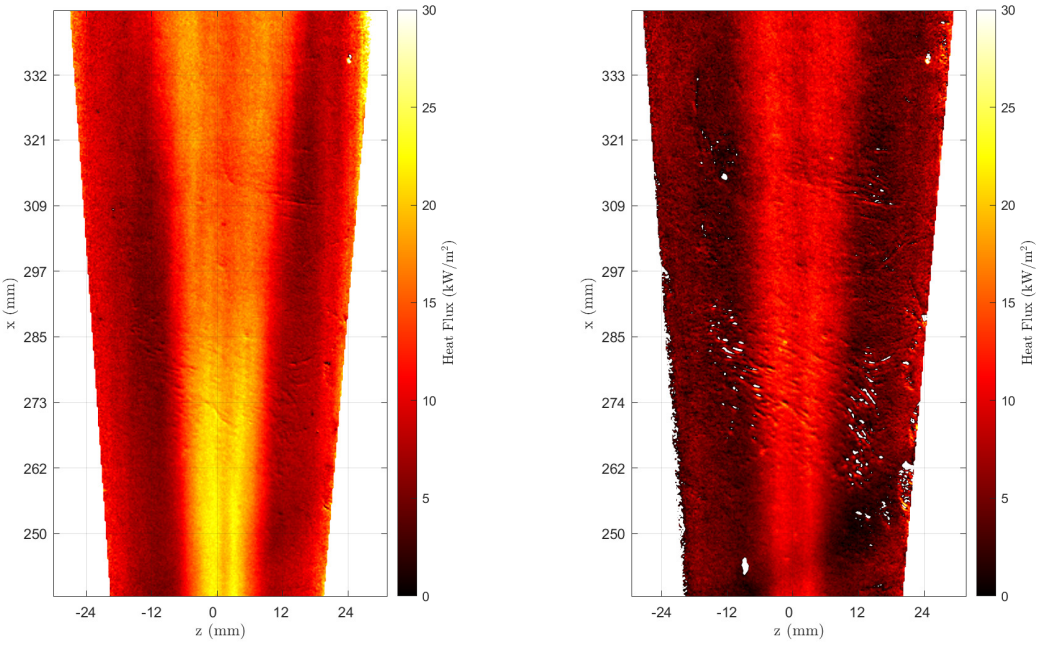

(a) Mean heat flux contour for $T_w/T_e = 2.32$ run

(b) Mean heat flux contour for $T_w/T_e = 1.91$ run

Figure 3.22: Mean heat flux contours for $\alpha = 4°$ condition

Fig. 3.23 compares the centerline profiles. The $T_w/T_e = 2.32$ curve shows that the highest heating occurs near $x = 250$ mm along the centerline and the flux drops by over 25% moving toward 320 mm. As could be expected from the contour, the $T_w/T_e = 1.91$ curve shows little change over the 100-mm range. The maximum heating does appear to be slightly farther downstream, at $x = 280$ mm, and the flux decreases slightly as the aft end is approached.

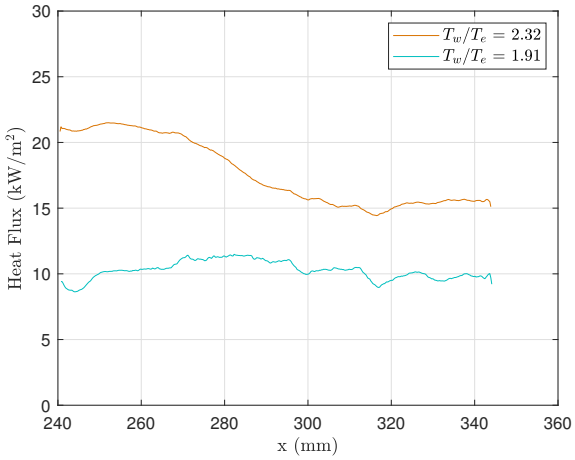

Figure 3.23: Centerline heat flux profiles at $\alpha = 4°$

Schlieren images taken simultaneously with the TSP images depict fully turbulent and most-likely separated flow for $264 \leq x \leq 354$ mm at both $\alpha = 4°$ runs. Based on Stetson's separation criterion for sharp cones, $\alpha/\theta_c \geq 0.7$ (where θ_c is the cone half angle), boundary-layer separation is expected here [113]. Fig. 3.24 shows reference-subtracted schlieren snapshots. In a study of a 7° cone at $\alpha = 6°$, Swanson and Schneider saw similar streaks of high heating on either side of the leeward ray and suggested that they may be due to separation vortices [112]. It is possible that some schlieren images show the signature of intermittent separation. For example, the first snapshots in Figs. 3.24(a) and 3.24(b) show a structure extending from the wall out into the flow over the span of 25 mm. Arrows indicate the direction of this structure. The pattern of high and low heating streaks could be attributed to the counter-rotating vortex structure associated with separation on conical geometries [113, 114].

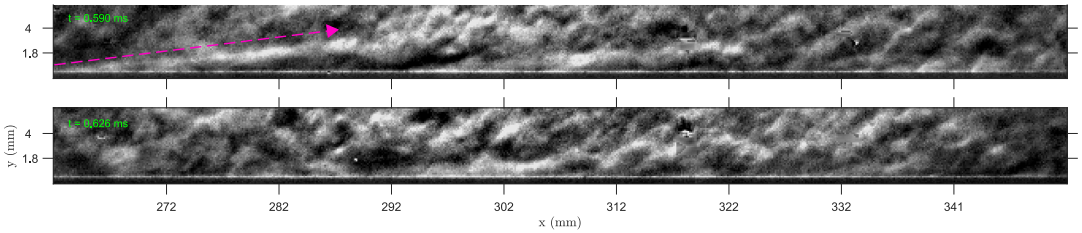

(a) Schlieren at $T_w/T_e = 2.32$

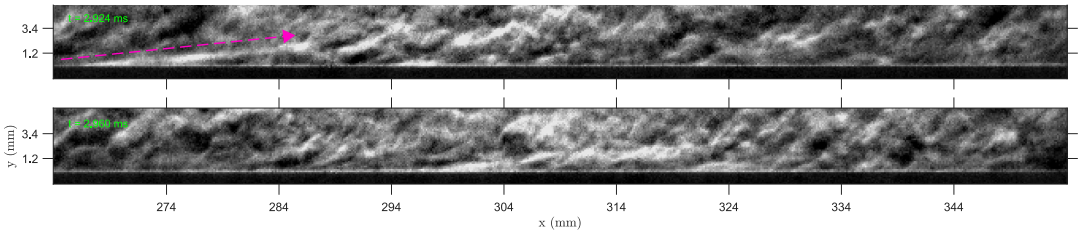

(b) Schlieren at $T_w/T_e = 1.91$

Figure 3.24: Schlieren images from $\alpha = 4°$ condition

Finally, spanwise heat flux profiles were extracted at discrete streamwise stations on each example at $\alpha = 4°$. The results shown in Fig. 3.25 further quantify the observances from Fig. 3.22. In the uncooled case in Fig. 3.25(a), spanwise profiles decrease in heat flux until $x = 311$ mm and then rise back up slightly. Irregularities can be seen in the increasing portion, $-5 \leq z \leq 0$ mm, of the $x = 311 - 337$ mm profiles. These irregularities, such as the small drop near $z = -2$ mm in the $x = 337$ mm profile, correspond to the narrow streaks that appear within the high-heating band in the contour. In the cooled case in Fig. 3.25(b), the profiles rise in heat flux until $x = 285$ mm, but the overall change is less significant. Although no evidence of the narrow heating bands seen in Fig. 3.25(a) are identified in this case, most profiles exhibit a small kink in their descent before reaching the minimum heat flux. For example, the $x = 245$ mm profile decreases over the range $z = 3 - 7$ mm, then rises slightly before sinking to its minimum at $z = 11$ mm. These kinks indicate the

presence of a weak auxiliary heating streak outboard of the main heating lobe on either side of the centerline. Locations of minimum heat flux were identified in each of these plots. By concatenating these locations, planar rays of minimum heating were constructed. For the uncooled case, minima in heat flux are observed at angles of $\phi_p = \pm 3.5°$ relative to the centerline in this top-down plane. For the cooled case, minima are observed at $\phi_p = \pm 4.1°$, and the auxiliary streaks lie at $\phi_p = \pm 3.9°$. These have not been converted to cone azimuthal angles.

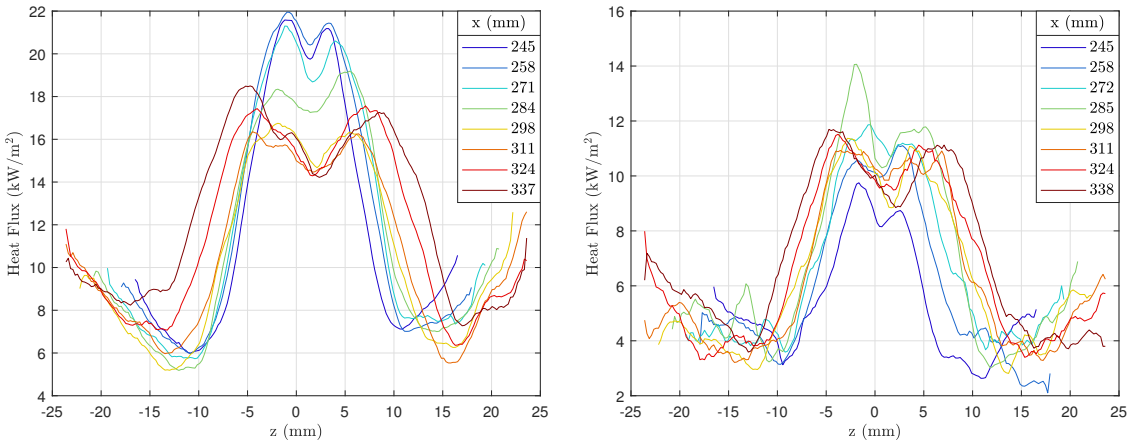

(a) Spanwise profiles for $T_w/T_e = 2.32$ run

(b) Spanwise profiles for $T_w/T_e = 1.91$ run

Figure 3.25: Spanwise heat flux profiles for $\alpha = 4°$ condition

3.5 Conclusions

An experimental methodology was developed to study the effect of wall temperature on boundary-layer stability. A cooling system comprising probe cooling, liquid nitrogen injection, and thermal insulation, proved capable of decreasing wall temperatures by 90 K relative to an uncooled state. Wavepacket structure, boundary-layer stability, and surface heating were characterized through calibrated schlieren and temperature-sensitive-paint imaging on a slender cone at Mach 6,

$Re = 5.2 \times 10^6 \mathrm{m}^{-1}$, and $\alpha = 0°$ and $+4°$. Three discrete wall-temperature conditions, $T_w/T_e = 1.64$, 1.88, and 2.33, were analyzed. Instabilities in cooled conditions manifested as relatively straight streaks of alternating dark/light intensity confined to a small boundary layer, as compared to the billowing waves seen in the uncooled conditions. Measurement of boundary-layer height δ showed that increasing the level of cooling decreased the boundary-layer thickness at a rate similar to that expected from similarity solutions calculated for each run condition. The decrease in wall temperature was also associated with a decrease in the structure angle of disturbances right at the wall. While uncooled wavepackets leaned slightly upstream with $\theta = 95 - 100°$ near the wall, waves at the moderately-cooled condition exhibited a more vertical profile, and highly-cooled structures leaned downstream with structure angles $\theta < 83°$. Apart from two anomalous runs in the moderately-cooled set, cooling increased the frequencies associated with second-mode disturbances. Over the region $1.65 \leq Re \leq 2.1 \times 10^6$, the uncooled set, $T_w/T_e = 2.31 - 2.38$, exhibited peak frequencies in the range $270 \leq f \leq 325$ kHz. The (non-anomalous) moderately-cooled cases, $T_w/T_e = 1.85 - 1.86$, experienced peak frequencies $290 \leq f \leq 340$ kHz within the same region, and the highly-cooled set, $T_w/T_e = 1.64 - 1.65$, spanned $310 \leq f \leq 380$ kHz. It was also shown that cooling increased spectral amplitudes and growth rates, moving the point of spectral saturation upstream. A PSD comparison demonstrated that the coldest case, $T_w/T_e = 1.64$, exhibited the highest power overall for the extent of the field of view. Uncooled runs exhibited the lowest spectral powers, and moderately-cooled spectra grew to intermediate amplitudes by $Re = 2.05 \times 10^6$. The uncooled cases exhibited fully-laminar flow with

no sign of saturation, as seen in N-factor curves and the representative heat-flux contour. The moderately-cooled runs, however, peaked in ΔN at $Re = 2.03 \times 10^6$, and the highly-cooled runs demonstrated a lengthened saturation stage in the range $1.87 \leq Re \leq 1.94 \times 10^6$. Thus, any reduction in boundary-layer receptivity due to cooling at these conditions was more than compensated by the increased growth rate of the disturbances.

Although the TSP results suffered from degradation due to the cooling process, heat-flux contours still showed distinctions due to cooling at both angles of attack. At $\alpha = 0°$, the gradual decrease in heating along the centerline expected for a laminar boundary layer was seen at $T_w/T_e = 2.32$ but not at $T_w/T_e = 1.87 - 1.90$. Instead, these cases exhibited centerline heat-flux profiles which appeared to increase over some extent in the downstream direction. When the cone was pitched at $\alpha = 4°$, high-heating streaks appeared on either side of the leeward ray for all cases, serving as potential indicators of separation vortices. Schlieren images demonstrated the fully-turbulent state of the boundary layer and suggested separation as well. The uncooled case experienced a distinct drop in centerline flux over the range $x = 245 - 300$ mm whereas the cooled case showed a slight rise. Minima in heating were detected at angles (relative to a top-down plane) of $\phi_p = 3.5°$ in the uncooled cases and $\phi_p = 4.1°$ in the cooled case, indicating a slight expansion of the azimuthal extent of separated flow.

Chapter 4: High-Enthalpy Tests in T5

4.1 Facility & Setup

All testing for the second part of the study was conducted in the T5 reflected shock tunnel at the California Institute of Technology. In this section, two campaigns are highlighted, with the main difference between them being the imaging system used. In the first campaign, referred to hereafter as the "Campaign A," the frame rate was limited to 160 kHz. In the second campaign, "Campaign B," two new cameras were introduced, and the frame rate could be increased up to 875 kHz. The bulk of the analysis provided currently is from Campaign A, but some results from Campaign B are included as well.

The facility design and operation are detailed in Ref. [115] and summarized here briefly. Moving in the downstream direction, the tunnel can be segmented into the following components: secondary reservoir, piston, compression tube (CT), primary diaphragm, shock tube (ST), secondary diaphragm, contoured nozzle, test section, and dump tank. Before a shot, the test section, dump tank, and both tubes are evacuated. Then the ST is filled with air to desired test-gas pressure P_1, and the CT is filled with an argon/helium mixture to the desired driver pressure P_{CT}. Finally the secondary reservoir, upstream of the piston, is filled with compressed

air to a specified gage pressure P_{2R}, typically around 1200 psi. Once exposed to the pressure in the secondary reservoir, the 120-kg piston travels downstream, adiabatically compressing the driver gas mixture to a desired value P_4. At this point the pressure difference between the driver gas in the CT and the test gas in the ST is high enough to burst the primary stainless-steel diaphram. A shock wave travels through the ST at a speed U_s, compressing the test gas, until it is reflected at the downstream end of the ST, bursting the secondary mylar diaphragm. Under tailored operation, the test gas is considered stagnant after being additionally compressed and heated from the shock reflection to an ultimate reservoir pressure P_R and temperature T_R. This flow is then accelerated through the axisymmetric nozzle to a Mach 5, and hypervelocity flow is established for about 1 ms in the test section. Total enthalpies h_0 of approximately 10 MJ/kg were established for all shots, resulting in freestream-to-wall temperature ratios T_∞/T_w of roughly 5.

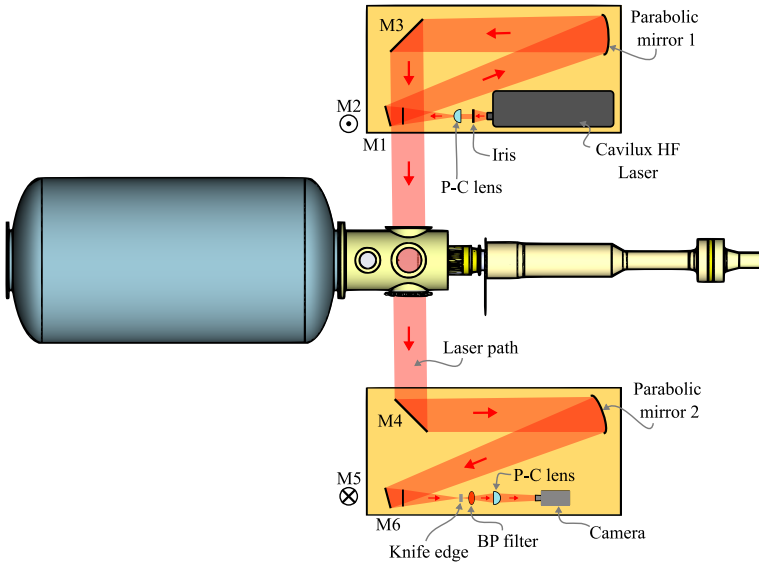

Figure 4.1: Schematic of schlieren setup

Fig. 4.1 depicts a simplified schematic of the schlieren setup. As shown on

the top (port) side, the light from the Cavilux HF laser unit was first sent through an adjustable iris diaphragm and then expanded through a plano-convex (P-C) lens. The beam was collimated by a parabolic mirror and directed by a few planar mirrors (M1-M3) through the test section. On the starboard side, the beam was again directed to the level of the camera with a few planar mirrors (M4-M5) . A parabolic mirror focused the beam back down to a point, where the knife edge was inserted. Finally, the beam passed through a bandpass (BP) filter, which prohibited the chemiluminescene from obscuring the signal, and then a long-focal-length plano-convex lens, which was used to establish the magnification of the images.

The model was a 5°-half-angle cone, 99 cm in total length. The frustum section was aluminum and 83 cm in length, and the interchangeable nosetip was machined out of molybdenum. For the majority of the tests in both campaigns, a 16-cm nosetip with nose radius $R_N = 2$ mm was used. In Campaign B, a blunter $R_N = 3$ mm nosetip, 15 cm in length, was also tested. The model was installed at zero incidence for all the shots, and the angle of attack was checked with a laser level mounted on the upstream side of the nozzle.

4.2 Results: Campaign A

For Campaign A, the optical setup provided a pixel/mm scale of 8.7. Imaging was performed with a Phantom v2640 camera at a frame rate of 160 kHz, using a camera exposure time of 0.5 μs and a laser pulse with of 30 ns. The field of view was between $x = 57$ and 73 cm along the cone surface, or $0.57 \leq x/L \leq 0.73$. Table 4.1

lists the relevant reservoir and freestream conditions for the tests analyzed from this campaign: Shots 2958, 2959 and 2963. The total enthalpy and reservoir conditions were calculated using Cantera and the Shock & Detonation Toolbox [116, 117], and the freestream conditions were generated using University of Minnesota's Nozzle Code, documented in Refs. [118, 119, 120, 121].

As discussed in the following subsections, Shots 2958 and 2959 exhibit very similar boundary-layer behavior: laminar with strong second-mode content. Shot 2963, with the highest unit Reynolds number $Re_\infty = 6.10 \times 10^6$ m^{-1}, demonstrates the beginning of transition to turbulence. The propagation speeds u_p represent the average speed of wavepackets in each run. An average boundary-layer height of $\delta = 1.2$ mm was calculated from the images for all three shots.

Shot	Reservoir			Freestream						
	P_0 (MPa)	h_0 (MJ/kg)	T_0 (K)	U_∞ (m/s)	P_∞ (kPa)	T_∞ (K)	Re_∞ ($\times 10^6$ m^{-1})	u_p (m/s)	M_∞ –	T_∞/T_w –
2958	58.3	10.22	6289	4045	35.9	1607	5.30	3017	4.99	5.4
2959	57.8	9.76	6099	3973	34.7	1524	5.51	2990	5.04	5.2
2963	60.6	9.30	5915	3902	35.4	1438	6.10	2991	5.10	4.9

Table 4.1: Shot Conditions

4.2.1 Boundary-layer and exterior structures

Fig. 4.2 shows a series of reference-subtracted schlieren images of the boundary layer from Shots 2958, 2959, and 2963. An erroneous gamma correction caused the image signal in Shot 2958 to have less than half the dynamic range of that from the other shots, and the corrected images thus appear more grainy. Also, some optical warping caused the wall to appear non-flat in this shot.

Boundary-layer height, δ, was measured with a Sobel-filter-based technique, discussed in Ref. [84]. As mentioned in Section 4.1, the average value $\delta = 1.2$ mm was found for all three shots. A wavelet transform was employed to identify the presence of second-mode wavepacket in schlieren images, as discussed in Refs. [81, 83, 84, 106]. A method using cross-correlation of identified second-mode regions in sequential images was used to calculate the average propagation speeds u_p listed in Table 4.1.

In Shots 2958 and 2959, second-mode wavepackets are especially visible right at the wall, where alternating dark/light waves appear. The example from Shot 2958 in Fig. 4.2(a) shows various wavepackets entering and leaving the field of view. One wave structure starting at $x = 632$ mm appears to sink into the boundary-layer, nearly diminishing at $x = 660$ mm by $t = 0.169$ ms while another packet starting at $x = 660$ mm grows more prominent as it moves downstream. In Fig. 4.2(b), one packet moves steadily from $x = 641$ mm to $x = 708$ mm, and the band of light/dark spots grows taller in the boundary layer, demonstrating pointed peaks by $t = 0.281$ ms.

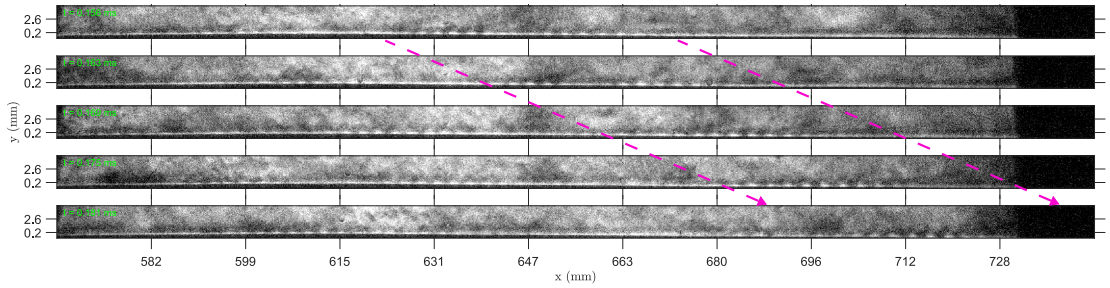

(a) Shot 2958

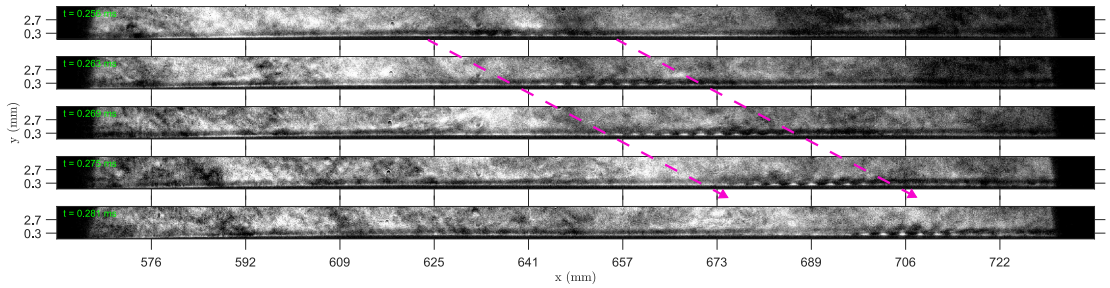

(b) Shot 2959

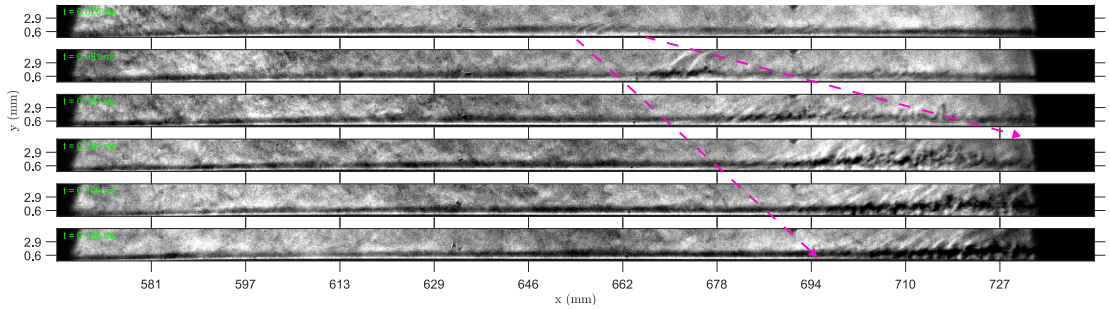

(c) Shot 2963

Figure 4.2: Series of schlieren images from each shot with regions of interest marked

The schlieren sequence in Fig. 4.2(c) exhibits the transitional state of the boundary layer in Shot 2963. A curved structure arcs from the bottom to the top of the boundary layer at $x = 683$ mm in the first image. Moving downstream, this structure grows into two noticeable streaks that pass out of the boundary layer at $t = 0.081$ ms, sending small disturbances downstream. From then on, turbulent breakdown occurs in the region $x \geq 677$ mm, where the boundary layer grows in height and Mach waves radiate into the freestream. As can be seen, this transi-

tional structure expands as it propagates downstream unlike the wavepackets in Figs. 4.2(a) and 4.2(b), which can be easily traced with u_p.

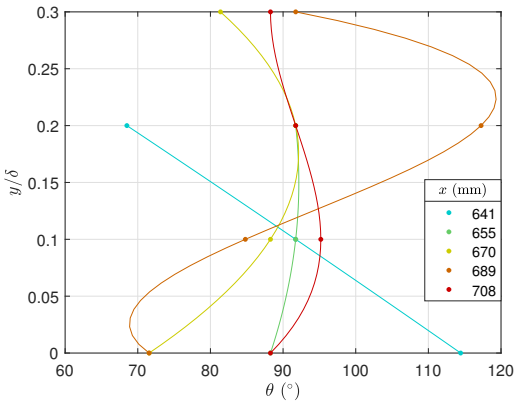

Figure 4.3: Orientation of waves as a function of wall-normal distance

To quantify the trends seen in Fig. 4.2, the angles of structures inside and outside the boundary layer were computed. For second-mode wavepackets clearly confined within boundary layer, rows of harmonic content were cross-correlated with one another. The structure angle θ at each height y/δ was calculated using the peak displacement Δx and the distance between rows Δy such that $\theta = \tan^{-1}(\Delta y/\Delta x)$. Calculation was stopped when rows exhibited low intensity in the bandwith $k = 2 - 3.5\delta$ or when correlated pairs of rows failed to meet a minimum correlation magnitude. The series of n data points from each image was then fitted with a polynomial of order $n - 1$. Fig. 4.3 shows the results for the wavepacket series imaged in Fig. 4.2(b). As can be shown, the wave persists only in the region $y/\delta \leq 0.2$ in the first two images but expands to 30% δ by $x = 670$ mm. The structure angle right at the wall θ_{wall} decreases as the packet moves from $x = 641$ mm to 670 mm, indicating that the waves incline more toward the wall in this region. Then for $x = 689 - 708$ mm, θ_{wall} rises back up, reaching 88° at $t = 0.281$ ms, where

the wavepacket exhibits a largely vertical profile for $y = 0 - 0.3\delta$.

For structures observed just outside δ, a new method was developed to characterize the unique nature of these features which, as shown at $t = 0.087$ ms in Fig. 4.2(c), often appear as a rippling in the boundary layer and nearby freestream. Methods based on Gabor filtering have been implemented to extract features within the field of texture analysis [122]. For this reason, Gabor filtering was utilized to quantify the orientation of structures extending out of the boundary layer in Run 2963. Segments of images with rippled texture were identified, and a bank of Gabor filters oriented $10^\circ \leq \theta \leq 80^\circ$ was used to interrogate overlapping windows within each segment. The magnitude of each filter response was calculated using a sum-of-squares routine, and angles which generated local maxima in the response magnitude were identified as the local structure angle. Resulting structure angles for the five images $t = 0.810 - 0.106$ ms in Fig. 4.2(c) are drawn on the segments in Fig. 4.4.

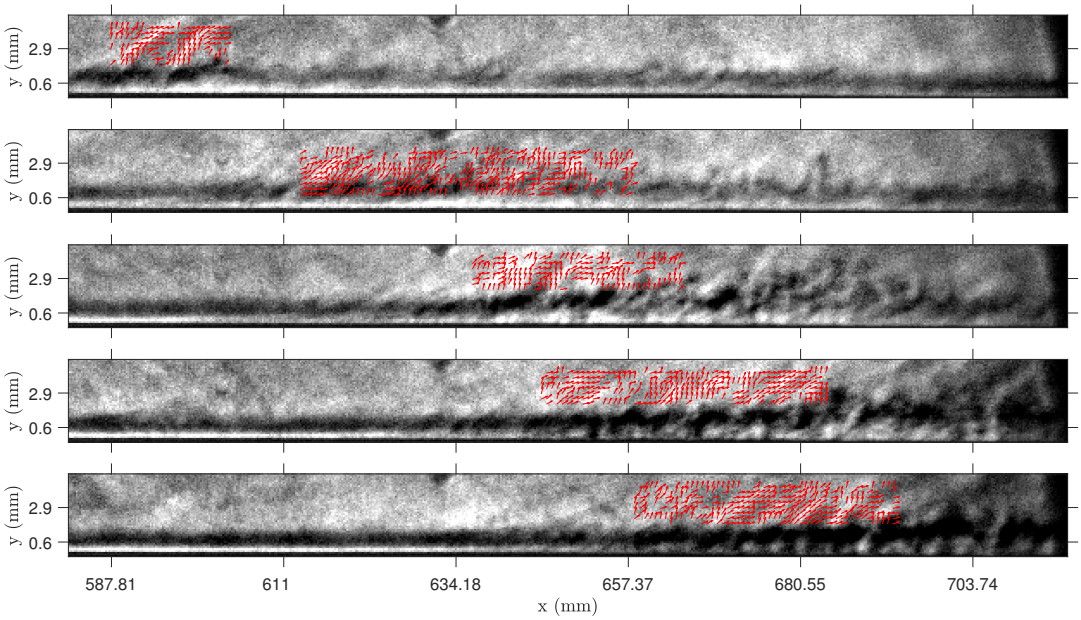

Figure 4.4: Feature angles computed by Gabor filtering

Segments of the vector fields shown in Fig. 4.4 were averaged to provide mean profiles of the exterior feature as it moves downstream. The averaged profiles are displayed in Fig. 4.5, and linear fits, shown as dashed lines, assisted in calculating the Mach angle of the features. The corresponding relative Mach number increases from $M_{rel} = 1.1$ at $x = 674$ mm to $M_{rel} = 2.1$ at $x = 715$ mm, where $M_{rel} = M_e - M_{dist}$. This indicates that, with an expected edge Mach number $M_e = 4.85$, the disturbance Mach number M_{dist} (in a lab-stationary frame) decreases from 3.75 to 2.75.

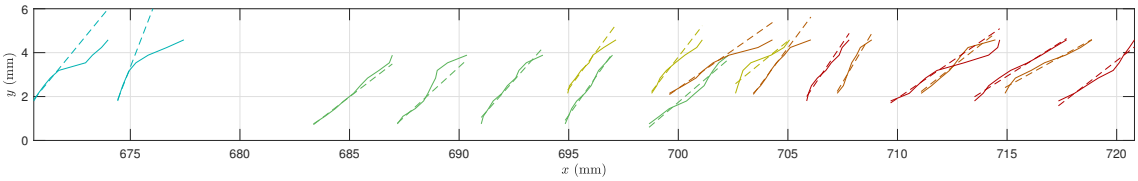

Figure 4.5: Averaged feature angles and associated Mach lines

4.2.2 Spectral content

Apart from their size and orientation, instabilities were also characterized by their spectral content. Wavenumber spectra were calculated for pixel signals at approximately $10\%\delta$ for a central bin $627 < x < 680$ mm within each image. A Blackman window was applied to the bin intensity profile before the power-spectral density (PSD) was computed over the wavenumber domain k. Fig. 4.6 shows the resulting heat map generated by aggregating all image spectra from the duration of each shot. Figs. 4.6(a) and 4.6(b) demonstrate the laminar state of the boundary layer in Shots 2958 and 2959, which both experience only short bursts of second-mode content around $k = 350$ m^{-1}. The heat map in Fig. 4.6(c) exhibits the transitional state of this boundary layer, which experiences broadband turbulent content for $t = 0.15 - 0.27$ ms and $t = 0.88 - 0.95$ ms, in addition to short bursts of second-mode activity centered around $k = 370$ m^{-1}.

These time-resolved maps were instrumental in identifying images with wavepackets and other notable features. For example, the schlieren sequence in Fig. 4.2(a) corresponds to the multi-lobed bright spot at $t = 0.16$ ms in Fig. 4.6(a), and the series shown in Fig. 4.2(b) corresponds to the strong burst at $t = 0.27$ ms in 4.6(b). While strong second-mode wavepackets did not persist in Shot 2963 as much as they did in 2958 and 2959, the unique exterior structures often followed fleeting moments of second-mode content. For example, the streaks identified in Figs. 4.2(c) and 4.4 followed the $k = 280$ m^{-1} burst at $t = 0.62$ ms in Fig. 4.6(c). Similarly, the features analyzed later in this section follow the $k = 370$ m^{-1} burst at $t = 0.59$ ms.

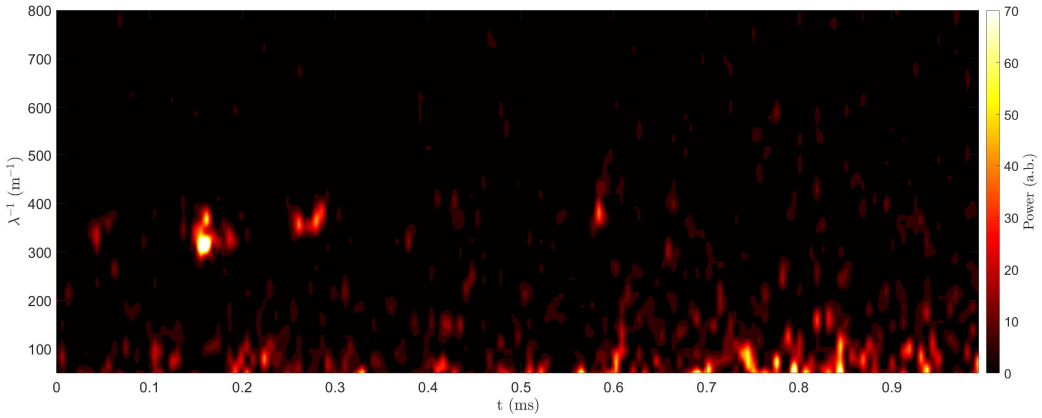

(a) Run 2958 spectra over time

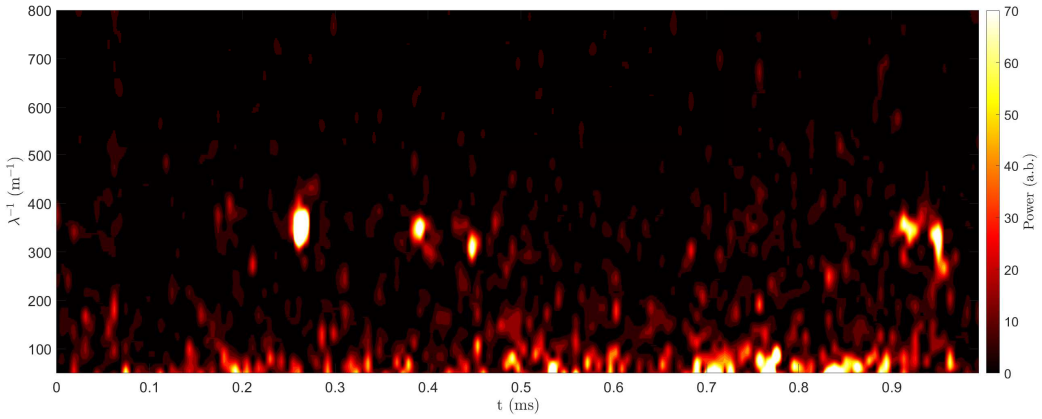

(b) Run 2959 spectra over time

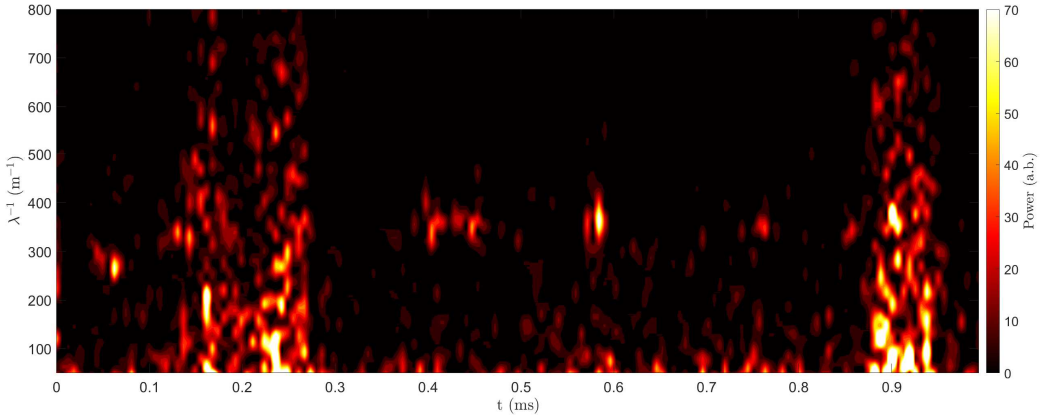

(c) Run 2963 spectra over time

Figure 4.6: Wavenumber spectra throughout run durations

To investigate the evolution of energy within the boundary layer as instabilities move downstream, wavenumber spectra were also computed at various wall-normal

heights. Regions of notable second-mode activity were identified and tracked using the mean propagation speeds u_p presented in Table 4.1. In the schlieren series of Figs. 4.7-4.9, the bounds of these regions are marked, and the resulting spectra are displayed.

Fig. 4.7 provides insight into the multi-lobed second-mode burst at $t = 0.16$ ms in Shot 2958, discussed previously in Figs. 4.2(a) and 4.6(a). It is important to note that, due to the image warping, the y/δ values are not exact for this shot. One strong peak around $k = 365$ m^{-1} corresponds to the content right at the wall within the marked region in the first frame of Fig. 4.7(a). As the wave progresses downstream, it splits into two wave structures visible within the bounds at $t = 0.156 - 0.163$ ms, and the content in Fig. 4.7(b) bifurcates into two peaks, $k = 315$ and 365 m^{-1}. By $t = 0.163$ ms the power of the higher-k peak drops to less than half that of the lower-k peak for 10-20% δ, and from then on, only one wavepacket is observed persisting within the bounds marked on the schlieren, growing taller as it moves downstream. The higher-k peak completely diminishes as the lower-k peak doubles in size at $t = 0.169$ ms. This latter peak persists, distributing more energy higher into the boundary layer. It is to be noted that the z limits on the third, fourth, and fifth plots were increased to 9.5×10^4 to encompass the growth of the low-k peak without obscuring the lower-power split content in the other plots. Ultimately, this analysis shows the apparent splitting of second-mode content leading to the attenuation of high-k content amid growth and spatial redistribution of lower-k content.

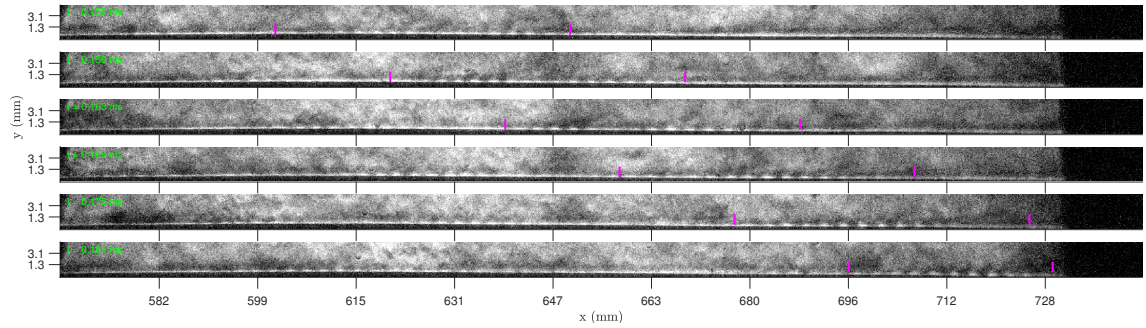

(a) Image series from Run 2958

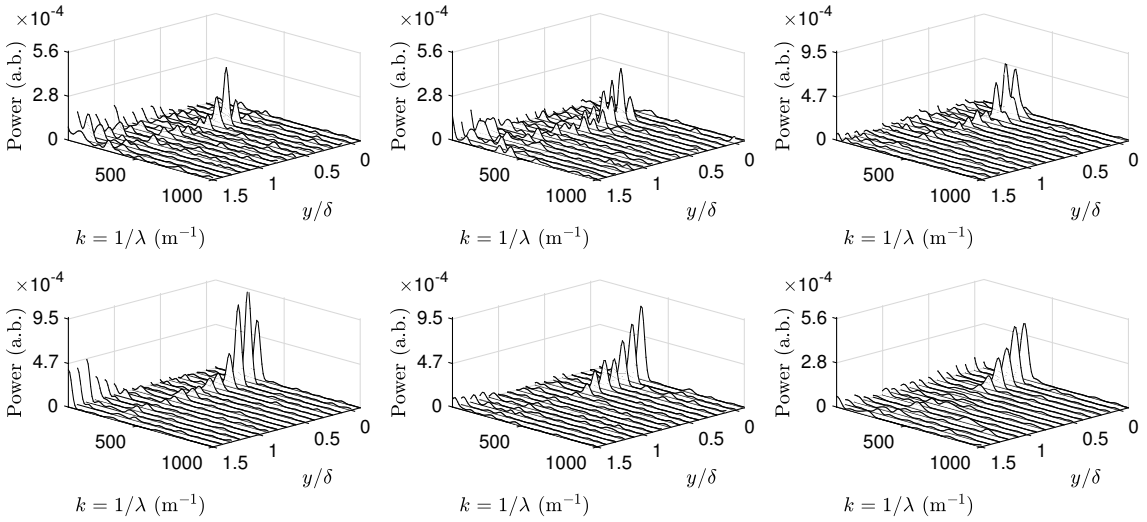

(b) Wall-normal spectral content. Top row (left → right) corresponds to frames $t = 0.150 \rightarrow 0.163$ ms. Bottom row (left → right) corresponds to frames $t = 0.169 \rightarrow 0.181$ ms.

Figure 4.7: Wall-normal wavenumber spectra for Run 2958

Fig. 4.8 expands the analysis of the content at $t = 0.27$ ms in Shot 2959, also discussed previously in Figs. 4.2(b) and 4.6(b). The second-mode content in these images demonstrates a much higher signal-to-noise ratio, producing PSD powers an order of magnitude higher than that in other two shots. The content at the wall in the first image results in a $k = 355$ m^{-1} peak at at 10% δ. This 10%-δ peak remains the maximum throughout the series, nearly quadrupling in power at $t = 0.269$ ms and then decreasing by $t = 0.281$ ms. As the wavepacket propagates, the peak wavenumber shifts gradually from 355 m^{-1} to 335 m^{-1}, and energy is

distributed slightly higher in the boundary layer. For example, at $t = 0.269$ ms the peak power at $y/\delta = 0.3$ sits at 10% of the maximum $y/\delta = 0.1$ peak but rises to 30% of the maximum at $t = 0.281$ ms. Unlike the example from Shot 2958, this series does not exemplify the coexistence of multiple modes of harmonic content; rather, it demonstrates the growth and spatial redistribution of a strong second-mode disturbance.

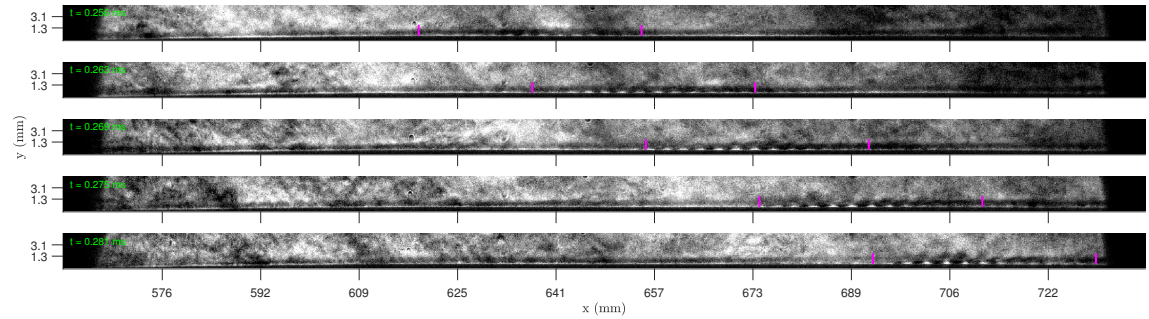

(a) Image series from Run 2959

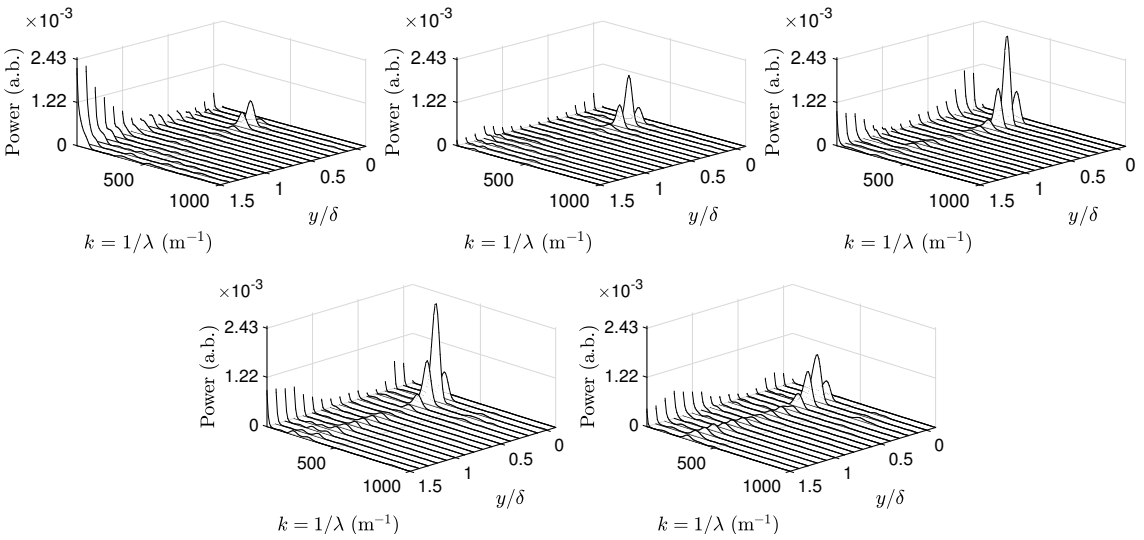

(b) Wall-normal spectral content. Top row (left → right) corresponds to frames $t = 0.256 \rightarrow 0.269$ ms. Bottom row (left → right) corresponds to frames $t = 0.275 \rightarrow 0.281$ ms.

Figure 4.8: Wall-normal wavenumber spectra for Run 2959

Finally, Fig. 4.9 explores the evolution of wavenumber content for the most noticeable second-mode burst from Shot 2963, seen at $t = 0.59$ ms in Fig. 4.6(c).

Similar to the other shots, the series starts with a band of alternating dark/light spots right at the wall which becomes most prominent at $x = 640$ mm at $t = 0.588$ ms. Two small peaks, $k = 305$ and 415 m^{-1}, correspond to the subtle second-mode band in the first image. By $t = 0.588$ ms the peaks have combined and tripled in power, generating a strong 360 m^{-1} peak at 10% δ and a secondary split peak at 20% δ.

The subsequent development distinguishes this transitional shot from the others, exhibiting a mechanism by which energy is transferred out of the boundary layer as the breakdown to turbulence commences. A curved feature extends out of the marked region at $t = 0.594$ ms, decreasing the power of the 10%-δ peak. In the following frame, a periodic structure extends outside the boundary layer at the lefthand side of the marked region, creating a second periodic layer on top of the wavepacket confined within δ. The spectra reflects this observation; high-k content around 440-450 m^{-1} is introduced over $y/\delta = 1 - 1.4$, exceeding the power of the 10%-δ peak which has lowered to 305 m^{-1}. Moving downstream, more structures extend out of the boundary layer, creating the rippling appearance of Mach waves radiating into the freestream, discussed earlier. Even amid this apparent energy transfer out of the boundary layer, the strongest peak of the series at 330 m^{-1} emerges at $t = 0.606$ ms, distributing content up to $y/\delta = 0.4$. Then, high-k content again seems to rise out of the boundary layer; the peak in the lower half of δ shrinks, and content at 390-450 m^{-1} arises over $y/\delta = 1 - 1.4$. The orientation of the structures likely represents the speed at which such content radiates. The disturbance orientation in Fig. 4.5 suggests that radiated content slows down as it

propagates downstream.

The large range of harmonic content, $305 \leq k \leq 450$ m^{-1}, in this example indicates that the boundary layer is on the brink of turbulent breakdown. The apparent back-and-forth transfer of spectral content between the boundary layer and the nearby freestream was associated with other features in this run, such as the exterior structures in Fig. 4.2(c), and is thus considered representative of its spectral behavior. While the example from Shot 2958 demonstrates the attenuation of high-k content, this shot seems to show how such content it is transferred outside δ. It is to be noted that based on two discrete examples, seen in Figs. 4.2(c) and 4.8(a), the boundary layer in Shot 2963 appears to begin breakdown around $x/L = 0.66$; however, transition in the shot was highly intermittent. During the broadband bursts depicted in Fig. 4.6(c), turbulent spots passed through the entirety of the field of view, but at other times, the flow was entirely laminar.

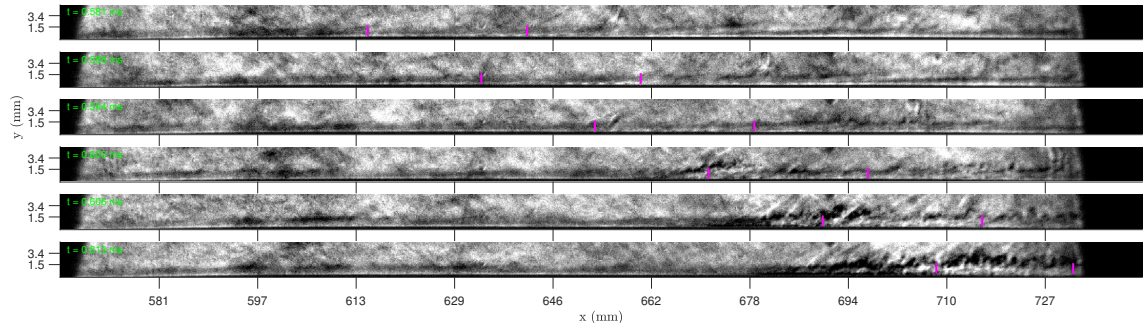

(a) Image series from Run 2963

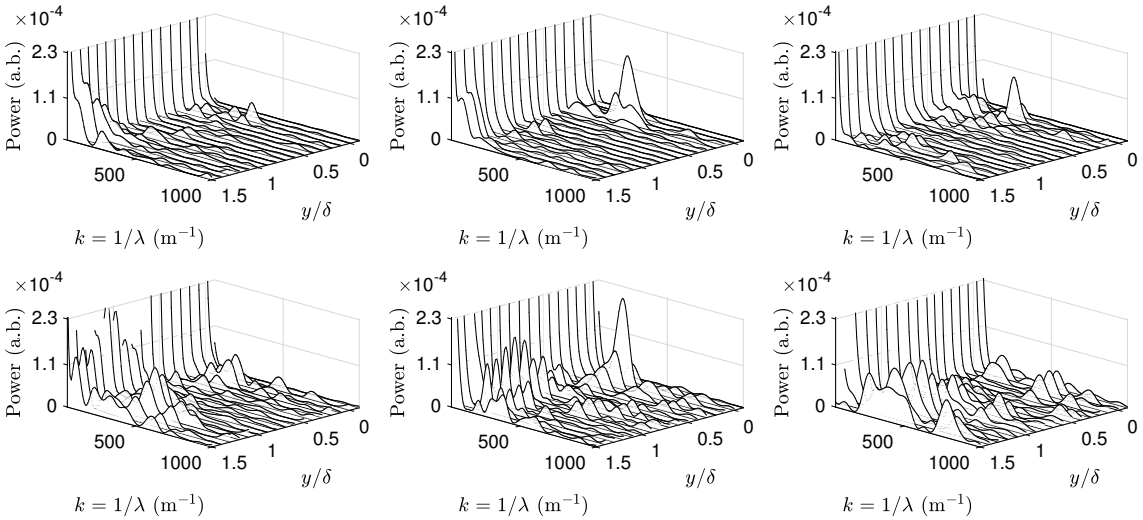

(b) Wall-normal spectral content. Top row (left → right) corresponds to frames $t = 0.581 \rightarrow 0.594$ ms. Bottom row (left → right) corresponds to frames $t = 0.600 \rightarrow 0.613$ ms.

Figure 4.9: Wall-normal wavenumber spectra for Run 2963

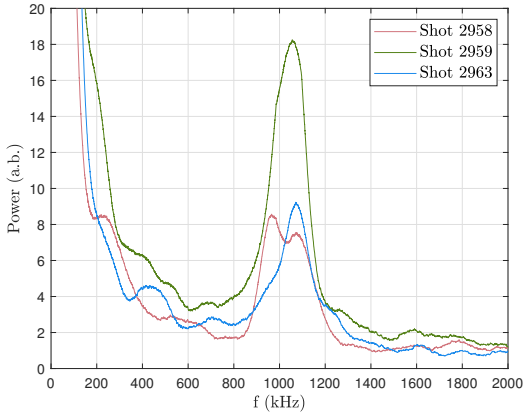

Figure 4.10: Averaged frequency spectra

To visualize some of the spectral content in frequency space in addition to the

wavenumber domain, wavenumber spectra were multiplied by mean propagation speed such that $f = u_p \times k$. Fig. 4.10 compares the PSD of the content at 10% δ in the region $627 < x < 680$ mm from each shot. The spectra were each averaged over a 0.3-ms period where second-mode content was observed but turbulent breakdown was not present. As can be seen, the peak power in Shot 2959 at $f = 1060$ kHz exceeds that of the other two shots by a factor of 2, indicating a much stronger signal-to-noise ratio in this case. The 1060-kHz peak corresponds to a wavenumber $k = 355$ m^{-1}, which could be expected from Fig. 4.6(b). The peak frequency for Shot 2963 at $f = 1070$ kHz corresponds to $k = 360$ m^{-1}, the strong peak seen in the wall-normal spectra of Fig. 4.9(b). Most uniquely, Shot 2958 experiences a split peak with notable energy at 1070 kHz and slightly higher power at 965 kHz. These peaks correspond to wavenumbers $k = 320$ m^{-1} and 355 m^{-1}, similar to those observed in the multi-lobed bright spot at $t = 0.16$ ms in Fig. 4.6(a) and the wall-normal spectra for $t = 0.156$ ms in Fig. 4.7(b). The peaks at 1060 kHz in Shot 2959 and 1070 kHz in Shots 2963 and 2958 all correspond to 86% $u_p/2\delta$, and the 965-kHz peak represents 76% $u_p/2\delta$.

4.3 Results: Campaign B

As mentioned, two new cameras were introduced in Campaign B. Specifically, a Phantom v2512 was used for the first three shots and then swapped out for a Phantom TMX for the remainder of the matrix. Both cameras provided higher frame rates than those available using the Phantom 2640 in Campaign A, and the

optical setup of each run could be modified to focus on features of interest. For example, the frame rate could be set to the maximum 875 kHz to maximize the number of images captured, or it could be lowered slightly to allow for increased laser pulse width and, thus, more light and a better signal-to-noise ratio. In this campaign, the bluntness of the nosetip was also increased in an effort to observe any effects on the modal content within the boundary layer. While a formal analysis of freestream conditions is not yet available for these results, Table 4.2 lists the fill conditions, expected freestream Reynolds numbers, nose radius, and the optical settings used for the shots.

Shot	Fill Conditions P_1 (kPa)	Fill Conditions P_4 (MPa)	Expected Re_∞ ($\times 10^6$ m^{-1})	Nose Radius R_N (mm)	Frame Rate (kHz)	Laser Pulse Width (ns)	Spatial Scale (pixel/mm)
2983	83	105	5.51	2	360	30	6.7
2984	92.6	105	6.10	2	390	30	6.7
2985	100	105	6.17	2	390	30	6.7
2986	100	105	6.17	2	875	20	7.6
2987	100	105	6.17	2	875	20	7.1
2988	100	105	6.17	2	666	30	6.7
2989	83	105	5.51	2	666	30	9.6
2993	120	105	6.36	3	666	30	6.3

Table 4.2: Test Matrix

Examples of reference-subtracted schlieren sequences are shown in Fig. 4.11. Each shows the development of a unique feature. In Fig. 4.11(a), Shot 2983, at an expected $Re_\infty = 5.51 \times 10^6$ m^{-1}, exhibits the propagation of second-mode wavepackets, similar to those seen in Campaign A. While these wavepackets have not been interrogated to the same extent, it is noted that two distinct appearances are visible: the forward-leaning dark streaks moving from $x = 645$ to 670 mm, and

the more conventional rope-like packet propagating from $x = 675$ to 705 mm. In Fig. 4.11(b), Shot 2988 exemplifies the passage of a turbulent spot at an expected $Re_\infty = 6.17 \times 10^6$ m^{-1}. Radiating streaks extending out of the boundary layer are visible, but the signature of second-mode waves appears to lead and follow the structure. This observation could be explained by the visualizations of Casper et al., who found the signature of second-mode waves to persist even after the point of breakdown, encompassing arrowhead-shaped turbulent spots [91]. In Fig. 4.11(c), Shot 2993, with an increased $R_N = 3$ mm, and at an expected $Re_\infty = 6.36 \times 10^6$ m^{-1}, exhibits the presence of a backward-radiating structure. This type of feature has not been seen in any of the other shots; it is possible it could indicate the supersonic instability, or otherwise a non-modal feature related to the increased bluntness.

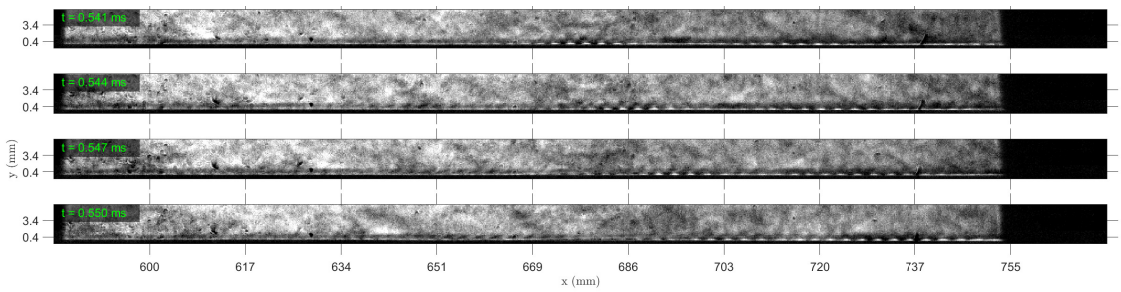

(a) Shot 2983

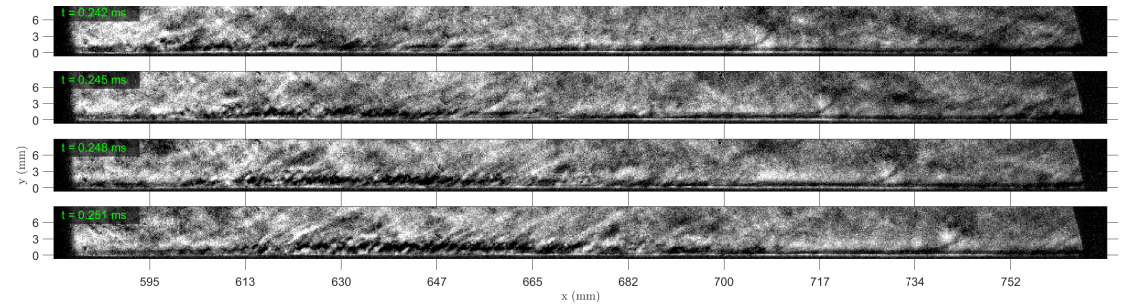

(b) Shot 2988

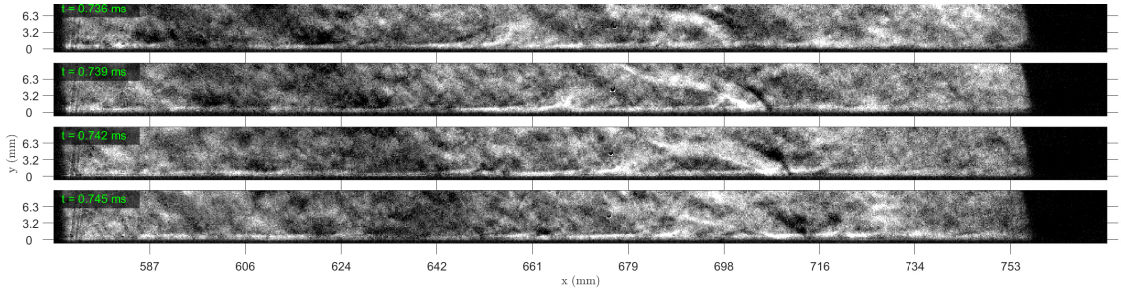

(c) Shot 2993

Figure 4.11: Schlieren series from Shots 2983, 2988, and 2993

The methodology described in Section 3.4.2 was employed to assess frequency content in this campaign. Pixel intensities were reconstructed over time, and power-spectral-density estimates were computed for the time signals. As enumerated in Table 4.2, imaging in Shot 2983 was performed with a frame rate of 360 kHz, and Shot 2987 was imaged at 875 kHz. Unfortunately the frame rate (and its harmonics) from nearly all the shots was found to interfere with the second-mode frequency band identified from the reconstruction. These two shots, however, appeared to retain the

clearest second-mode peaks despite frame-rate corruption, and, for this reason, they are displayed here. Fig. 4.12 compares the resultant spectral content calculated at $x = 680$ mm for Shots 2983 and 2987. It is to be noted that corruption due to frame-rate harmonics can still be observed, for example at $300 \leq f \leq 400$ kHz for Shot 2983 and $800 \leq f \leq 950$ kHz in Shot 2987. Despite being at different Reynolds numbers, both shots exhibit clear spectral content at 1200 kHz, as shown in Fig. 4.12(a). As shown in Fig. 4.12(b), this 1200-kHz peak corresponds to 81% of the normalized frequency $f \times 2\delta/u_p$ for the lower-Re_∞ shot whereas, for the higher-Re_∞ shot, it corresponds 75%.

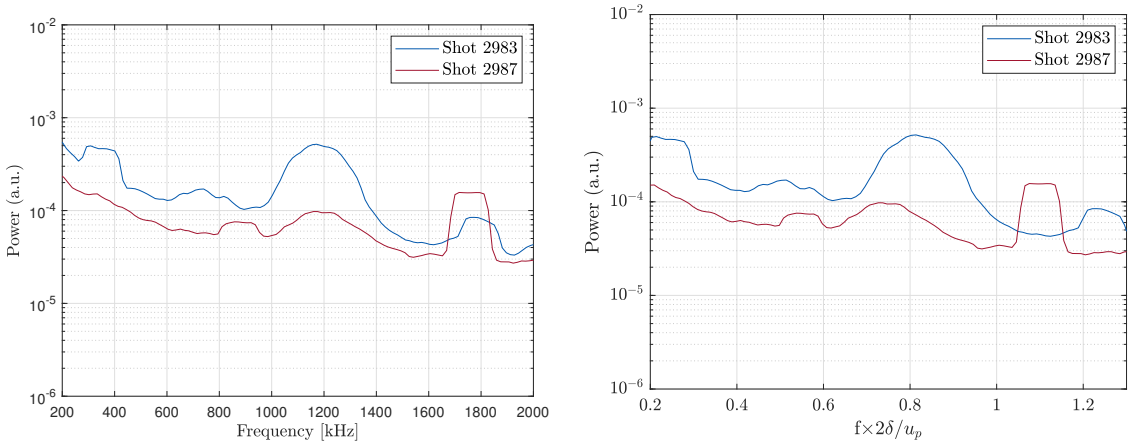

(a) PSD curves

(b) PSD curves normalized by $u_p/2\delta$

Figure 4.12: Spectral content at $x = 680$ mm in Shots 2983 and 2987

4.4 Conclusion

Boundary-layer instability and breakdown was visualized along a slender cone at high-enthalpy conditions. Reservoir pressures of $P_R = 58 - 61$ MPa and specific total enthalpies of $h_0 = 9.3 - 10.22$ MJ/kg were found to produce strong second-mode content as well as intermittent turbulence. In the first campaign, Shots 2958

and 2959, at $Re_\infty = 5.3 - 5.51 \times 10^6$ m^{-1}, exhibit second-mode instabilities with the highest PSD content at 0.1δ; however, the structure angle and wavenumber spatial distribution evolve as these instabilities move downstream. In Shot 2958, distinct wave structures populate the frame $570 \leq x \leq 730$ mm, and a high-wavenumber peak attenuates as a lower-wavenumber peak grows in strength. Waves in Shot 2959 tend to incline more toward the wall in the beginning of their development and then revert to a vertical profile once expanded to 0.3δ. In this shot, an extremely strong second-mode peak persists, shifting from $k = 355$ to 335 m^{-1}. Shot 2963, at the highest $Re_\infty = 6.10 \times 10^6$ m^{-1}, demonstrates intermittent turbulent bursts, indicating the beginning of turbulent breakdown in the range $0.57 \leq x/L \leq 0.73$. Structures extending out of the boundary layer often follow fleeting bursts of second-mode content, starting as individual disturbances and evolving into a series of Mach waves which "ripple" through the boundary layer and nearby freestream. The combination of a Gabor-filtering technique and spectral analysis suggests that these waves provide a mechanism by which high-k content is transferred out of the boundary at disturbance Mach numbers $M_{dist} = 2.75 - 3.75$. Wall-normal spectra depict spectral peaks alternating between lower-k near-wall content and higher-k content over $y/\delta = 1 - 1.4$. In instances where the onset of these structures was observed, breakdown appeared to begin at $x/L = 0.66$. The quantity $0.86\ u_p/2\delta$ was found to predict second-mode frequency peaks in all cases, with Shot 2958 (lowest Re_∞, highest T_∞/T_w) also demonstrating a peak at $f = 0.76u_p/2\delta$. In the second campaign, higher frame rates were utilized to image second-mode wavepackets and the transition to turbulence for expected Reynolds numbers $5.51 \leq Re_\infty \leq 6.36 \times 10^6$

m^{-1}. Second-mode instabilities and turbulent spots were visualized as in the first campaign. For the highest-Re_∞ shot, where the nose bluntness was increased to 3 mm, distinct backward-leaning radiation was also identified. Time reconstruction of pixel intensities from this campaign allowed PSD estimates, indicating a 1200-kHz peak for the range $Re_\infty = 5.51 - 6.17 \times 10^6$ m^{-1}. This peak corresponded to $0.81u_p/2\delta$ in the lower-Re_∞ case and $0.75u_p/2\delta$ in the higher-Re_∞ case.

Chapter 5: Conclusions & Overall Contributions

The effect of the thermal gradient on boundary-layer stability was investigated in two distinct facilities. The following conclusions reiterate the main findings from each set of campaigns, along with the overall impact of the investigation and suggestions to further the knowledge.

The first part of the study took place in HyperTERP, the reflected shock tunnel at the Univeristy of Maryland. Although this tunnel was limited in available reservoir enthalpy, a system consisting of active probe-cooling, LN_2 injection, and thermal management was developed to vary the wall temperature of the model. This study filled an important gap within the available literature on the topic, as it investigated the effect of the wall-to-edge temperature ratio with an unchanging freestream and with close attention to surface thermal uniformity. While a number of previous studies proved unable to characterize either 1) the uniformity of the temperature profile along their models, or 2) the effect of the non-uniformity on resulting boundary-layer stability, the methodology here indicated temperature differences less than 3.3°C in the region 0.34 - 0.88 x_b/L. Three discrete wall-to-edge temperature conditions (T_w = 2.3, 1.9, and 1.6) were established and tested. Simultaneous calibrated schlieren and TSP imaging provided unique insight into the

spatiotemporal development of second-mode-dominated transition.

Filtering and cross-correlation methods were utilized to characterize the structures associated with the second-mode instability at the three thermal conditions. A Sobel filter was used to optically measure boundary-layer height, and it was found that cooling shrunk the boundary layer height as expected from similarity solutions. Cooling also decreased the structure angle at the wall, changing wavepackets from backward-leaning structures in the uncooled case to foward-leaning structures in the cooled case. A time reconstruction of pixel signal intensities was utilized to create power-spectral density estimates of instability content. Overall, spectral analyses agreed well with predictions based on linear stability theory. Cooling generally increased disturbance frequencies, with the exception of two outlier runs from the moderately-cooled set. The most highly-cooled set, $T_w = 1.6$ increased peak second-mode frequencies by approximately 25% relative to the uncooled cases. Finally, cooling increased the growth rate $\Delta N/\Delta Re$, of second-mode instabilities. Spectral saturation was identified only in cooled cases, with the most highly-cooled runs experiencing a 6% reduction in the Reynolds number at saturation relative to the moderately-cooled case.

Heat-flux contours reflected the laminar state of the boundary layer in the uncooled, $T_w = 2.3$, case, with a decreasing temperature profile moving in the downstream direction. The centerline profiles in the moderately-cooled $T_w = 1.9$ case showed some evidence of heat-flux increase along the centerline, suggesting the early transitional state of the boundary layer. At $\alpha = 4^\circ$ angle of attack, the leeward side of the cone surface exhibited high-heating streaks on either side of the centerline

for both cooled and uncooled conditions. Similar to thermal imaging in Ref. [112], it was expected that these streaks represent separation vortices. This conclusion also supported Stetson's separation criterion, $\alpha/\theta_c \geq 0.7$, whereby flow separation would be expected for this geometry [113]. Schlieren images from this angle of incidence demonstrated fully turbulent flow. Topological observations from these contours also suggested an increase in azimuthal flow separation on the leeward side of a pitched cone due to cooling.

Discussion from the variable-wall-temperature study within HyperTERP sought to address each of the three-part transition process: receptivity, stability, and breakdown. While the available data was primarily oriented toward a stability and breakdown-focused analysis, it was hypothesized that the upstream spectral amplitudes provided some insight into the receptivity of the boundary layer under each thermal condition. The results demonstrated that any such reduction in receptivity was outweighed by the destabilized second-mode instability. Similar to Kara et al. [57], it was found that the destabilizing effect of cooling still pushed transition upstream. Additionally, discussion from this study spanned the three types of transition analysis observed in the literature: transition location, spectral growth, and instability structure.

The second part of the study, performed at T5, investigated boundary-layer stability and transition with a freestream enthalpy 10 times higher than that within HyperTERP. Providing the first visualizations of second-mode dominated breakdown to turbulence at high-enthalpy, this study imparted a great deal of insight into this distinct phenomenon. Again the structure of second-mode waves was char-

acterized. For the first campaign, which was limited to a lower frame rate, average boundary-layer heights of 1.2 mm were identified for all cases. Structure angles were observed to evolve in orientation as waves progressed downstream: Waves began at a backward-leaning orientation, then swayed forward as the packet propagated until a certain point. Distinct textured structures extending out the boundary layer were identified for wave undergoing breakdown. A Gabor-filter-based analysis quantified the Mach angles associated with these radiating structures, associating them with a Mach number decreasing from 3.75 to 2.75.

A wall-normal spectral analysis showed strong peaks right above the wall, at wavenumbers near 350 m^{-1}, for the laminar case. In the transitional case, the strong spectral peak at 0.1δ was found to alternate with spectral peaks outside the boundary layer. This suggested that the extending structures seen in schlieren could constitute a mechanism by which high-wavenumber content was passed through the boundary layer during breakdown. Similar to the previous work of Laurence et al. in high-enthalpy flow, it was found that spectral energy was confined very close to the wall [6]. To provide frequency estimates for the lower-frame-rate runs, wavenumbers were scaled by $u_p/2\delta$, and peaks were identified at 1070 kHz in all cases, with an additional peak at 970 kHz in the lowest-Re_∞ case.

In the second campaign, where higher frame rates were available, second-mode wavepackets and the breakdown to turbulence was again visualized. When the nose radius was increased from 2 to 3 mm, unique backward-leaning radiation was observed. The higher frame rates provided more insight into the time-resolved development of these features and allowed pixel signals to be reconstructed over

time. Spectral peaks at 1200 kHz were identified at two different Reynolds numbers, corresponding to 0.81 $u_p/2\delta$ in the lower-Re_∞ case and 0.75 $u_p/2\delta$ in the higher-Re_∞ case analyzed.

This multi-part investigation made a number of contributions to the state of the art in high-speed experimentation as well as the knowledge base within hypersonic aerothermodynamics. Below are listed some of the main accomplishments, both technological and intellectual, as well as some of the work's broader impacts.

Technological Merit

- Constructed an active cooling system capable of decreasing model temperatures by approximately 100°C by integrating probe cooling, LN_2 injection, and insulation within UMD shock tunnel
- Conducted some of the first simultaneous imaging (schlieren and TSP) analyzing the spectral content and thermal footprint of second-mode instabilities
- Performed schlieren imaging in high-enthalpy facility with chemiluminescence, capturing second-mode-instability growth, breakdown, and transition
- Demonstrated efficacy of optical analysis by comparing results to simulations and other measurements (FLDI)

Intellectual Merit

- Evaluated the effect of various levels of wall-cooling on boundary-layer structures, wavenumber and frequency content, spectral amplitude, spectral growth rate, and separated-flow topology

- Visually depicted the transition process in high-enthalpy flow, connecting spectral measurements to flow structures
- Provided an extensive experimental analysis of a boundary layer where the supersonic mode was predicted to be unstable

Broader Impact

- Provided insight into the problem of the thermal boundary layer, reconciling experimental testing with true-flight physics
- Connected numerical predictions to time-resolved, high-resolution images in two distinct facilities

Altogether, this thesis study shed light on a number of phenomena related to the wall-temperature effect on boundary layer stability. Discrepancies between ground and flight tests due to thermal conditions, such as those discussed in Refs. [22, 68], have persisted for decades, whether involving conventional or high-enthalpy tunnels. This study is the first of its kind to straddle two experimental approaches to analyzing the temperature ratio effect on boundary-layer stability: decreasing wall temperature and increasing freestream temperature. It contributed a number of technological achievements: constructing a cooling system to vary wall temperature while minimizing the axial temperature gradient on the model, performing simultaneous planar schlieren and top-down TSP imaging, and introducing the utility of the Gabor filter for textural analysis of high-enthalpy breakdown to turbulence. Future work will involve combining the two methodologies by establishing a wall-cooling system in the high-enthalpy environment. In this way, the temperature

ratio, inherently low to begin with, will be varied amid the unchanging freestream. Acknowledging the dynamic trajectory of hypersonic aircraft, this investigation will elucidate the some of the mechanics experienced by a vehicle ascending and descending through the atmosphere while heating up over time. In conclusion, this study visually has uncovered important stability phenomena that have been plaguing hypervelocity aircraft for decades but have never before been visualized experimentally. Ultimately, this work constitutes one step in connecting the often-elusive experimental data from wind tunnels to true hypervelocity flight in the atmosphere.

Bibliography

[1] Leslie M Mack. Boundary-layer linear stability theory. Technical report, California Inst of Tech Pasadena Jet Propulsion Lab, 1984.

[2] NP Bitter and JE Shepherd. Stability of highly cooled hypervelocity boundary layers. *Journal of Fluid Mechanics*, 778:586–620, 2015.

[3] J Leith Potter. Review of the influence of cooled walls on boundary-layer transition. *AIAA Journal*, 18(8):1010–1012, 1980.

[4] Kenneth Stetson, Elton Thompson, Joseph Donaldson, and Leo Siler. Laminar boundary layer stability experiments on a cone at Mach 8. V-tests with a cooled model. In *20th Fluid Dynamics, Plasma Dynamics and Lasers Conference*, 1989.

[5] Eric C Marineau, Guillaume Grossir, Alexander Wagner, Madlen Leinemann, Rolf Radespiel, Hideyuki Tanno, Brandon C Chynoweth, Steven P Schneider, Ross M Wagnild, and Katya M Casper. Analysis of second-mode amplitudes on sharp cones in hypersonic wind tunnels. *Journal of Spacecraft and Rockets*, 56(2):307–318, 2019.

[6] SJ Laurence, A Wagner, and K Hannemann. Experimental study of second-mode instability growth and breakdown in a hypersonic boundary layer using high-speed schlieren visualization. *Journal of Fluid Mechanics*, 797(3):471–503, 2016.

[7] Hans Wolfgang Liepmann and Anatol Roshko. *Elements of gasdynamics*. Courier Corporation, 2001.

[8] Michael J Hargather and Gary S Settles. A comparison of three quantitative schlieren techniques. *Optics and Lasers in Engineering*, 50(1):8–17, 2012.

[9] Thomas J Whalen, Stuart J Laurence, Eric C Marineau, and Hiroshi Ozawa. A Green's function approach to heat-flux estimation from temperature-sensitive paint measurements. *Measurement Science and Technology*, 32(11):114011, 2021.

[10] Cameron S Butler and Stuart J Laurence. Interaction of second-mode wave packets with an axisymmetric expansion corner. *Experiments in Fluids*, 62(7):1–17, 2021.

[11] Ivett A Leyva. The relentless pursuit of hypersonic flight. *Physics Today*, 70(11):30–36, 2017.

[12] United States. Defense Science Board. Task Force on the National Aerospace Plane. *Report of the Defense Science Board Task Force on the National Aerospace Plane (NASP).* Office of the Under Secretary of Defense for Acquisition, 1988.

[13] Anne Haack, Michael Gerding, and F-J Lübken. Characteristics of stratospheric turbulent layers measured by LITOS and their relation to the Richardson number. *Journal of Geophysical Research: Atmospheres*, 119(18):10–605, 2014.

[14] Robert Sharman and Todd Lane. Aviation turbulence. *Springer International Publishing, Switzerland, DOI*, 10:978–3, 2016.

[15] Fei Li, Meelan Choudhari, Chau-Lyan Chang, Roger Kimmel, David Adamczak, and Mark Smith. Transition analysis for the ascent phase of HIFiRE-1 flight experiment. *Journal of Spacecraft and Rockets*, 52(5):1283–1293, 2015.

[16] Roger L Kimmel, David Adamczak, Allan Paull, Ross Paull, Jeremy Shannon, Robert Pietsch, Myles Frost, and Hans Alesi. HIFiRE-1 ascent-phase boundary-layer transition. *Journal of Spacecraft and Rockets*, 52(1):217–230, 2015.

[17] Roger Kimmel, David Adamczak, Thomas Juliano, and Allan Paull. HIFiRE-5 flight test preliminary results. In *51st AIAA Aerospace Sciences Meeting including the New Horizons Forum and Aerospace Exposition*, page 377, 2013.

[18] MM Sherman and T Nakamura. Flight test measurements of boundary-layer transition on a nonablating 22 deg cone. *Journal of Spacecraft and Rockets*, 7(2):137–142, 1970.

[19] Matthew MacLean, Timothy Wadhams, Michael Holden, and Heath Johnson. Ground test studies of the HIFiRE-1 transition experiment part 2: Computational analysis. *Journal of Spacecraft and Rockets*, 45(6):1149–1164, 2008.

[20] Katya Marie Casper, Steven J Beresh, John F Henfling, Russell Wayne Spillers, and Brian Owen Matthew Pruett. High-speed schlieren imaging of disturbances in a transitional hypersonic boundary layer. Technical report, Sandia National Laboratories (SNL), 2012.

[21] Mujeeb R Malik. Hypersonic flight transition data analysis using parabolized stability equations with chemistry effects. *Journal of Spacecraft and Rockets*, 40(3):332–344, 2003.

[22] Scott A Stanfield, Roger L Kimmel, David Adamczak, and Thomas J Juliano. Boundary-layer transition experiment during reentry of HIFiRE-1. *Journal of Spacecraft and Rockets*, 52(3):637–649, 2015.

[23] Derek Jackson and Brian Launder. Osborne Reynolds and the publication of his papers on turbulent flow. *Annu. Rev. Fluid Mech.*, 39:19–35, 2007.

[24] Nikolaus Rott. Note on the history of the Reynolds number. *Annual review of fluid mechanics*, 22(1):1–12, 1990.

[25] Bruno Eckhardt. Introduction. turbulence transition in pipe flow: 125th anniversary of the publication of Reynolds' paper, 2009.

[26] Nikolaus Rott. Lord Rayleigh and hydrodynamic similarity. *Physics of Fluids A: Fluid Dynamics*, 4(12):2595–2600, 1992.

[27] Michael Eckert. Turbulence research in the 1920s and 1930s between mathematics, physics, and engineering. *Science in context*, 31(3):381–404, 2018.

[28] Herrmann Schlichting and Klaus Gersten. *Boundary-layer theory*. Springer Science & Business Media, 2003.

[29] Osborne Reynolds. III. An experimental investigation of the circumstances which determine whether the motion of water shall be direct or sinuous, and of the law of resistance in parallel channels. *Proceedings of the royal society of London*, 35(224-226):84–99, 1883.

[30] Osborne Reynolds. Iv. on the dynamical theory of incompressible viscous fluids and the determination of the criterion. *Philosophical Transactions of the Royal Society of London*, 186(186):123–164, 1895.

[31] A Sommerfeld. Ein beitrag zur hydrodynamischen erklarung der turbulenten flussigkeisbewegung. *Atti Congr. Int. Math. 4th*, 1908.

[32] Ludwig Prandtl. Flüssigkeitsbewegung. *Handwörterbuch der Naturwissenschaften*, 4:101–140, 1913.

[33] Theodore von Kármán. *Aerodynamics, Selected Topics in the Light of Their Historical Development. Theodore Von Kármán...* NY, Cornell University Press, 1954.

[34] Lord Rayleigh. VIII. On the question of the stability of the flow of fluids. *The London, Edinburgh, and Dublin philosophical magazine and journal of science*, 34(206):59–70, 1892.

[35] Ludwig Prandtl. Über flussigkeitsbewegung bei sehr kleiner reibung. *Verhandl. III, Internat. Math.-Kong., Heidelberg, Teubner, Leipzig, 1904*, pages 484–491, 1904.

[36] Ludwig Prandtl. Der luftwiederstad von kugeln. *Nachrichten von der Gesellschaft der Wissenschaften zu Göttingen, Mathematisch-Physikalische Klasse*, 1914:177–190, 1914.

[37] Geoffrey Ingram Taylor. I. Eddy motion in the atmosphere. *Philosophical Transactions of the Royal Society of London. Series A, Containing Papers of a Mathematical or Physical Character*, 215(523-537):1–26, 1915.

[38] Ludwig Prandtl. Bemerkungen über die entstehung der turbulenz. *ZAMM-Journal of Applied Mathematics and Mechanics/Zeitschrift für Angewandte Mathematik und Mechanik*, 1(6):431–436, 1921.

[39] W Tollmien. Uber die entstehung der turbulenznachr. ges. wiss-gottingen, math. *Phys. Klasse, 1929, pp21*, 44, 1929.

[40] Hermann Schlichting. Zur enstehung der turbulenz bei der plattenströmung. *Nachrichten von der Gesellschaft der Wissenschaften zu Göttingen, Mathematisch-Physikalische Klasse*, 1933:181–208, 1933.

[41] JL Van Ingen. A suggested semi-empirical method for the calculation of the boundary layer transition region. *Technische Hogeschool Delft, Vliegtuigbouwkunde, Rapport VTH-74*, 1956.

[42] L Mack. Computation of the stability of the laminar boundary layer. *Methods in Computational Physics*, 4:247–299, 1965.

[43] Leslie M Mack. Boundary-layer stability theory, document 900-277, rev. a. *Jet Propulsion Lab., Pasadena, CA*, 1969.

[44] Leslie M Mack. Linear stability theory and the problem of supersonic boundary-layer transition. *AIAA Journal*, 13(3):278–289, 1975.

[45] Alexander V Fedorov and Andrew P Khokhlov. Prehistory of instability in a hypersonic boundary layer. *Theoretical and Computational Fluid Dynamics*, 14(6):359–375, 2001.

[46] Thomas L Lewis and Richard D Banner. Boundary layer transition detection on the X-15 vertical fin using surface-pressure-fluctuation measurements. Technical report, NASA, 1971.

[47] Eli Reshotko. Boundary-layer stability and transition. *Annual review of fluid mechanics*, 8(1):311–349, 1976.

[48] Mujeeb R Malik. Prediction and control of transition in supersonic and hypersonic boundary layers. *AIAA Journal*, 27(11):1487–1493, 1989.

[49] Alexander Fedorov and Anatoli Tumin. High-speed boundary-layer instability: old terminology and a new framework. *AIAA Journal*, 49(8):1647–1657, 2011.

[50] Lester Lees. The stability of the laminar boundary layer in a compressible fluid. Technical report, National Advistory Committee for Aeronautics, 1947.

[51] Leslie M Mack. Review of linear compressible stability theory. In *Stability of time dependent and spatially varying flows*, pages 164–187. Springer, 1987.

[52] Pavel V Chuvakhov and Alexander V Fedorov. Spontaneous radiation of sound by instability of a highly cooled hypersonic boundary layer. *Journal of Fluid Mechanics*, 805:188–206, 2016.

[53] Carleton P Knisely and Xiaolin Zhong. Significant supersonic modes and the wall temperature effect in hypersonic boundary layers. *AIAA Journal*, 57(4):1552–1566, 2019.

[54] Clifton H Mortensen. Toward an understanding of supersonic modes in boundary-layer transition for hypersonic flow over blunt cones. *Journal of Fluid Mechanics*, 846:789–814, 2018.

[55] Sasidharan Unnikrishnan and Datta V Gaitonde. Instability characteristics of cooled hypersonic boundary layers. In *AIAA Scitech 2020 Forum*, page 0588, 2020.

[56] S Unnikrishnan and Datta V Gaitonde. Instabilities and transition in cooled-wall hypersonic boundary layers. *Journal of Fluid Mechanics*, 2020.

[57] Kursat Kara, Ponnampalam Balakumar, and Osama Kandil. Effects of wall cooling on hypersonic boundary layer receptivity over a cone. In *38th Fluid Dynamics Conference and Exhibit*, 2008.

[58] Reza Jahanbakhshi and Tamer A Zaki. Optimal heat flux for delaying transition to turbulence in a high-speed boundary layer. *Journal of Fluid Mechanics*, 916, 2021.

[59] Charles B Rumsey and Dorothy B Lee. Measurements of aerodynamic heat transfer and boundary-layer transition on a 10 degree cone in free flight at supersonic Mach numbers up to 5.9. Technical report, NASA, 1961.

[60] Charles B Rumsey and Dorothy B Lee. *Measurements of Aerodynamic Heat Transfer and Boundary-Layer Transition on a 15˚ Cone in Free Flight at Supersonic Mach Numbers up to 5.2.* NASA, 1961.

[61] Charles F Merlet and Charles B Rumsey. *Supersonic Free-flight Measurements of Heat Transfer and Transition on a 10˚ Cone Having a Low Temperature Ratio.* NASA, 1961.

[62] Mitchel H Bertram and Luther Neal Jr. Recent experiments in hypersonic turbulent boundary layers. Technical report, NASA, 1965.

[63] Aubrey M Cary Jr. Turbulent boundary-layer heat transfer and transition measurements for cold-wall conditions at Mach 6. *AIAA Journal*, 6(5):958–959, 1968.

[64] Norman W Sheetz. Ballistics range boundary-layer transition measurements on cones at hypersonic speeds. In *Viscous Drag Reduction*, pages 53–83. Springer, 1969.

[65] Ernest V Zoby and Charles B Rumsey. Analysis of free-flight laminar, transitional, and turbulent heat-transfer results at free-stream Mach numbers near 20 (Reentry F). Technical report, NASA, 1971.

[66] R Wright and E Zoby. Flight boundary layer transition measurements on a slender cone at Mach 20. In *10th Fluid and Plasmadynamics Conference*, page 719, 1977.

[67] PD Germain and HG Hornung. Transition on a slender cone in hypervelocity flow. *Experiments in Fluids*, 22(3):183–190, 1997.

[68] Philippe H Adam and Hans G Hornung. Enthalpy effects on hypervelocity boundary-layer transition: ground test and flight data. *Journal of Spacecraft and Rockets*, 34(5):614–619, 1997.

[69] Richard Scherrer. Boundary-layer transition on a cooled 20 deg. cone at Mach numbers of 1.5 and 2.0. Technical report, NASA, 1950.

[70] Richard Scherrer and Forrest E Gowen. Comparison of theoretical and experimental heat transfer on a cooled 20 degrees cone with a laminar boundary layer at a mach number of 2.02. Technical report, NASA, 1950.

[71] BE Richards and JL Stollery. Further experiments on transition reversal at hypersonic speeds. *AIAA Journal*, 4(12):2224–2226, 1966.

[72] ER Van Driest and J Christopher Boison. Experiments on boundary-layer transition at supersonic speeds. *Journal of the Aeronautical Sciences*, 24(12):885–899, 1957.

[73] Richard J Wisniewski and John R Jack. Recent studies on the effect of cooling on boundary-layer transition at Mach 4. *Journal of the Aerospace Sciences*, 28(3):250–251, 1961.

[74] P Krogmann. An experimental study of boundary layer transition on a slender cone at Mach 5. *In AGARD Laminar-Turbulent Transition 12 p (SEE N78-14316 05-34*, 1977.

[75] Dal V Maddalon. Effect of varying wall temperature and total temperature on transition reynolds number at Mach 6.8. *AIAA Journal*, 7(12):2355–2357, 1969.

[76] Ralph D Watson. Wall cooling effects on hypersonic transitional/turbulent boundary layers at high Reynolds numbers. *AIAA Journal*, 15(10):1455–1461, 1977.

[77] Anthony Demetriades. New experiments on hypersonic boundary layer stability including wall temperature effects. In *Heat Transfer and Fluid Mechanics Institute, Meeting, 26 th, Pullman, Wash*, pages 39–55, 1978.

[78] Christopher R Alba, Heath B Johnson, Matthew D Bartkowicz, Graham V Candler, and Karen T Berger. Boundary-layer stability calculations for the HIFiRE-1 transition experiment. *Journal of Spacecraft and Rockets*, 45(6):1125–1133, 2008.

[79] Heath Johnson, Chris Alba, Graham Candler, Matthew MacLean, Timothy Wadhams, and Michael Holden. Boundary-layer stability analysis of the Hypersonic International Flight Research Transition Experiments. *Journal of Spacecraft and Rockets*, 45(2):228–236, 2008.

[80] Joseph Jewell, Ross Wagnild, Ivett Leyva, Graham Candler, and Joseph Shepherd. Transition within a hypervelocity boundary layer on a 5-degree half-angle cone in air/CO2 mixtures. In *51st AIAA Aerospace Sciences Meeting Including the New Horizons Forum and Aerospace Exposition*, page 523, 2013.

[81] Katya M Casper, Steven J Beresh, John Henfling, Russell Spillers, and Brian Pruett. Transition statistics measured on a 7-degree hypersonic cone for turbulent spot modeling. In *52nd Aerospace Sciences Meeting*, 2014.

[82] Richard E Kennedy, Stuart J Laurence, Michael S Smith, and Eric C Marineau. Hypersonic boundary-layer transition features from high-speed schlieren images. In *55th AIAA Aerospace Sciences Meeting*, 2017.

[83] Laura A Paquin, Shaun Skinner, and Stuart J Laurence. Methodology for investigating the effects of wall cooling on hypersonic boundary layer transition. In *AIAA AVIATION 2020 FORUM*, 2020.

[84] Laura A Paquin, Shaun Skinner, and Stuart Laurence. Effect of wall cooling on the stability of a hypersonic boundary layer over a slender cone. In *AIAA AVIATION 2021 FORUM*, 2021.

[85] Laura A Paquin, Shaun Skinner, and Stuart J Laurence. Boundary-layer disturbances and surface heat-flux profiles on a cooled slender cone. In *AIAA SCITECH 2022 Forum*, 2022.

[86] Alan E Blanchard and Gregory V Selby. An experimental investigation of wall-cooling effects on hypersonic boundary-layer stability in a quiet wind tunnel. Technical report, NASA, 1996.

[87] Sebastien Wylie, Matthew McGilvray, Sreekanth Raghunath, and D Mee. Hypersonic boundary layer instability measurements at Mach 7 and flight total enthalpy. In *International Conference on Flight vehicles, Aerothermodynamics and Re-entry Missions and Engineering (FAR)*, pages 1–8, 2019.

[88] Ryan Oddo, Jonathan L Hill, Mark F Reeder, Daniel Chin, Joshua Embrador, Jeffrey Komives, Matthew Tufts, Matthew Borg, and Joseph S Jewell. Effect of surface cooling on second-mode dominated hypersonic boundary layer transition. *Experiments in Fluids*, 62(7):1–18, 2021.

[89] Gary S Settles. *Schlieren and shadowgraph techniques: visualizing phenomena in transparent media*. Springer Science & Business Media, 2001.

[90] Jayahar Sivasubramanian and Hermann F Fasel. Numerical investigation of the development of three-dimensional wavepackets in a sharp cone boundary layer at Mach 6. *Journal of Fluid Mechanics*, 756:600–649, 2014.

[91] Katya M Casper, Steven J Beresh, and Steven P Schneider. Pressure fluctuations beneath instability wavepackets and turbulent spots in a hypersonic boundary layer. *Journal of Fluid Mechanics*, 756:1058–1091, 2014.

[92] JP Hubner, BF Carroll, KS Schanze, HF Ji, and MS Holden. Temperature- and pressure-sensitive paint measurements in short-duration hypersonic flow. *AIAA Journal*, 39(4):654–659, 2001.

[93] Hiroshi Ozawa, Stuart Jon Laurence, J Martinez Schramm, Alexander Wagner, and Klaus Hannemann. Fast-response temperature-sensitive-paint measurements on a hypersonic transition cone. *Experiments in Fluids*, 56(1):1–13, 2015.

[94] Di Peng, Xu Liu, Lingrui Jiao, Ziyan Li, Xin Wen, Chaokai Yuan, Guilai Han, Yunfeng Liu, Yingzheng Liu, and Zonglin Jiang. Noise reduction for temperature-sensitive paint measurement contaminated by strong background radiation in a high enthalpy hypersonic tunnel. *Acta Mechanica Sinica*, 37(1):20–26, 2021.

[95] Carson L Running, Hirotaka Sakaue, and Thomas J Juliano. Hypersonic boundary-layer separation detection with pressure-sensitive paint for a cone at high angle of attack. *Experiments in Fluids*, 60(1):1–13, 2019.

[96] Anshuman Pandey, Katya M Casper, John T Flood, Rajkumar Bhakta, Russell Spillers, and Steven J Beresh. Tracking turbulent spots on a hypersonic cone at angle of attack using temperature-sensitive paint. In *AIAA AVIATION 2021 FORUM*, page 2889, 2021.

[97] Andrew Mills. Optical oxygen sensors. *Platinum Metals Review*, 41(3):115–127, 1997.

[98] H Ozawa and SJ Laurence. Experimental investigation of the shock-induced flow over a wall-mounted cylinder. *Journal of Fluid Mechanics*, 849:1009–1042, 2018.

[99] Bryan Campbell, Tianshu Liu, and John Sullivan. Temperature sensitive fluorescent paint systems. In *25th Plasmadynamics and Lasers Conference*, page 2483, 1994.

[100] Cameron Butler and Stuart J Laurence. HyperTERP: A newly commissioned hypersonic shock tunnel at the University of Maryland. In *AIAA Aviation 2019 Forum*, 2019.

[101] Richard Edward Kennedy. *An Experimental Investigation of Hypersonic Boundary-Layer Transition on Sharp and Blunt Slender Cones*. PhD thesis, University of Maryland, 2019.

[102] Richard E Kennedy, Stuart J Laurence, Michael S Smith, and Eric C Marineau. Investigation of the second-mode instability at Mach 14 using calibrated schlieren. *Journal of Fluid Mechanics*, 845, 2018.

[103] Inna Kurits, Joseph Norris, and Pratik Bhandari. Temperature-sensitive paint calibration methodology developed at AEDC Tunnel 9. In *49th AIAA Aerospace Sciences Meeting including the New Horizons Forum and Aerospace Exposition*, page 851, 2011.

[104] V Romano, AD Zweig, M Frenz, and HP Weber. Time-resolved thermal microscopy with fluorescent films. *Applied Physics B*, 49(6):527–533, 1989.

[105] LN Cattafesta III, T Liu, and JP Sullivan. Uncertainty estimates for temperature-sensitive paint measurements with charge-coupled device cameras. *AIAA Journal*, 36(11):2102–2108, 1998.

[106] Nathan Shumway and Stuart J Laurence. Methods for identifying key features in schlieren images from hypersonic boundary-layer instability experiments. In *53rd AIAA Aerospace Sciences Meeting*, 2015.

[107] Wallace D Hayes and Ronald F Probstein. Viscous hypersonic similitude. *Journal of the Aerospace Sciences*, 26(12):815–824, 1959.

[108] Massimo Trella and Paul A Libby. Similar solutions for the hypersonic laminar boundary layer near a plane of symmetry. *AIAA Journal*, 3(1):75–83, 1965.

[109] W Mangler. Zusammenhang zwischen ebenen und rotationssymmetrischen grenzschichten in kompressiblen flüssigkeiten. *ZAMM-Journal of Applied Mathematics and Mechanics/Zeitschrift für Angewandte Mathematik und Mechanik*, 28(4):97–103, 1948.

[110] Graeme Gillespie, Andrew Ceruzzi, and Stuart Laurence. Multi-point focused laser differential interferometry for noise measurements in high-speed tunnels. In *AIAA Aviation 2021 Forum*, 2021.

[111] Joel Gronvall, Heath Johnson, and Graham Candler. Hypersonic three-dimensional boundary layer transition on a cone at angle of attack. In *42nd AIAA Fluid Dynamics Conference and Exhibit*, 2011.

[112] Erick Swanson and Steven Schneider. Boundary-layer transition on cones at angle of attack in a Mach-6 quiet tunnel. In *48th AIAA Aerospace Sciences Meeting Including the New Horizons Forum and Aerospace Exposition*, page 1062, 2010.

[113] Kenneth F Stetson. Boundary-layer separation on slender cones at angle of attack. *AIAA Journal*, 10(5):642–648, 1972.

[114] Fei Li, Meelan Choudhari, Chau-Lyan Chang, Jeffery White, Roger Kimmel, David Adamczak, Matthew Borg, Scott Stanfield, and Mark Smith. Stability analysis for HIFiRE experiments. In *42nd AIAA Fluid Dynamics Conference and Exhibit*, page 2961, 2012.

[115] HG Hornung. Performance data of the new free-piston shock tunnel at GALCIT. *AIAA Paper 92-3943*, 1992.

[116] David G Goodwin, Harry K Moffat, and Raymond L Speth. Cantera: An object-oriented software toolkit for chemical kinetics, thermodynamics, and transport processes, 2009.

[117] Shannon Browne, J Ziegler, and JE Shepherd. Numerical solution methods for shock and detonation jump conditions. *GALCIT report FM2006*, 6:90, 2008.

[118] Michael J Wright, Graham V Candler, and Marco Prampolini. Data-parallel lower-upper relaxation method for the Navier-Stokes equations. *AIAA Journal*, 34(7):1371–1377, 1996.

[119] Graham Candler. Hypersonic nozzle analysis using an excluded volume equation of state. In *38th AIAA Thermophysics Conference*, page 5202, 2005.

[120] Heath Bradley Johnson. *Thermochemical interactions in hypersonic boundary layer stability*. University of Minnesota, 2000.

[121] Ross M Wagnild. High enthalpy effects on two boundary layer disturbances in supersonic and hypersonic flow. Technical report, MINNESOTA UNIV MINNEAPOLIS, 2012.

[122] Olaf Pichler, Andreas Teuner, and Bedrich J Hosticka. A comparison of texture feature extraction using adaptive Gabor filtering, pyramidal and tree structured wavelet transforms. *Pattern Recognition*, 29(5):733–742, 1996.